NASA/CR—97-206296

An Experimental Study of the Near Field Region of a Free Jet With Passive Mixing Tabs

D.G. Bohl and J.F. Foss
Michigan State University, East Lansing, Michigan

Prepared under Grant NAG3–1459

National Aeronautics and
Space Administration

Lewis Research Center

November 1997

This report is a formal draft or working paper, intended to solicit comments and ideas from a technical peer group.

This report contains preliminary findings, subject to revision as analysis proceeds.

Available from

NASA Center for Aerospace Information
800 Elkridge Landing Road
Linthicum Heights, MD 21090-2934
Price Code: A08

National Technical Information Service
5287 Port Royal Road
Springfield, VA 22100
Price Code: A08

Technical Report

MSU-ENGR-04-96
TSFL-R-044

Title: AN EXPERIMENTAL STUDY OF THE NEAR FIELD REGION OF A FREE JET WITH PASSIVE MIXING TABS

Prepared by: D.G. Bohl and J.F. Foss
Turbulent Shear Flow Laboratory
Department of Mechanical Engineering
Michigan State University
East Lansing, Michigan

Prepared for: Dr. K. Zaman
NASA Lewis Research Center
Grant No. NAG3-1459

Date: 29 August 1996

Abstract:

An experimental study was performed to determine the flow characteristics of a tabbed free jet. Results were acquired in the near field (nominally 2 tab widths upstream to 2 tab widths downstream of the exit plane) of a tabbed jet. Upstream pressure results showed static pressure distributions in both the x- and y-directions along the top surface of the tunnel. Hot-wire measurements showed rapid expansion of the core fluid into the ambient region. Two counter rotating regions of streamwise vorticity were shown on each side of the primary tab.

An enhancement of the tabbed jet concept was proposed and tested. Specifically, two tabs, half the scale of the primary tab, were added to the primary tab to provide attachment surfaces for the normally occurring ejection of fluid. The secondary tabs caused a slight increase in the streamwise vorticity created from the upstream static pressure gradient while significantly increasing the re-oriented boundary layer vorticity. The combined pumping effect of the two counter rotating regions of vorticity caused a significant increase in the transport of the jet core fluid into the surrounding region.

COLLEGE OF ENGINEERING
MICHIGAN STATE UNIVERSITY
EAST LANSING, MICHIGAN 48824

TABLE OF CONTENTS

LIST OF FIGURES

NOMENCLATURE

English

A:	Coefficient in Collis and Williams relationship. See (3.1).
b:	Base length of the primary tab, 200mm.
B:	Coefficient in Collis and Williams relationship. See (3.1).
l_w:	Length of active region of hot-wire sensor.
n:	Coefficient in Collis and Williams relationship. See (3.1).
N:	Node. See (5.1) and (5.2).
N':	Half node. See (5.2).
p:	Static pressure.
P_{atm}:	Atmospheric pressure.
Q:	Magnitude of the velocity measured by a hot-wire.
R:	Radius of curvature. See (5.3).
S:	Saddle. See (5.1) and (5.2).
S':	Half saddle. See (5.2).
u:	Velocity in the streamwise (x) direction.
U_{up}:	Upstream reference velocity, calculated from the pressure differential in the tunnel contraction upstream of the tunnel exit.
v:	Velocity in the spanwise (y) direction, lateral velocity.
V:	Velocity magnitude.
w:	Velocity in the vertical (z) direction, transverse velocity.

Greek

α:	Angle of secondary tab to the horizontal plane, generic length measure.
β:	Angle between a slant wire and the probe axis, generic velocity measure.
$\chi_{surface}$:	Euler characteristic for a surface. See (5.1) and (5.2).
δ:	Boundary layer thickness.
$\delta_{ambient}$:	Maximum penetration of the shear layer into the ambient region.
δ_{core}:	Maximum penetration of the shear layer into the core region.
δ_d:	Displacement thickness.
$\delta_{high\ speed}$:	Maximum penetration of high speed fluid into the ambient region.
γ:	In-plane flow angle.
η:	Ratio of voltage of a hot-wire at an angle divided by the voltage of the same wire at γ=0. See equation (4.3).
σ:	Angle of the secondary tabs with respect to the x-z plane.

θ:	Shear layer momentum thickness. See (5.4).
ω_x:	Stream wise vorticity. See equation (4.10).

Symbols

-:	Average value; Velocities are time averaged, Stream wise vorticity is spatially and temporally averaged. See equation (4.13).
~:	Root mean square value. See equation (4.14).
*:	Non dimensional value. See section 4.7 for definitions.

Definitions

ambient region:	Area in the flow field outside of the projected tunnel walls.
core region:	Area in the flow field inside of the projected tunnel walls.
modified geometry:	Tab configuration that consists of one primary tab with one secondary tabs on each side of the primary tab.
primary tab:	The single large (200mm) tab that protrudes into the core region. Used in both the simple and modified geometries.
secondary tab:	The smaller (100mm) tab that protrudes into the ambient region. Used in pairs.
primary geometry:	Tab geometry that consists of a single primary tab.
un-tabbed geometry:	Tunnel configuration without any tabs. Reference case.

1. INTRODUCTION

1.1 Previous Work

The restrictions on noise emissions from jet engines have led to the development of strategies to combat noise in jet flows. There are two sources of jet noise that can be targeted by the rapid mixing of the heated jet core with the cooler co-axial fan flow. The first of these two sources is termed "screech". This noise source is related to the interaction of coherent turbulent structures with standing shock-expansion waves, and the resulting feedback loop, in supersonic jets. The second noise type is a "broad band" noise that occurs over a range of low frequencies. This noise is due to the dynamics and interaction of large and small scale turbulent structures (Ahuja and Brown (1989)).

The development of the High Speed Civil Transport has centered on two passive mixing strategies previously investigated. The first of these strategies is the use of lobed nozzles. A study of the effects of lobes in mixing two streams of fluid was conducted by Koch am Brink (1991) and also reported by Koch am Brink and Foss (1993). This study demonstrated that the lobe geometry creates strong streamwise vortical motions which substantially increase the mixing between the two layers. It was shown that the shape of the lobes creates pressure gradients which re-orient the boundary layer vorticity from each lobe into the streamwise direction. The areas of streamwise vorticity were found to have a length scale on the order of the lobe height. The lobed geometry was shown to have superior mixing characteristics over a simple two stream mixing layer.

An alternate strategy, pursued by the NASA Lewis Research Center, among other places, has been to use passive mixing tabs in the exit plane of the jet. An obstruction is

placed in the exit plane of the high speed jet core. The obstructions (i.e. "passive mixing tabs") promote rapid exchange of the core fluid with the surrounding fluid.

Early research into the physics of tabbed flows was reported in Bradbury and Khadem (1975). In that work the authors studied the effect of changing boundary conditions on the entrainment rate of free jets. They found that boundary layer thickness, turbulence levels in the approach boundary layer and nozzle convergence did not have any significant effect on the entrainment rate of the jet flow. Rather they determined that by placing an object perpendicular to the streamwise direction into the core flow they could create large scale distortions in the flow field. It was shown in this work that the core splits into two high speed regions for a round jet with two tabs placed 180 degrees apart in the jet exit plane. A significant increase in the entrainment for the tabbed jet was indicated when compared to the untabbed jet.

Bradbury and Khadem (1975) proposed that two possible reasons for the distortion in the jet flow. They reported that either: 1) trailing vortex motions shed by the tab "stirred" the fluid or 2) the simple deflection of the core flow by the object created the distortions.

Ahuja and Brown (1989) expanded on many of Bradbury and Khadem's (1975) results. They showed that a jet with two opposing tabs had a nondimensional centerline velocity decay that was much faster than that for the untabbed jet. However, they also showed that the rate of decay of the nondimensional centerline velocity was much higher for a tabbed jet with two tabs rather than three or four. Finally the authors showed that the same effect can be seen in both heated and unheated cores and that the two tab configuration showed a significant drop in the average core temperature downstream of the exit.

This work (Ahuja and Brown (1989)) was important in that the authors reported two results that were important to later studies. First, the tab placed into the flow must have a certain length dimension in order to have an effect on the flow field. Second, it was reported that the flow distortion was not restricted to compressible flows. This second result was critical in that the analytical as well as experimental analysis of the flow field could be performed on an incompressible fluid.

In an attempt to infer the physics of a tabbed jet Ahuja and Brown (1989) noted that the high level of mass entrainment in a round jet is caused by the large scale motions shed by the jet. It was shown (by the elimination of the screech tones) that for a tabbed jet these motions were altered. The conjecture was that other large scale motions, created by the tab, were responsible for the rapid mixing in the tabbed jet. Ahuja and Brown concluded by stating that the simplicity (i.e. the lack of moving parts) in the tabbed jet concept made it attractive for use in gas turbine engines.

Much of the current work in the use of tabbed jets has been conducted jointly by NASA Lewis Research Center (Dr. K. Zaman) and the Ohio State University (Dr. M. Reeder and Dr. M. Samimy). A series of studies were performed over several years which resulted in several conference papers and journal publications. Their results are summarized here and provide the basis for the present study.

Zaman et. al. (1994) reported that tabs, which were perpendicular to the streamwise direction and extend into the core flow, produce an area of counter rotating streamwise vorticity, ω_x, on either side of the tab. The sign of this vorticity was of opposite sign from what one would expect from the re-orientation of the boundary layer vorticity around the tab. These regions, shown schematically in Figure 1.1, create the large scale distortion in

the flow field shown in previous works (Ahuja and Brown (1989) , Bradbury and Khadem (1975)). In their discussion, the authors stated that fluid from the core region would be ejected as a result of the streamwise vorticity as shown in Figure 1.1. In addition ambient fluid was entrained into the core region downstream of the tab as a result of the vortical motions shown in Figure 1.1. This large scale exchange of fluid between the core and ambient regions provided the rapid mixing produced by the tabbed jet (Zaman et. al. (1994)).

These studies also confirmed many of the results of Ahuja and Brown(1989). Specifically they showed:

1) the results were similar for both supersonic and subsonic flows. This result was demonstrated through flow visualizations results which clearly showed qualitatively similar results for both flows (Zaman et. al.(1991)).

2) the tab height (i.e. the height of the tab projected into the exit plane of the jet) must be on the order of the approach boundary layer thickness or larger in order to have a significant effect on the flow. A tab which does not exceed this height will not generate structures larger than the boundary layer and will not effect the global flow field (Zaman et. al. (1994)).

3) more than four tabs resulted in a decreased effectiveness of the tabs. Specifically, the lobes of core fluid that were created by the tabs interacted and combined when four or more tabs were used. For example, a jet with six tabs created a similar distortion of the flow field as a tabbed jet with three tabs (Zaman et. al. (1992).

4) a two tab configuration experienced more rapid centerline decay than a three or four tab configuration. It was clearly shown by the authors that for a tabbed round jet with two opposing tabs the core flow split into two high speed regions. With four or more tabs the flow field formed four lobes of high speed fluid connected at the center of the jet (Zaman et. al. (1994)). Note that this observation illustrated that using the centerline average velocity decay to determine the "effectiveness" of a tab is incomplete and could be deceptive.

5) the screech tones in the jet were reduced. Additionally, the broad band noise was also reduce in the tabbed jet flow (Zaman et. al. (1992)).

Other important features of the flow field, in addition to items 1-5 above, were also detailed. A series of results were reported in which the orientation of the tab was changed and the differences in the flow field were observed (Zaman et. al. (1994)). The authors showed that by orienting the tabs so that they pointed upstream it was possible to create an ejection of fluid from the region behind the tab. (Note that this was the opposite of the effect seen when the tab was placed perpendicular to the streamwise direction as described above.) The reason for this difference was believed to be a change in sign of the streamwise vorticity introduced into the flow. When the orientation of the tab was changed so that the tab point downstream in the flow, the distortion of the flow field (i.e. the ejection of core fluid) increased when compared to the perpendicular orientation. In addition the thrust penalty decreased for the same size tab. Thrust loss for the downstream orientation was estimated to be nominally 1.5% per tab. This "penalty" was computed by comparing the actual thrust to the thrust calculated for a uniform flow from the isentropic relationship (Zaman et. al. (1994)).

Steffen et. al. (1996) reported results from a computational study in a 3:1 aspect ratio rectangular jet which mimicked an experimental jet to which the computational results were compared. These results showed that when two tabs were placed at the midpoint of the short sides, the jet experienced a switch in the major axis at x/d=3, where d is the equivalent hydraulic diameter of the rectangular nozzle. For the same jet without tabs, axis switching was not reported at the farthest measurement location x/d=14, although the data did indicate that the flow would experience an "axis switch" at a farther downstream location.

Foss and Zaman (1996) studied the effects of a tab on a two stream mixing layer. In this experimental study the velocity ratio between the free streams was 2:1 with the tab pointing into the high speed stream. Using the "Peak-Valley-Counting" technique (Ho and Zohar (1994)) the authors were able to show that the peak in the dissipation spectra in the tabbed flow shifted to higher wave numbers. This indicated that the turbulent cascade increased in length (i.e. the wave number distance between the largest and smallest scales increased) for the tabbed flow. In addition to having smaller scales when compared to the untabbed shear layer the small scales in the tabbed shear layer contained more energy. It was noted that the location in the flow field with the highest peak in the dissipation spectra did not coincide with the location of the peak in the fluctuating streamwise velocity values.

1.2 Analytical Considerations of the Flow Field

The effect of placing tabs into the exit plane of a jet is to produce large scale streamwise vortical motions into the flow field. The orientation of the tabs is responsible

for determining the sign of the vorticity introduced into the flow. The tab is assumed to be oriented downstream, see Figure 1.2, in the following analysis.

In past studies (Reeder (1994), Zaman (1993)), analysis of the sources of vorticity in the flow has concentrated on the streamwise vorticity created by the tabs. This analysis, while important, serves to analyze only part of the streamwise vorticity seen in the flow field after the jet exit. There is also a significant region of streamwise vorticity present due to the re-orientation of the approach boundary layer vorticity.

The vorticity in a two dimensional laminar boundary layer is aligned with the y-direction using the coordinate system shown in Figure 1.3. Note that all three components of vorticity in a turbulent boundary layer can exist instantaneously; however, the time averaged vorticity in a turbulent boundary layer only involves the y-direction component. This vorticity was introduced into the flow by the creation of a velocity gradient in the z-direction, i.e. $\partial u / \partial z$. To understand possible additional sources of vorticity in a boundary layer consider the x-component linear momentum equation:

$$\frac{\partial u}{\partial t} + u\frac{\partial u}{\partial x} + v\frac{\partial u}{\partial y} + w\frac{\partial u}{\partial z} = g_x - \frac{1}{\rho}\frac{\partial P}{\partial x} + \nu\left(\frac{\partial^2 u}{\partial^2 x} + \frac{\partial^2 u}{\partial^2 y} + \frac{\partial^2 u}{\partial^2 z}\right). \tag{1.1}$$

At a wall u,v,w as well as the derivatives parallel to the wall (i.e. $\partial ()/\partial x$ and $\partial ()/\partial y$) will be equal to zero if there is no blowing/suction applied. If, in addition, the body forces are equal to zero and the time derivatives are neglected, (1.1) simplifies to

$$0 = -\frac{1}{\rho}\frac{\partial P}{\partial x}\Big|_{z=0} + \nu\left(\frac{\partial^2 u}{\partial^2 z}\right)\Big|_{z=0}. \tag{1.2}$$

Vorticity in the y-direction, ω_y, is defined as

$$\omega_y = \frac{\partial u}{\partial z} - \frac{\partial w}{\partial x}. \tag{1.3}$$

Equation (1.3) can be simplified in a two dimensional boundary layer to

$$\omega_y \approx \frac{\partial u}{\partial z}. \tag{1.4}$$

Equation (1.4) is then substituted into (1.2) and evaluated at the physical boundary to yield

$$\nu \frac{\partial \omega_y}{\partial z}\Big|_{z=0} \approx \frac{1}{\rho}\frac{\partial P}{\partial x}\Big|_{z=0}. \tag{1.5}$$

Equation (1.5) can be generalized for a flow parallel to a surface by

$$\frac{\partial \omega_b}{\partial n}\Big|_{n=0} = +\frac{1}{\mu}\frac{\partial P}{\partial s}\Big|_{n=0} \tag{1.6}$$

where n is the direction normal to the surface, s is the direction of the velocity vector parallel and near to the surface, and b is the direction perpendicular to the same velocity vector. (Note that $\hat{s} \times \hat{n} = \hat{b}$.) This general result indicates that a static pressure gradient in the plane of a surface provides a flux of vorticity into the flow with a direction parallel to the plane of the surface.

Equation (1.5) specifically shows that if there is a pressure gradient in the x-direction there will be y-component vorticity, ω_y, added into the flow at z=0. It has been shown in past studies (Reeder (1994), Zaman (1993)) as well as in the present study (section 5.3.1 and 5.5.1) that the presence of a passive mixing tab creates a strong positive pressure gradient ($\{\partial P/\partial x\ \hat{}0\}$; for $y \approx 0$ and $z \approx 0$) upstream of the jet exit. The adverse pressure gradient serves as a source of vorticity into the flow. In the analysis of a

boundary layer it is instructive to note that separation occurs when the vorticity becomes zero at the wall.

The vorticity upstream of the tab is re-oriented and stretched by the velocity gradients in the flow. The x-direction vorticity transport equation is given by (Whitham (1963), equation (17)):

$$\frac{D\vec{\omega}}{Dt} = \vec{\omega}\cdot\nabla\vec{v} + \nu\nabla^2\vec{\omega} \tag{1.7}$$

Equation (1.7) can be decomposed into the x-direction transport equation as

$$\frac{D\omega_x}{Dt} = \omega_x\frac{\partial u}{\partial x} + \omega_y\frac{\partial u}{\partial y} + \omega_z\frac{\partial u}{\partial z} + \nu\left(\frac{\partial^2\omega_x}{\partial^2 x} + \frac{\partial^2\omega_x}{\partial^2 y} + \frac{\partial^2\omega_x}{\partial^2 z}\right) \tag{1.8}$$

The first term of (1.9) on the right hand side is the stretching term, the second and third terms are re-orientation terms, and the fourth term is the viscous diffusion term. It is possible to re-orient the boundary layer vorticity, ω_y, into streamwise vorticity in the presence of a velocity gradient $\partial u/\partial y$ via (1.8). The $-\omega_y$ from the boundary layer will become $+\omega_x$ for $y<0$ for the tabbed jet. Note that for a tabbed jet $\partial u/\partial y < 0$ for $y<0$. The vorticity from the re-oriented boundary layer is of opposite sign to what was found to dominate the tabbed jet flow (Zaman (1993)). It was this observation which led to the further analysis (Reeder (1994), Zaman (1993)) of the sources of the negative sense streamwise vorticity seen in the flow field. (Note, it will be shown in this study that the re-oriented boundary layer vorticity plays a significant role in the large scale transport of fluid from the core region to the ambient region in the near region ($x \leq 2b$) of the flow field.)

It is possible to show, using (1.6), that a pressure gradient in the y-direction will also serve as a source of streamwise vorticity in the flow by

$$\nu \frac{\partial \omega_x}{\partial z}\Big|_{z=0} \approx -\frac{1}{\rho}\frac{\partial P}{\partial y}\Big|_{z=0}. \qquad (1.9)$$

Equation (1.9) is derived from the general expression (1.6) where n is the z-direction, b is the x-direction and s is the y-direction. The tabs, in addition to creating a pressure gradient in the x-direction, also create a pressure gradient in the y-direction (Zaman et. al. (1993), section 5.3.1 and 5.5.1). Since $\partial P/\partial y$ was greater than zero for $y<0$ this pressure gradient will act as a source of negative ω_x in the flow field.

Zaman (1993) first discussed the two regions where pressure gradients were found that would provide a flux of negative sense streamwise vorticity into the flow[1]. These regions (labeled 1 and 2 on Figure 1.2) were found directly upstream of the jet exit along the jet wall and on the face of the tab itself. The upstream pressure distribution, dubbed the "pressure hill", was found to be the dominant source of vorticity for the flow field. This was determined by displacing the tab downstream from the jet exit (creating a gap between the tab and the jet exit) which reduced the pressure distribution upstream of the tab. This was shown to greatly reduce the overall effect of the tabbed jet (Zaman et. al. (1994)).

The observation that the effects of tabs are independent of compressibility (Ahuja and Brown (1989) and Zaman et. al. (1991)) is important in the error analysis sources of

[1]Zaman credits Dr. J. Foss of Michigan State University with proposing the idea of the two possible regions of pressure gradients which provide a flux of streamwise vorticity into the flow.

streamwise vorticity in that there are other sources of vorticity in a compressible flow which have been neglected in the above analysis.

1.3 Present Study

The present study was performed to provide further details about the flow field of the tabbed jet. The experimental apparatus, with exit dimensions of 610 mm x 610 mm and a tab length of 200 mm was of a very large scale when compared to those used in the works of K. Zaman, M. Reeder, and M. Samimy. This permitted measurements to be readily made very close to the exit plane of the jet; the present data are the first to be reported in this near region. These measurements included cross-vane vorticity visualizations as close as x/b=0.1. The scale of the experimental apparatus also reduced the spatial resolution problems of x-array hot-wire probes that were experienced by Zaman et.al. (1994).

Four experimental procedures were used in this work to interrogate the flow field. First, static pressure measurements were made upstream of the tunnel exit. This gave insight into the vorticity sources of the flow field and how geometry changes could be utilized to enhance the tab's effect. Second, a cross-vane vorticity probe was used to determine the nominal borders of the streamwise vorticity in the very near field of the tabbed jet, i.e. x/b=0.1 to 0.4. Third, a single sensor probe was used to determine the streamwise velocity field for the untabbed jet at x/b=0.7,1.2, and 2.0, as well as for the simple and modified jets at x/b=0.7. Finally x-array hot-wire probes were used to provide u,v, and w measurements at x/b=1.2 and 2.0 for the primary tab jet and modified tab jet. Note that at x/b=0.7 the flow angle fluctuations were found to be too large (i.e. greater

than ±36 degrees) to allow the use of x-array hot-wire probes. These data were then processed to provide the spatially averaged streamwise vorticity, ω_x, at those locations.

Three geometries were investigated, see Figure 1.4. The untabbed jet, Figure 1.4a, provided the reference case for the basic flow field. The primary tab geometry, Figure 1.4b, has one primary tab. This geometry (an equilateral triangle oriented 45 degrees downstream) served as a connection to the past work of K. Zaman, M. Reeder and M. Samimy. Note that the percentage of the exit area to the projected tab in the y-z plane was nominally 3 times greater in this study. A primary goal of this study was to provide a basis for enhancing effects of the tabs in jet flows. The modified tab geometry was created by the addition of two secondary tabs, one on each side of the primary tab, see Figure 1.4c. A rationale for the changes in the flow field for the modified tab geometry when compared to the primary tab geometry will be given and further insights into the physics of tabs will be discussed.

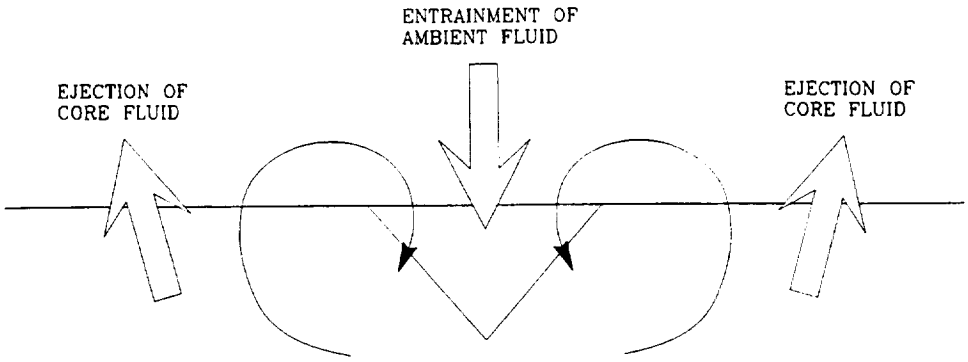

Figure 1.1: Inferred flow directions from action of the streamwise vorticity.

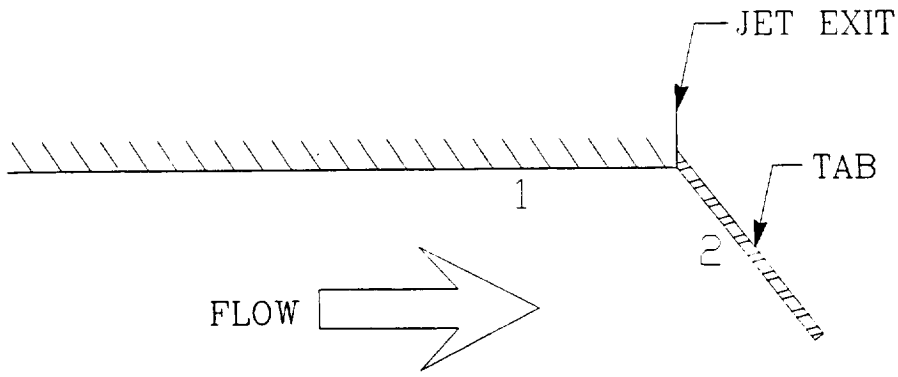

Figure 1.2: Cross section of the centerline of the tabbed jet.

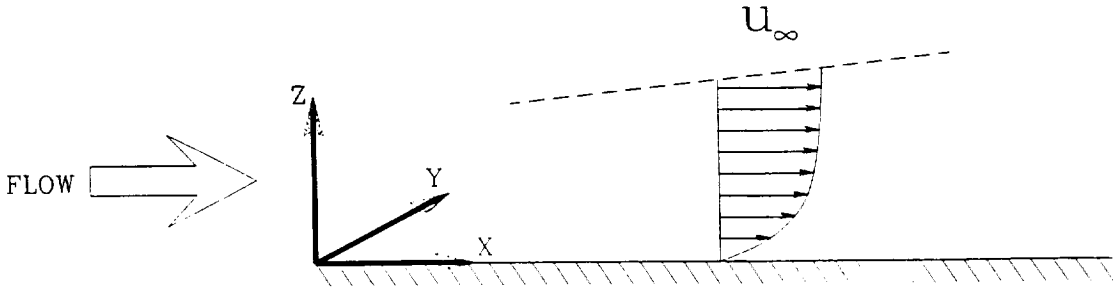

Figure 1.3 Schematic of a typical boundary layer.

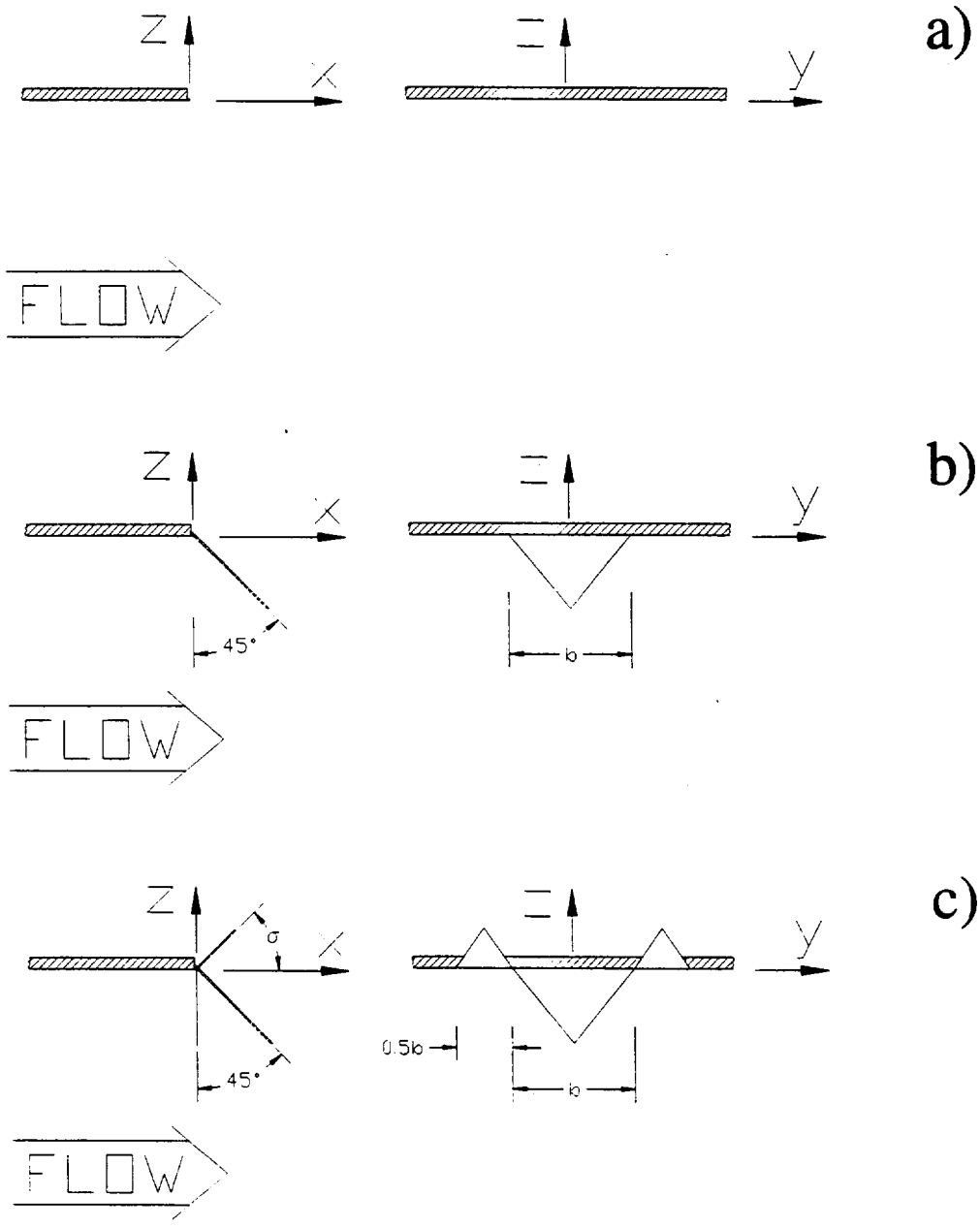

Figure 1.4: Geometry definitions a) untabbed, b)simple, c)modified.

2. EXPERIMENTAL APPARATUS

2.1 Flow System

An Engineering Laboratory Design closed loop wind tunnel, shown in Figure 2.1, was used as the flow system for this study. The unmodified tunnel has a clear plastic test section of 61cm x 61cm x 244cm (2'x2'x8'). The flow is driven by a JOY 50 hp AC motor with a constant speed of 1770 rpm. Adjustments to the flow speed are made via a manual controller which varies the angle of attack on the fan blades. Tunnel cooling is accomplished using a fin/tube heat exchanger with building water as the cooling medium. The plenum-test section contraction ratio is 6.25. Static taps upstream and downstream of the contraction provided the reference velocity U_{up}. The calibration curve for this tunnel was found using a single sensor hot-wire probe located at the exit of the tunnel extension, see Figure 2.2. The calibration curve is shown in Figure 2.3.

The tunnel was modified by removing the test section creating a Goettingen style wind tunnel as shown in Figure 2.2. A 24 cm long tunnel extension, shown in Figure 2.4, was placed at the tunnel "exit". Two rows of static pressure taps in the x-direction were placed on the top surface of the extension. The top surface was machined to allow the position of the top surface (and hence the static pressure taps) to be variable in the y-direction. This permitted $P(x,y)-P_{atm}$ to be measured upstream of the tab. The exit plane was machined to allow the attachment of the tabs. The entrance to the tunnel was fitted with half round flow conditioners. Cheese cloth with a wire mesh backing was placed over the inlet to prevent airborne particles from entering the modified tunnel.

A four degree of freedom traverse system, shown in Figure 2.5, was in place in the wind tunnel test section. The system allows for x,y,z and θ (about the z-axis). The probe support, seated on linear bearing blocks, was driven by high precision lead screws. An IBM/XT clone was used in conjunction with an OMNITECH ROBOTICS MC-3000 and MC-1000 controller board to provide the motion control. Five YASKAW 100 watt DC servo motors with optical encoders were used to drive the lead screws. The servo motors have a resolution of 36000 counts per revolution. The accuracy of the traverse in the x,y,z directions was found to be 0.1mm. Probes were located by sighting the probe location with respect to the center top surface of the tunnel extension. Extensions for the probe holder were machined to allow measurements to be made above the top of the tunnel.

2.2 Experimental Configuration Definitions

Figure 1.4 defines the geometries used in this study. The "untabbed" flow was used as the reference flow field. This flow field can be characterized as a square free jet. The "primary tab geometry" was created by the addition of one "primary" tab to the top surface of the untabbed jet. The primary tab was placed on the top surface of the tunnel and was oriented 45 degrees downstream of the exit plane as shown. The primary tab (machined from 3.14mm (1/8") thick stock) was an equilateral triangle with a base length, b, of 200 mm. The modified tab geometry consisted of the primary tab with two secondary tabs placed symmetrically about the center line of the primary tab. The secondary tabs had a base length of 100mm or 0.5b; they were also machined from 3.14 mm (1/8") thick stock. The location of the secondary tabs as well as the angle at which

they were positioned was variable. For both tabbed geometries the percent blockage of the jet exit was calculated to be 6.6% and was determined from the projected area of the primary tab in the y-z plane in the jet core.

2.3 Data Acquisition and Processing Systems

Data acquisition was performed using an Analogic Fast-16 A/D card with an IBM 486-66 PC clone. The A/D card had a resolution of 16 bits with a range of ±10 volts. This allows an A/D resolution of 0.31 millivolts. The inherent noise of the A/D board was found to be ±1 bit. The maximum sample rate of the system was 1 MHz. An eight channel sample and hold card was used in conjunction with the A/D card to provide eight channels of true simultaneous sampling.

The data were processed on the indicated PC as well as on a DEC ALPHA AXP-150 computer system.

2.4 Pressure Transducers

Two pressure transducers were used to take the reference and static pressure measurements for this study. A 1 Torr MKS Baratron pressure transducer was used to provide the reference pressures for the normalization of all hot-wire data as well as for calibrating the hot-wire sensors. Additionally the Baratron was used to measure the static pressure, $P(x,y)-P_{atm}$, upstream of the tunnel exit. A Validyne DP15-20 pressure transducer was used to provide the reference pressure during the static pressure surveys.

2.5 Hot-Wire Anemometers Anemometers

Hot-wire data were taken using several constant temperature anemometers. The single sensor surveys, as well as some of the x-array probe surveys, were accomplished using DISA 55M10 anemometers. The noise on these anemometers was found to be on the order of ±2.0 millivolts peak to peak. The typical frequency response was found to be 48 KHz at 10.5 m/s flow speed. The remainder of the data were taken using TSI 1750 anemometers. The noise level on these anemometers was found to be ±1.5 millivolts with a frequency response of 16 KHz at 10.5 m/s.

All hot-wire probes used in this study were fabricated (in-house) at the Michigan State University Turbulent Shear Flows Laboratory. Individual hot-wire sensors were constructed from 5μm diameter tungsten wire. A schematic of a typical single sensor probe is found in Figure 2.6. The wire spanned a length of 3mm with a 1mm active sensing region centered between two 1mm regions of nominally 50μm diameter copper plated tungsten. The active region of the sensor had a length to diameter ratio of 200. Hot-wire sensors were operated with an overheat value of 1.7. Nominal cold resistances of the wires were found to range from 3.5 to 4.5 ohms.

The sensors of the x-array hot-wire probes were the same as those for the single sensor probes described above. Two x-arrays were used simultaneously to provide u,v and u,w measurements at each location. The u values from the two arrays were averaged to provide the measurement of u.

All hot wire data were temperature compensated to reduce errors caused by a change in flow temperatures between the calibration and the measurements. Temperature measurements were conducted using a thermistor with a sensitivity of 2.03 K/Kohm at

293 K. At 293K the thermistor had an accuracy of ±0.2K and a frequency response of 10Hz. All temperature changes were assumed to be long term (on the order of hours) and therefore the response time of the thermistor was considered sufficient.

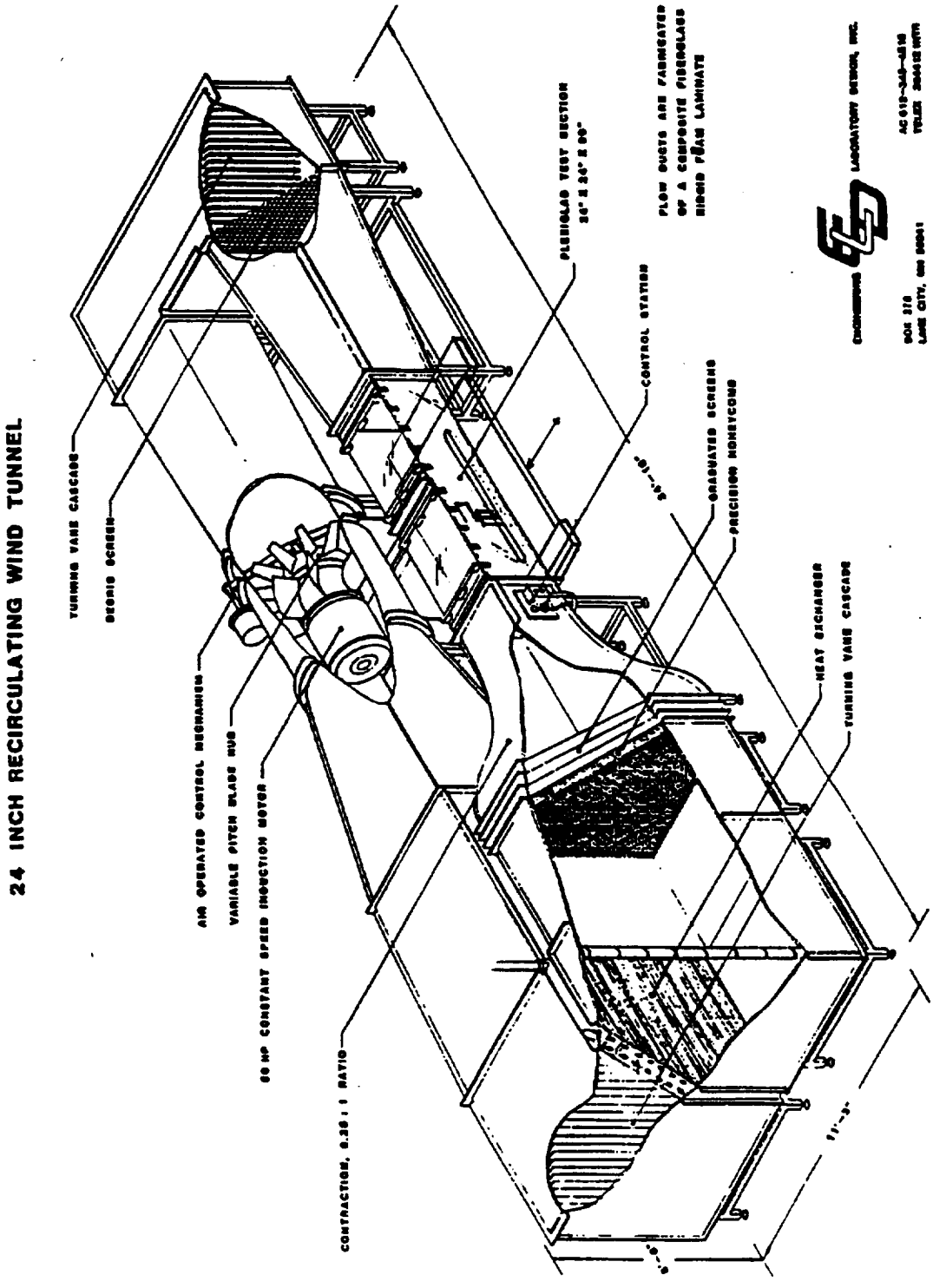

Figure 2.1: Schematic of experimental facility.

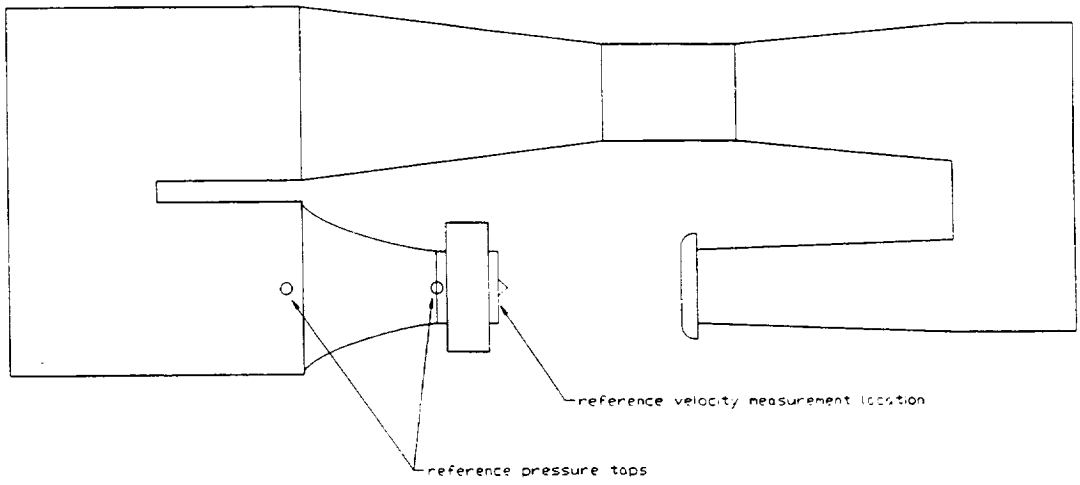

Figure 2.2: Schematic of the modified flow facility.

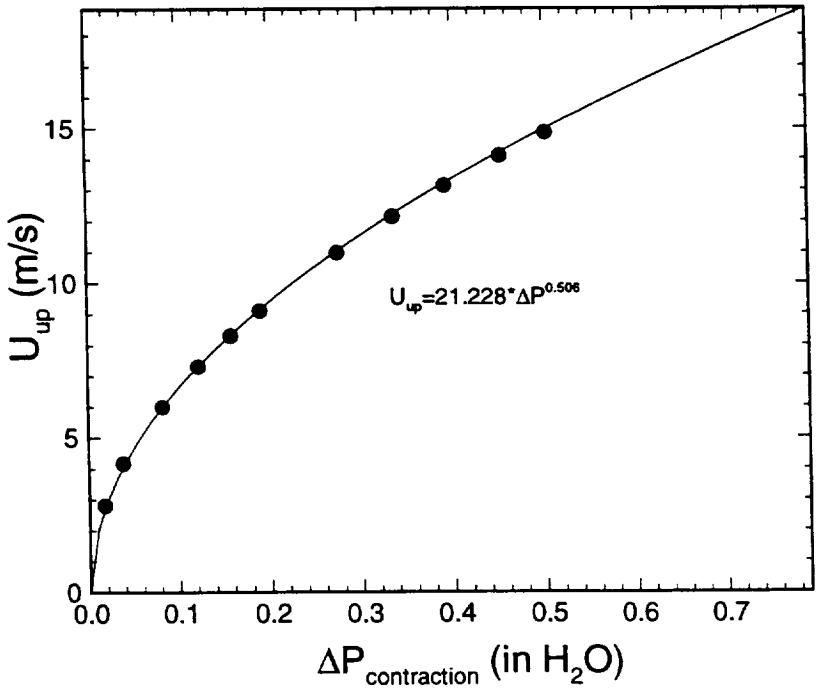

Figure 2.3: Velocity calibration curve for flow facility.

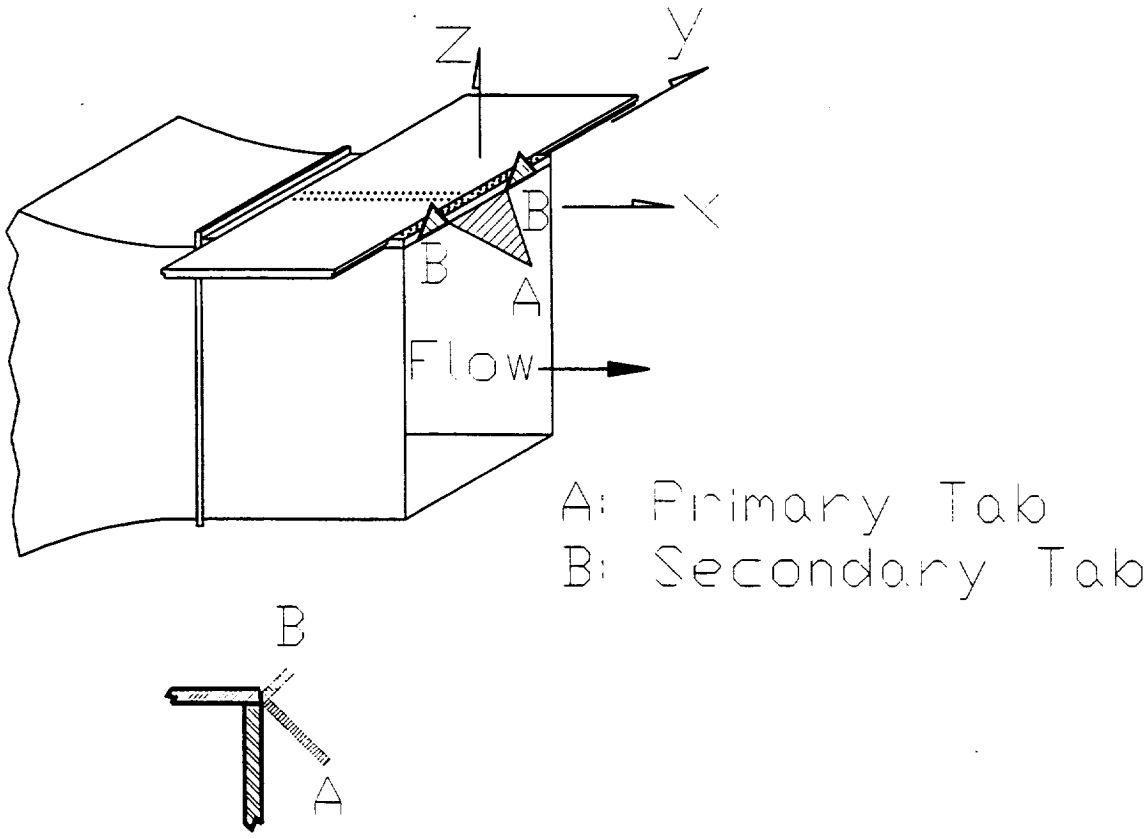

Figure 2.4: Schematic of the tunnel extension.

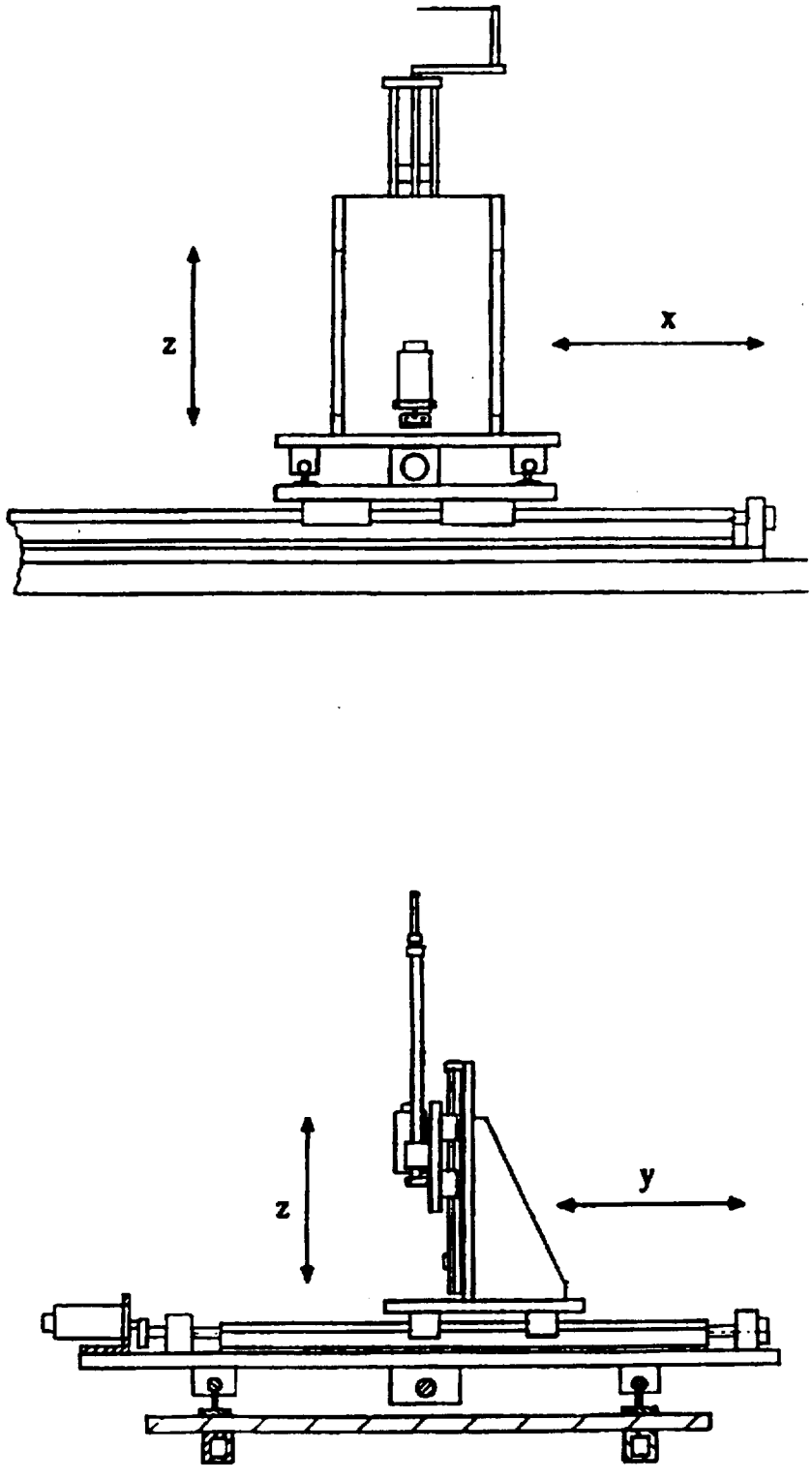

Figure 2.5: Schematic of the probe traverse system.

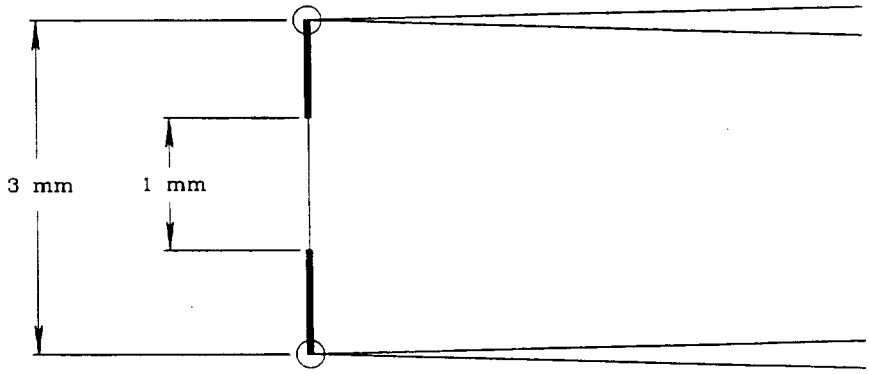

Figure 2.6: Schematic of single sensor hot-wire probe.

3. DATA PROCESSING METHODS AND CONSIDERATIONS

3.1 Introduction

The information presented in sections 3.2-3.4 describes the protocols for the use and calibration of the hot-wire probes in this study. The first two sections deal with the processing algorithms and calibration methods for the probes. The rationale for the use of each probe in different measurement locations in this study are presented in section 3.4 . Sections 3.5-3.7 deal with the cross-vane vorticity probe and further data reduction methods for all data in this study.

3.2 Single Sensor Calibration and Processing Algorithms

Data from the single sensor probes were processed using the modified Collis and Williams (1959) relationship:

$$E^2 = A + BQ^n \tag{3.1}$$

The measured hot-wire voltages were converted into velocities by solving (3.1) for the flow velocity Q.

A probe was calibrated by exposing the sensor to a steady flow and sampling the resulting anemometer output voltage and a reference pressure voltage. A MKS Baratron pressure transducer was used to measure the pressure differential in the calibration facility which provided the measured reference speed Q_m. Six flow speeds, ranging from 1.5 m/s to 13 m/s, were used in each calibration. Note, 1.5m/s represented the minimum

measurable speed in the calibration unit, while 13 m/s represented a velocity that exceeded the highest expected velocity in the flow field.

The calibration data were then transformed into E^2_{hw} and Q^n_m where the subscripts "hw" and "m" represent "hot-wire" and "measured" respectively. A least squares linear fit was performed on the transformed data to calculate the constants A and B used in (3.1). The standard deviation of the calibration data was calculated by

$$sd = \left(\frac{1}{N} \sum_{1}^{N} (Q_{calculated} - Q_m)^2 \right)^{1/2} \qquad (3.2)$$

where $Q_{calculated}$ was the velocity calculated from the measured anemometer voltage using the fit A and B for the given n and (3.1). The coefficient n was varied from 0.2 to 0.7 to determine the calibration coefficients that minimized the standard deviation. Figure 3.1 shows the affects of changing n for a given set of calibration data. The calibration data became most linear as the "best" n was approached . Typical "best" values of n ranged from 0.4 to 0.5.

3.3 X-Array Calibration and Processing Algorithms

An x-array was used to provide two components of velocity in the "plane" of the probe. Note that the "plane" of the probe refers to the plane parallel to the two wires of the probe, see Figure 3.2. The processing of an x-array hot-wire probe required the two voltages from the wires in the probe to be known at the same instant. These two voltages were processed simultaneously to provide measurements of the flow speed, Q(t), and angle, $\gamma(t)$ in the plane of the probe.

The simplest x-array processing algorithm, termed the "cosine law", was based on the concept of the effective cooling velocity (Bradshaw (1975)). This relationship assumed that a hot-wire sensor was cooled only by the velocity component perpendicular to the wire, Q_{eff}. The effective cooling velocity, Q_{eff}, for a hot-wire was determined by the relation

$$Q_{eff}=Q\cos(\beta-\gamma). \tag{3.3}$$

The angle γ, termed the "flow angle", was defined as the angle between the probe axis and the in-plane velocity vector as shown in Figure 3.2. The angle β was the angle described by a line drawn perpendicular to the wire and probe axis. The effective β was determined using the calibration data as described in Appendix A.

Expansion of (3.3) using a two angle formula yielded

$$Q_{eff}=Q[\cos(\beta)\cos(\gamma)+\sin(\beta)\sin(\gamma)]. \tag{3.4}$$

Substituting the values

$$u=Q\cos(\gamma) \tag{3.5}$$

$$v=Q\sin(\gamma) \tag{3.6}$$

into (3.4) yielded

$$Q_{eff}=u\cos(\beta)+v\sin(\beta). \tag{3.7}$$

Equation (3.7) yielded one equation with two unknowns, u and v, for each sensor. The two sensors in the x-array were used simultaneously to solve for u and v by

$$Q_{eff+} = u\cos(\beta_+) + v\sin(\beta_+) \tag{3.8}$$

and

$$Q_{eff-} = u\cos(\beta_-) + v\sin(\beta_-). \tag{3.9}$$

The terms Q_{eff+} and Q_{eff-} in (3.8) and (3.9) were defined from the calibration data and measured hot-wire voltage as

$$Q_{eff+} = \left[\frac{E_+^2 - A_+(\gamma=0)}{B_+(\gamma=0)/\cos(\beta_+)^{n_+}}\right]^{\left(\frac{1}{n_+(\gamma=0)}\right)} \tag{3.10}$$

and

$$Q_{eff-} = \left[\frac{E_-^2 - A_-(\gamma=0)}{B_-(\gamma=0)/\cos(\beta_-)^{n_-}}\right]^{\left(\frac{1}{n_-(\gamma=0)}\right)}. \tag{3.11}$$

Where - and + indicate the voltages and coefficients associated with the -β and + β sensors. Note that in (3.10) and (3.11) A, B and n values were only required for γ=0. Calibration of an x-array for use with the cosine law could therefore be accomplished using the same protocol as described for a single wire if β were known. The in-plane flow velocity and flow angle were defined from u and v as

$$Q=(u^2+v^2)^{1/2} \tag{3.12}$$

and

$$\gamma=\tan^{-1}(v/u). \tag{3.13}$$

This routine has been shown to be accurate for flow angles up to ± 12 degrees (Foss et. al.(1986)).

Historically, the "modified" cosine law was introduced as an attempt to increase the effective range of an x-array (Champagne, ... and Hinze (1959, 1975). In the cosine law it was assumed that the wire responded only to the flow which was perpendicular to the wire. This assumption became less valid as the flow angle was increased for a finite length wire. The modified cosine law accounted for this affect by adding a term to the effective velocity as:

$$Q_{eff}=Q(\cos^2(\beta-\gamma)+k^2\sin^2(\beta-\gamma)). \quad (3.14)$$

Note that the $k^2\sin^2(\beta-\gamma)$ term was included to account for the transverse cooling velocity and that the term k^2 could be determined using calibration data for the probe. This routine has been used extensively, however it also has some disadvantages. Specifically, the processing algorithm assumed A, B and n values were constant for all flow angles. This assumption has been to shown to be incompatible with experimental calibration data (Foss et.al. (1986)). Note this same limitation was also present for the cosine law algorithm. In addition, the values for k^2 determined from the calibration data have often been determined to be negative from the calibration data.

An alternate processing algorithm, described in Foss et. al.(1995), was used in this work. In this algorithm it was assumed that the wire which was more perpendicular to the flow direction was more responsive to the flow speed; therefore, that wire was designated the "speed wire". Conversely, the wire which was more tangent to the flow angle was more responsive to angle variations, and this wire was designated as the "angle wire". Wire 1 was the speed wire and wire 2 was the angle wire for the velocity vector shown in Figure 3.2.

This processing algorithm required extended calibration data. Specifically, the angle of the probe with respect to the flow was varied at a given speed. This provided speed and angle calibration data (i.e. $E(Q,\gamma)$). These data were fit at each calibration angle to the modified Collis and Williams form by

$$E^2(Q,\gamma)=A(\gamma)+B(\gamma)Q^{n(\gamma)}. \quad (3.15)$$

The best fit n was determined for the calibration data at each angle as described in section

3.2. A typical set of calibration data, plotted as E versus Q, is shown in Figure 3.3. These data clearly illustrate the probe response dependence on both angle and speed.

A relationship for the wire voltage versus flow angle for a constant speed was developed for this processing algorithm. Namely the function $\eta(\gamma)$ at a fixed Q was defined as

$$\eta = \frac{E(Q,\gamma)}{E(Q,0)} - 1. \tag{3.16}$$

Using the curves described by (3.15) $\eta(\gamma)$ was defined for any arbitrary speed at all calibration angles. In this work, 51 curves of flow angle, γ, versus η were defined for even speed increments from 0.25 m/s to the highest calibration speed, nominally 13 m/s. This allowed for the rational interpolation of the calibration data between the calibration speeds. Figure 3.4 shows a typical γ versus η curve for an arbitrary speed. A fifth order polynomial was used to describe the curve.

The enhanced sensitivity of the "angle wire" to the pitch angle (γ), in contrast to the insensitivity of the "speed wire" is clearly illustrated in Figure 3.4. Specifically, for flow angles greater than zero the calibration data were spaced over a range of η from -0.09 to 0. For negative flow angles these data ranged from η=0 to 0.045. This clearly illustrated that there was a greater resolution of flow angle for a positive angles with this wire. Conversely, a change in flow angle did not create as great a change in the hot-wire voltage indicating it was more sensitive to the flow speed for negative flow angles.

The following processing algorithm was developed to use the speed wire/ angle wire concept described above. The speed wire and angle wire were determined using an initial estimate of the flow angle, γ_{old}. In this work the initial estimate of the flow angle for the

speed wire/angle wire algorithm was provided by first using the cosine law to process the data pairs. A new estimate for the speed, Q_{new}, was made using the speed wire with the A,B, and n values for the calibration angle closest to γ_{old}. The variable η was determined for the angle wire using its voltage, E, and (3.16). Two estimates for the new flow angle were made using the two γ versus η curves closest to the new flow speed Q_{new}. The new flow angle, γ_{new}, was found by linear interpolation between the two angles based on the flow speed.

This processing algorithm was iterative. At the end the algorithm the new estimates for the flow speed and angle became Q_{old} and γ_{old} for the next iteration pass. In this work the solution was iterated 5 times to achieve the final values for Q and γ. The speed wire/ angle wire processing algorithm has been shown to increase the effective range of an x-array to ±36 degrees for sufficiently high flow speeds (Foss et. al. (1995)).

Calibration of the x-array probe was accomplished using six speeds, ranging from 1.5m/s to 13m/s, and thirteen angles, ranging from -36 to +36 degrees. Note that the calibration angle range was larger than the effective angle range to permit full resolution of the angles within the effective range.

It is important to note that an x-array probe will also respond to a velocity component which is perpendicular to the measurement plane. The effect of this component, typically referred to as the "bi-normal" component, is present in the x-array data contained within this work.

3.4 Determination of the Use of the Single Sensor and X-Array Probes

The decision to use a particular type of hot-wire probe was based upon the flow conditions, the data to be acquired, and the limitations of the probe.

In this study, the single sensor hot-wire probe was used to measure the streamwise velocity component for the untabbed geometry at x/b=0.7,1.2 and 2.0. Note that a single sensor probe was assumed to respond to two components of velocity which were perpendicular to the sensor wire. Specifically in this work, the sensor will respond to a streamwise velocity component, u, and to the transverse velocity component, w, because the sensor was parallel to the z-axis. The magnitude of the velocity measured at an instant by this probe will be

$$Q(t) = (u(t)^2 + w(t)^2)^{1/2}. \tag{3.21}$$

The average value as well as the fluctuating value will therefore be a result of the two velocity components. If either $\overline{u}$ or $\overline{w}$ were equal to zero than the average value of (3.21), $\overline{Q}$, will be identically $\overline{w}$ or $\overline{u}$ respectively. The untabbed jet flow field had nominally one mean velocity component, $\overline{u}$, which allowed accurate average streamwise velocity measurements to be made with the single sensor probe. The fluctuating values, which showed $w' \leq u'$, allowed a reliable estimation of $\tilde{u}$ to be made using the single sensor probe.

The flow pitch angle fluctuations were too large (i.e. greater than ±30 degrees) at x/b=0.7 to allow the use of x-arrays for the primary tab and modified tab geometries. Single sensor measurements were made at this location for these geometries so that qualities of the flow field could be inferred. This inferential process was limited by the non-zero $\overline{w}$ in both tabbed jet geometries. Specifically, these data will contain the

combined effects of u(t) and w(t) in both the mean and fluctuating values as indicated by (3.21).

The flow pitch angles were found to be less severe at x/b=1.2 and 2.0 for the primary tab and modified tab geometries; this permitted the use of x-array probes in these locations. At these locations it was possible to measure u(t), v(t), and w(t). Note that in order to resolve u,v, and w, two x-arrays, with their measurement planes horizontal and vertical, were used in the flow field simultaneously. The two x-arrays were separated by a distance of nominally 2.12mm from the center of the sensing arrays. The average streamwise velocity value, $\bar{u}$, was computed by averaging the streamwise velocity data from both x-arrays. The x-array hot-wire probe allowed the computation of the average velocity values, correlations, cross-correlations, two normal stresses, and one shear stress, to be made for each x-array. Note that the sensors on the x-array hot-wire probe will respond to the velocity component perpendicular to the plane of the x-array (the "bi-normal" velocity). In this study no attempt was made to correct for this velocity component.

Figure 3.5 was included to provide a comparison of the streamwise velocity measurements of the two probes. Note that single sensor hot-wire probe was held such that the sensor was parallel to the z-axis for all data in this work and therefore responded to the u(t) and w(t) velocity components. Figure 3.5, taken from the data of the modified geometry at x/b=1.2, showed that the single sensor and x-array hot-wire probe measure the same average streamwise velocity along the side wall of the tunnel where the transverse velocity was small, i.e. $\overline{w} << \bar{u}$. However, in the region above the tunnel exit (i.e. +z) the single sensor hot-wire probe over estimated the magnitude of the streamwise

velocity. This was expected since the magnitude of $\overline{w}$ was significant in this region (i.e. $\overline{w} \approx 0.15\ \overline{u}$) and therefore $\overline{u} < Q$.

3.5 Streamwise Vorticity Calculations

The spatially averaged streamwise vorticity, ω_x, was defined as:

$$\omega_x = \frac{\partial \overline{w}}{\partial y} - \frac{\partial \overline{v}}{\partial z}. \tag{3.22}$$

Thus, the spatially averaged streamwise vorticity was calculated from the appropriate partial derivatives of the $\overline{v}$ and $\overline{w}$ velocity fields which were computed using a second order finite difference method. The interior points were central differenced using (3.28) of Anderson (1984) by:

$$\frac{\partial a}{\partial h})_i = \frac{a_{i+1} - a_{i-1}}{2\,\Delta h} \tag{3.23}$$

while boundary points were either forward or backward differenced depending on the boundary using (3-29) of Anderson (1984) by:

$$\frac{\partial a}{\partial h})_i = \frac{-3a_i + 4a_{i+1} - a_{i+2}}{2\,\Delta h} \tag{3.24}$$

and (3-30) of Anderson (1984) by:

$$\frac{\partial a}{\partial h})_i = \frac{3a_i - 4a_{i-1} + a_{i-2}}{2\,\Delta h}. \tag{3.25}$$

Note, h was the spatial distance between data grid points. This method was found to give comparable results to fitting the data and taking a derivative of the fit curve.

3.6 Cross-Vane Vorticity Probe

The very near field of the jet was defined as the area from the physical exit of the tunnel, x/b=0, to the downstream plane which was described by the tip of the primary tab, see Figure 3.6. The tip was nominally located at x=0.61b. In this region the angle range of the flow pitch angles was greater than ±30 degrees. A cross-vane vorticity probe was used in this region to provide qualitative information about the streamwise vorticity. Figure 3.7 is a schematic of the cross vane vorticity probe. This probe was placed into the flow such that the probe axis was in the streamwise direction. The blades on the probe rotated in the presence of nonzero streamwise vorticity, ω_x, (with a sufficient magnitude to overcome the friction of the device) as described by (3.22). In this study the probe was used in a qualitative manor. Specifically, it was noted which direction the probe spun and if the probe spun "fast" or "slow" at each measurement location. The data presented in section 5.3.13 represented the nominal boundaries of the regions of streamwise vorticity from x/b=0.1 to 0.4. The friction in the probe did not allow observations to be made for streamwise distances greater than about x/b=0.4.

3.7 Statistical Calculations

The data presented within this study were a result of single point measurements. Each time series was processed to provide average and fluctuating values at one measurement location. The mean and mean square values were defined for a time series of data as

$$\overline{g} = \frac{1}{N}\sum_{i=1}^{N} g_i \tag{3.26}$$

and

$$\overline{(g')^2} = \frac{1}{N-1}\sum_{0}^{N}(g_i - \bar{g})^2 \tag{3.27}$$

Finally the rms fluctuating value was defined as

$$\tilde{g} = \overline{(g')^2}^{\frac{1}{2}} \tag{3.28}$$

Data for both the single sensor and x-array hot-wire measurements were acquired at a variety of sampling rates for 30 seconds. The sample time corresponded to 1575 tab base lengths units passing the tunnel exit with a nominal approach velocity of 10.5 m/s. Pressure data were taken at a sample frequency of 200Hz for 30 seconds.

These data were primarily represented in contour form to allow global features of the flow field to be represented. Three plots of data acquisition grids are presented in Figure 3.8 to provide a frame of reference as to the data point spacing used to form the contour plots. The first of these plots, Figure 3.8a, shows the data acquisition grid for the upstream pressure surveys. Data were acquired with increments of $\Delta x=\Delta y=0.1b$. Figure 3.8b shows the grid spacing for the hot-wire surveys conducted at x/b=0.7. These data were acquired with $\Delta y=\Delta z=0.05b$. Finally, Figure 3.8c represents the data acquisition spacing for hot-wire surveys conducted at x/b=1.2 and 2.0. These surveys were conducted with a spacing of $\Delta y=\Delta z=0.075b$.

3.8 Normalization of Data

All quantitative data are presented in non-dimensional form. The lengths were non-dimensionalized by the base length of the tab, b, as

$$K^*=K/b \tag{3.29}$$

where K represents any length measure in the flow field. Average and fluctuating velocity values were normalized with the approach velocity, U_{up}, by

$$\Phi^{*}=\Phi/U_{up} \tag{3.30}$$

where Φ is a velocity statistic in the flow field. The streamwise vorticity values were normalized with the approach velocity and the base length of the tab by, b/U_{up} as

$$\omega^{*}_{x} = \overline{\omega_x} \, (b/ U_{up}). \tag{3.31}$$

Finally the gage pressure values were made non-dimensional by the dynamic head of the approach flow as

$$P^{*}=P/0.5\rho U^{2}_{up}. \tag{3.32}$$

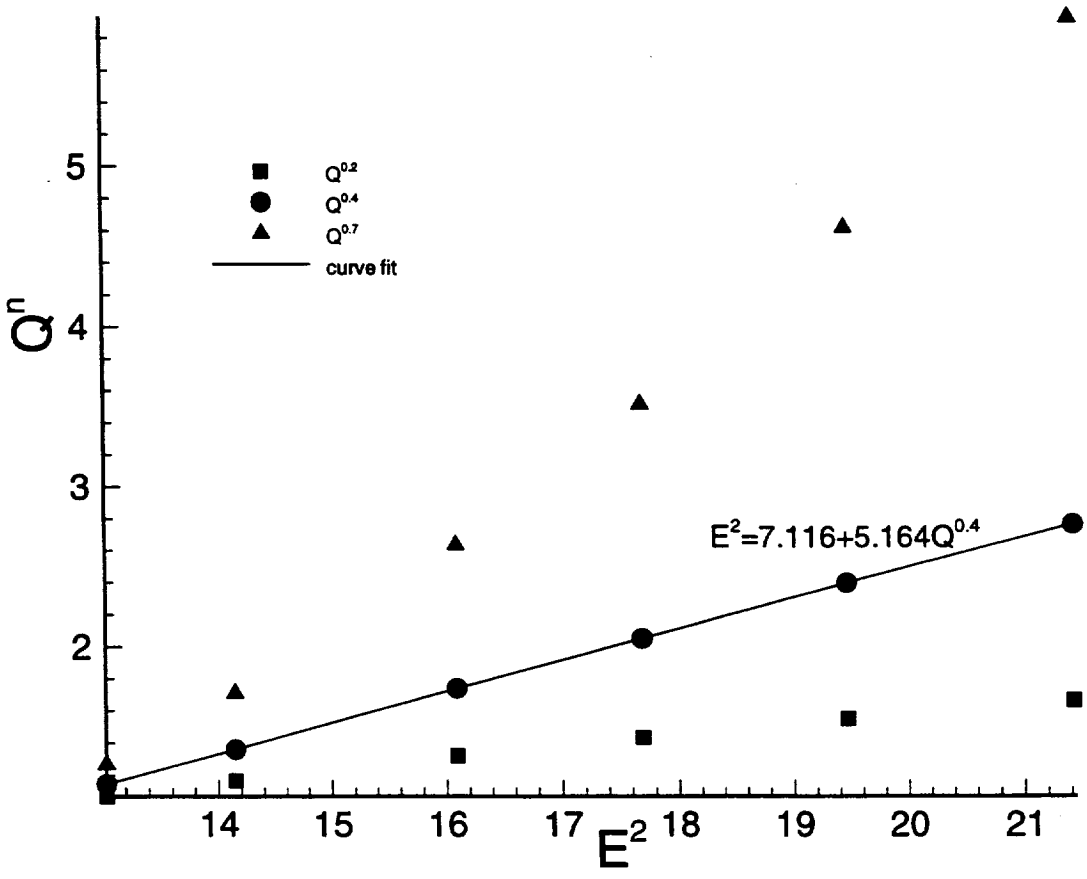

Figure 3.1: Hot-wire calibration data with changing n values.

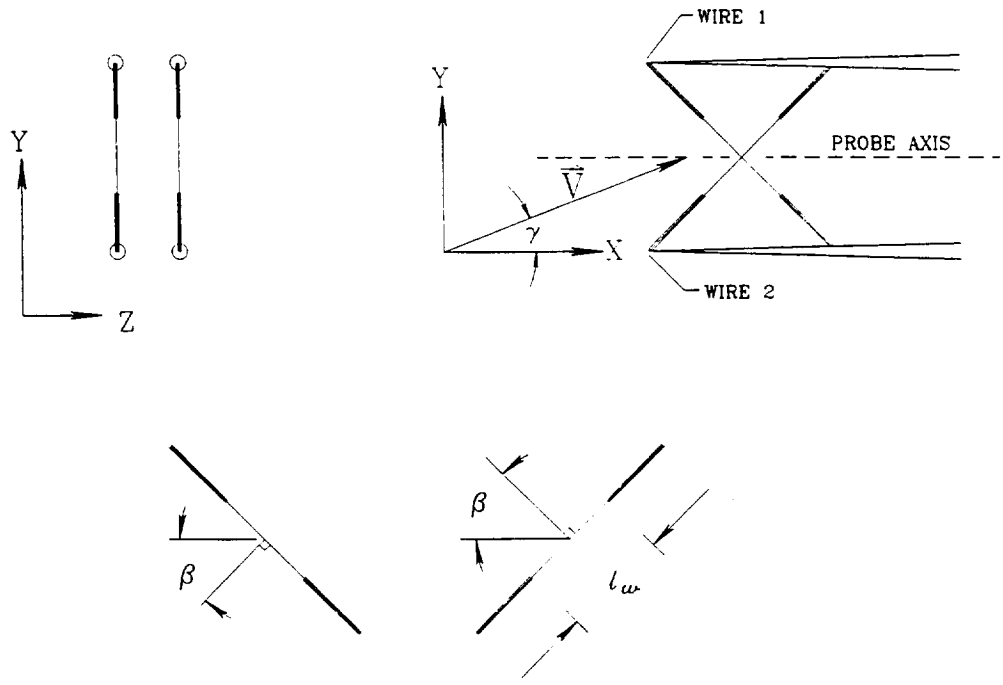

Figure 3.2: Schematic of x-array hot-wire probe.

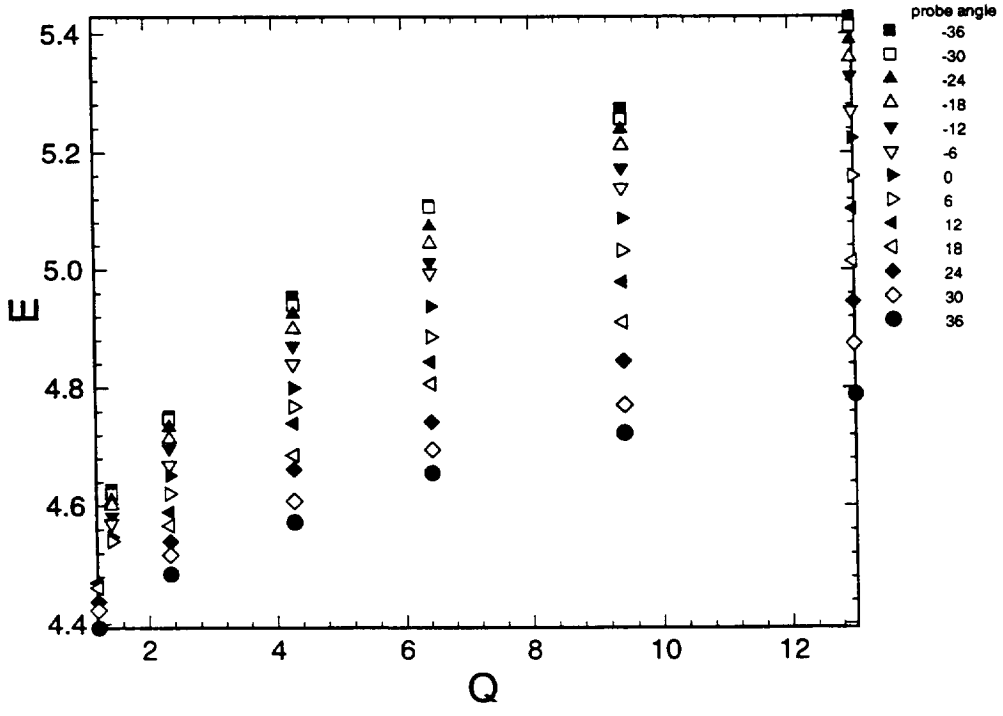

Figure 3.3: E versus Q from a typical x-array calibration.

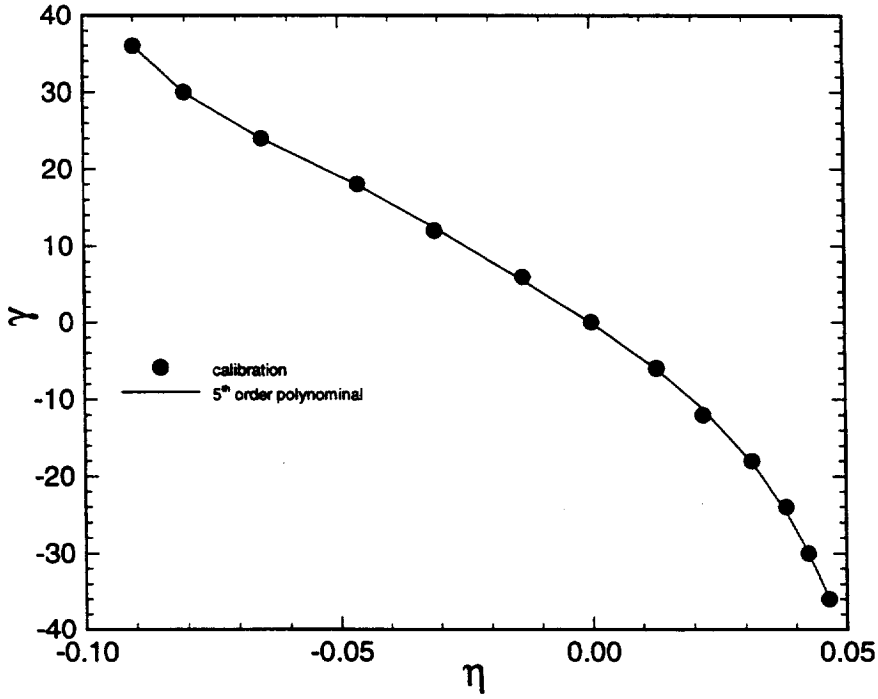

Figure 3.4: γ versus η data for x-array calibration. Note: Q=6.2 m/sec.

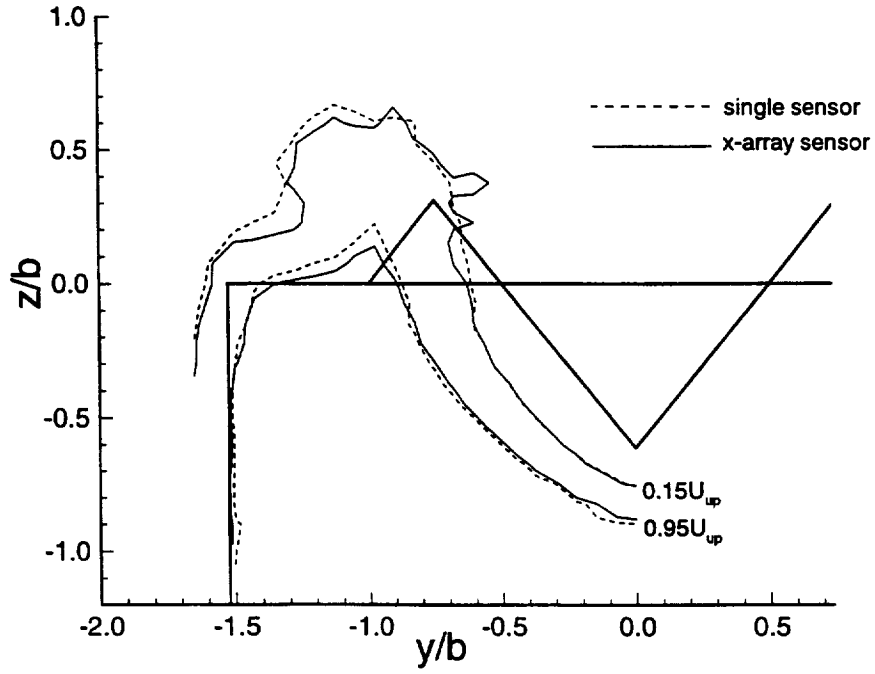

Figure 3.5: Comparison of streamwise velocity contours for the single sensor and x-array hot-wire probes.

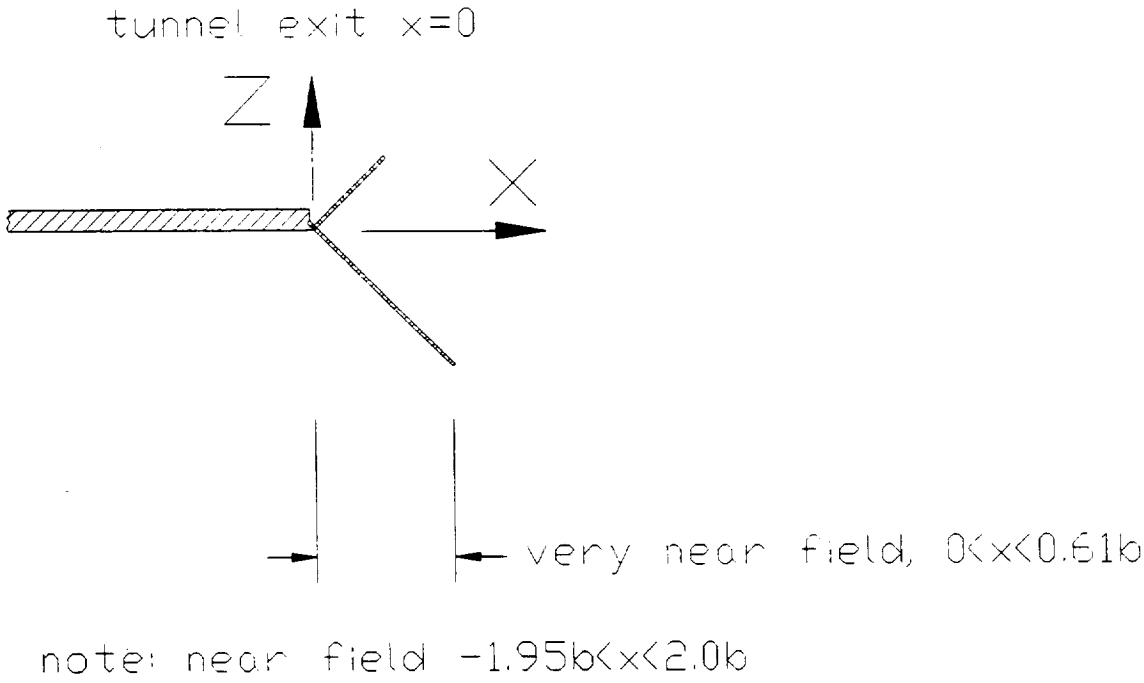

Figure 3.6: Definition of the "very near field".

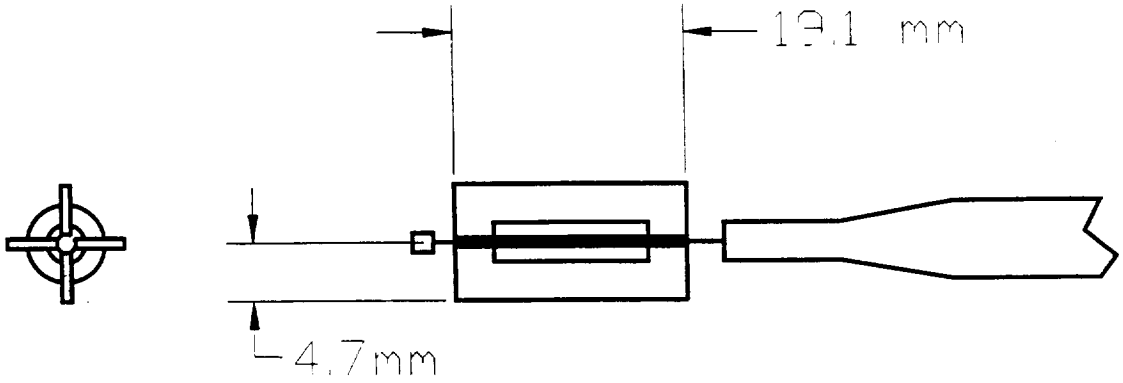

Figure 3.7: Schematic of cross-vane vorticity probe.

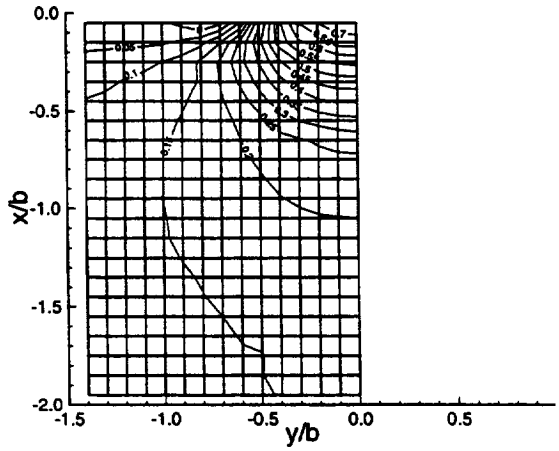

(a)

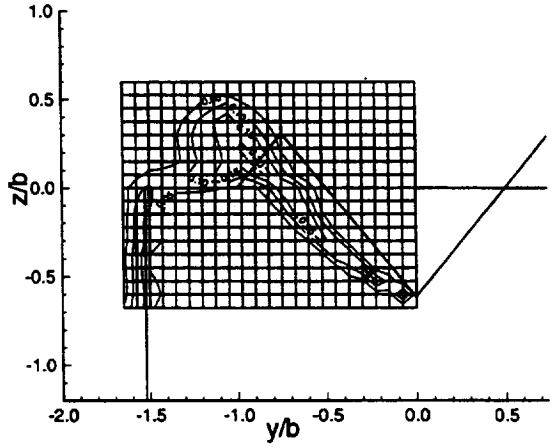

(b)

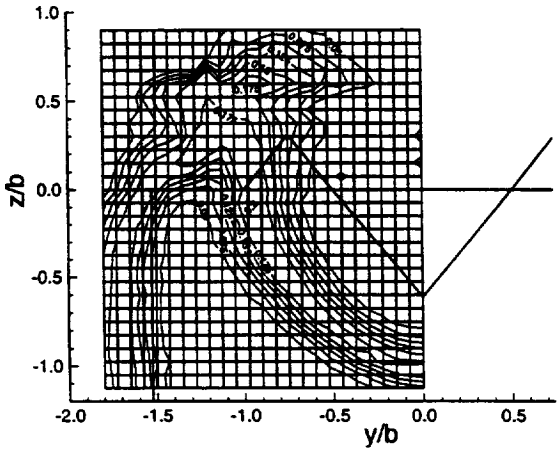

(c)

Figure 3.8: Data acquisition grid spacing: a) static pressure, b) hot-wire at x/b=0.7, c) hot-wire at x/b=1.2 and 2.0.

4. UNCERTAINTY CONSIDERATIONS

4.1 Pressure Measurements

Data taken with the 1 Torr MKS Baratron had an associated uncertainty of ±0.08% of the measured value(MKS Instruments (1994)). The ±0.08% level of uncertainty corresponded to an uncertainty of 0.04cm/s (0.004% of U_{up}) in the measurement of the approach velocity U_{up}. Note, this level of uncertainty was based on a nominal 4.8 volt measurement for an approach velocity of 10.5 m/s. For the measurement of the static pressure field the uncertainty for the Baratron can be taken to be ±0.08% directly. The reference pressures for the static pressure surveys were taken using a Validyne DP15TL pressure transducer. This device had an uncertainty of ±0.5% of the measured value (Validyne Engineering (1978)) which corresponds to a velocity uncertainty of 0.2cm/s (0.02% of U_{up}).

The static pressure measurements on the top surface of the tunnel extension without tabs present provide details about how well the static taps perform in a flow field. Specifically, any physical defects in the taps will provide a greater error in the pressure measurements than will the errors associated with the pressure readings. The pressure data upstream of the tunnel exit for the untabbed geometry (shown in Figure 5.2) show static pressures bounded by the magnitudes $C_p=0 \pm 0.02$. The farther upstream data show a back pressure which is made rational given the boundary layer growth in the tunnel extension. The pressure measurements also show a value of $C_p \approx -0.02$ along the wall. Note that the same pressure tap is used to measure all of the pressures for x=constant locations, therefore the pressure measurements in this region are due to imperfections in

the apparatus (i.e. the side wall/top wall interface) and not these local tap. The pressure measurements at the exit of the tunnel should be equal to zero. The nonzero measurements in this region indicate the uncertainty in the pressure to be ±0.006 as a conservative estimation of the uncertainty due to the tap imperfections. Figure 4.1 shows a typical pressure distribution for a fixed x location with uncertainty bars.

4.2 Hot-Wire Measurements

All hot-wire probes were pre and post calibrated to ensure that the wires did not experience significant drift during usage. Drift values were limited to a maximum of 0.05 m/s for a single sensor probe and 0.15 m/s for the x-array probes. These estimates of drift were calculated by combining the pre and post calibration data to provide calibration constants from the combined data and checking the standard deviations of the combined calibration data.

Single sensor hot-wire calibrations show a typical standard deviation of 0.03 m/s between the measured velocity and the analytical form $E^2=A+BQ^n$, as described in section 3.1. Note that at 10.5 m/s, nominally the approach velocity U_{up}, this level of deviation represents 0.3% uncertainty in the velocity measurements.

The x-array calibrations show a typical deviation of 0.08 m/s, i.e. 0.8% of U_{up}, and an angle variation of 0.1 degree except at the lowest calibration speed (nominally 1.5 m/s) and at the largest angles (± 36 degrees). In these extreme conditions the velocity was recovered to nominally 0.2 m/s and the angle to within 3 degrees. This estimation of the uncertainty in the x-array data was made by taking the calibration data, i.e. voltage at an

known angle and speed, and using the processing routine to calculate the speed and angle. The processed data are then compared to the measured data.

Figure 4.2a shows a typical average velocity traverse with error bars included for illustration. Note the error bars included in this figure were derived from the uncertainty in the calibration data. Figure 4.2b shows the $\tilde{u}/U_{up}$ survey for the same traverse. The error bars included with Figure 4.2b were determined by processing the same data set with the pre and post calibration coefficients separately. The difference between the measurements was found to be $\Delta(\tilde{u}/U_{up}) = 0.003$.

Figures 4.3 and 4.4 show the convergence of the mean and fluctuating statistical properties as a function of sample size in the plume region of the flow (i.e. at y=-b and z≈0.4b) for two data sets with $\bar{u} \approx 0.6U_{up}$ and $\bar{u} \approx 0.3U_{up}$ respectively. Note that the total number of samples n=60,000 was fixed by the sample rate (200Hz) and the total sample time (30 seconds). The data for $\bar{u} \approx 0.6U_{up}$, Figure 4.3a, suggest that the "infinite sample size" mean value can be estimated to be $\bar{u}/U_{up} \approx 0.62 \pm 0.005$ by the convergence pattern. Figure 4.4a also shows $\bar{u}$ as a function of the number of samples for $\bar{u} \approx 0.3U_{up}$. The convergence of the data at this location is less pronounced. The mean value of 0.32, obtained from 60,000 samples clearly does not represent a "converged statistic". From the variation of the "mean values" with increasing sample size, it is also difficult to estimate the true mean value at this point in the flow field: x=2.0b, y=-1.05b, z=0.825. It is instructive that this location is near the peak of the out-flow "plume" to be described below. In contrast, data taken from the outer edge of the jet flow (away from the tab) at x=2.0b, y=-1.8b and z=-1.05b and also for $\bar{u} \approx 0.3U_{up}$ exhibit convergence for as few as

10,000 samples; see Figure 4.5a. This clearly illustrates that different integral scales, and hence strong difference in the number of independent samples for the 30 second period, are present in the distorted and undistorted shear layer.

The convergence of the standard deviation values has also been assessed; these data are shown in Figures 4.3b, 4.4b and 4.5b. It is apparent that fewer samples (30000, 40000, and 10000 respectively) are required for the evaluation of this statistical measure.

The data from the x-arrays was used to provide calculations of the shear stresses in the flow field. Figure 4.5 shows the collapse of $\overline{u'v'}/U_{up}^2$ and $\overline{u'w'}/U_{up}^2$ as a function of the number of samples. (Note these data were calculated from the same measurements used in Figure 4.3.) These plots show the data tending to convergence, although these calculations appear to be oscillating. An estimation of the uncertainty in these data was determined to be ± 0.002 for both quantities.

In this study there are large regions of low velocity with magnitudes that are not within the calibration range. Specifically, the minimum possible calibration speed given the experimental facilities was nominally 1.5 m/s. Measurements of velocities smaller than those of the the calibration data require extrapolation of the calibration data and exhibit a larger uncertainty than do measurements that fall within the calibration velocity range. To minimize the effect of this uncertainty on the results the velocity data are presented in contour form with a minimum streamwise velocity contour of $0.15*U_{up}$. This represents a dimensional value of nominally 1.6 m/s which was within the calibration velocity range.

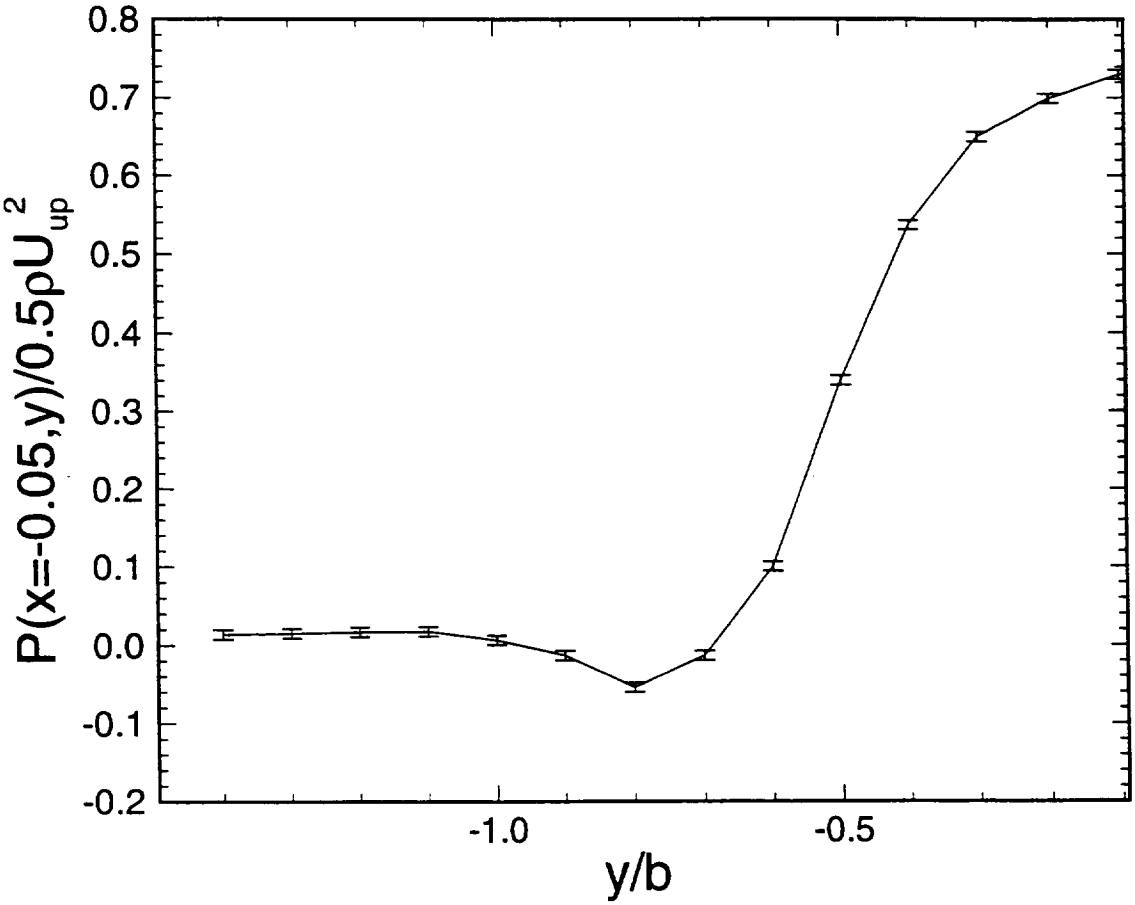

Figure 4.1: Error bar estimate for pressure surveys.

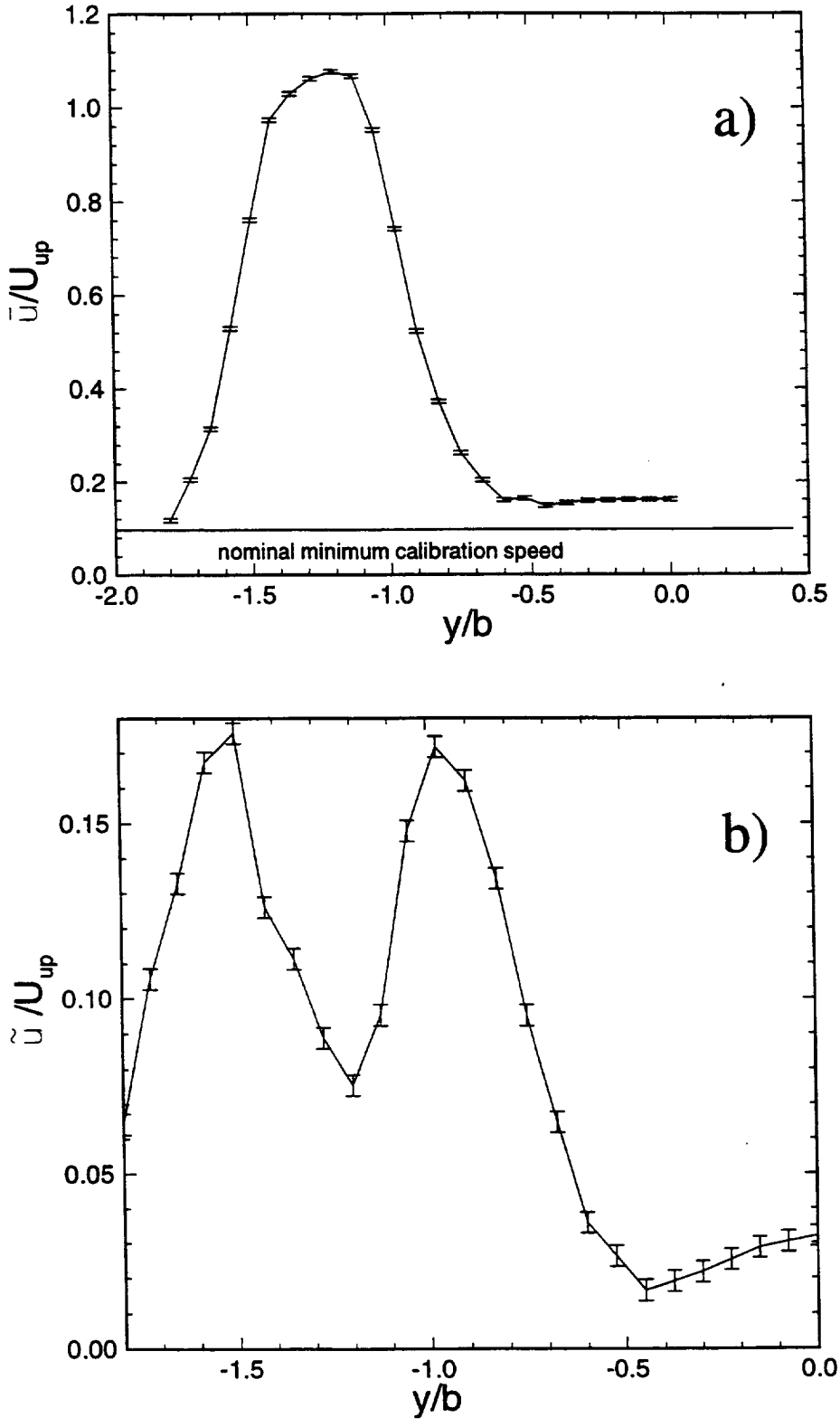

Figure 4.2: Error bar estimates for velocity measurements, a) average, b) rms.

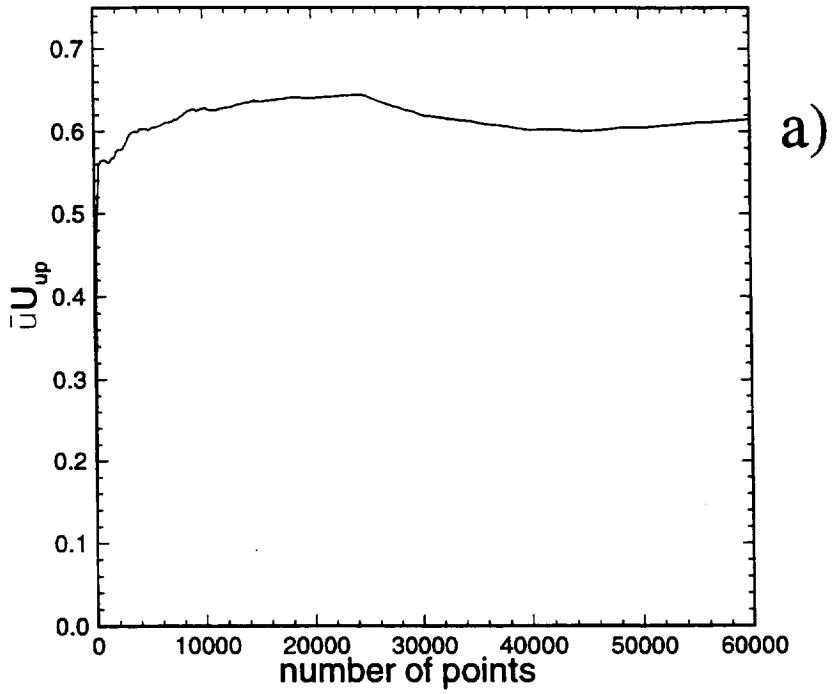

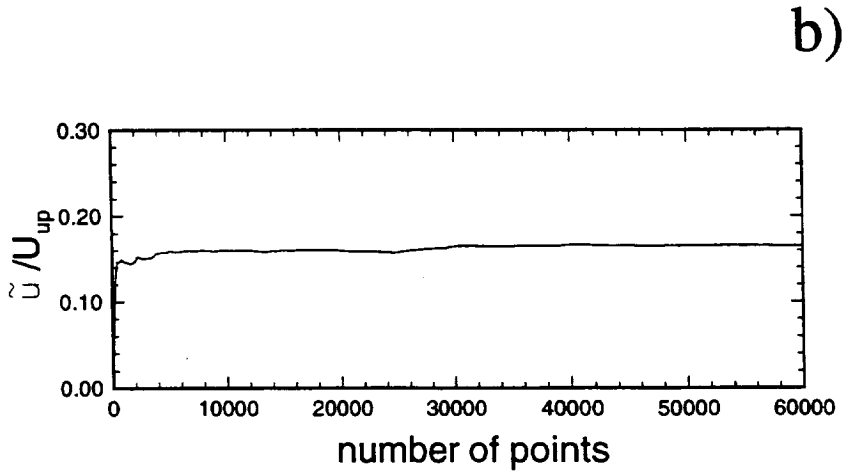

Figure 4.3: Statistical convergence for $\bar{u}/ U_{up} \approx 0.6$ in the plume region, a) average, b) rms.

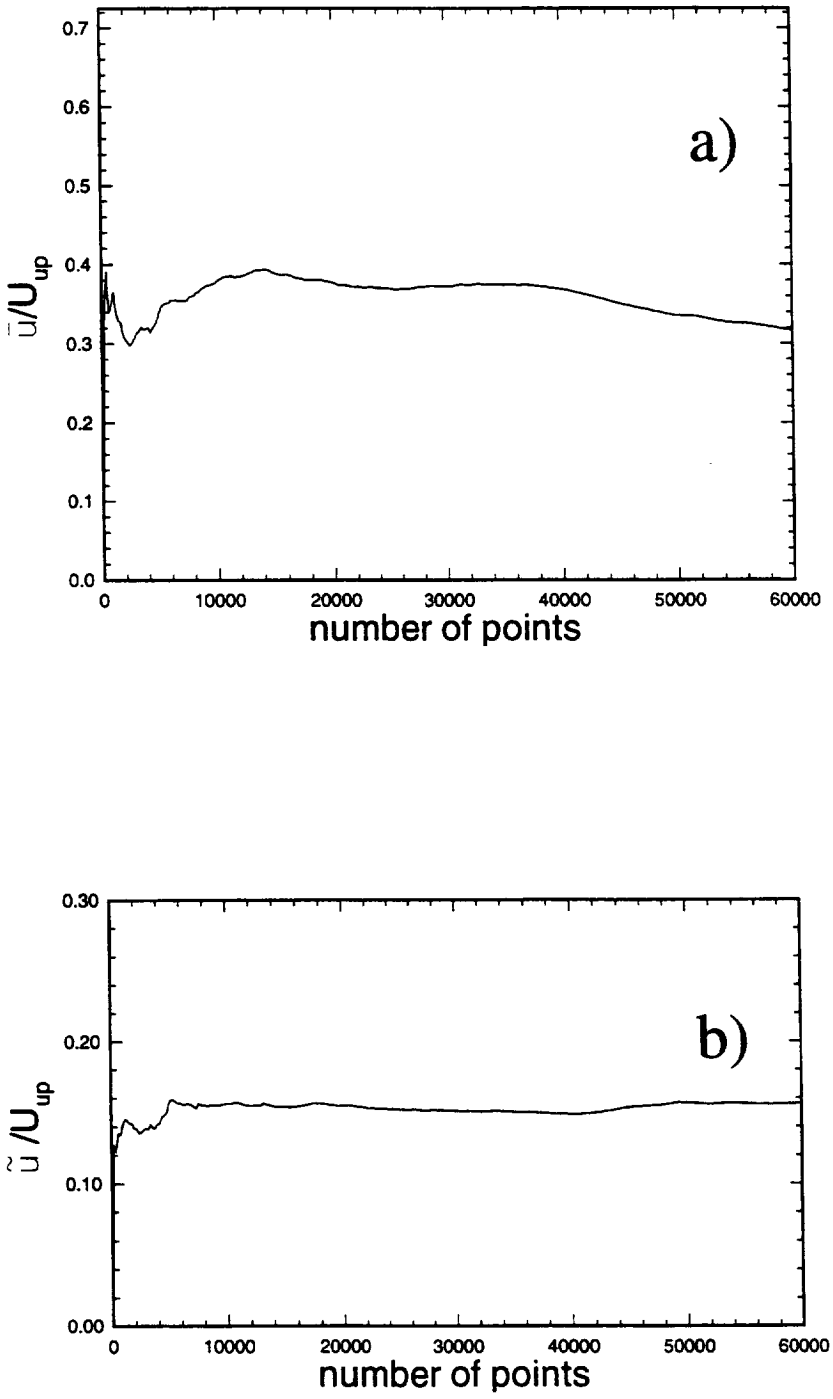

Figure 4.4: Statistical collapse for $\bar{u}/ U_{up} \approx 0.3$ in the plume region, a) average, b) rms.

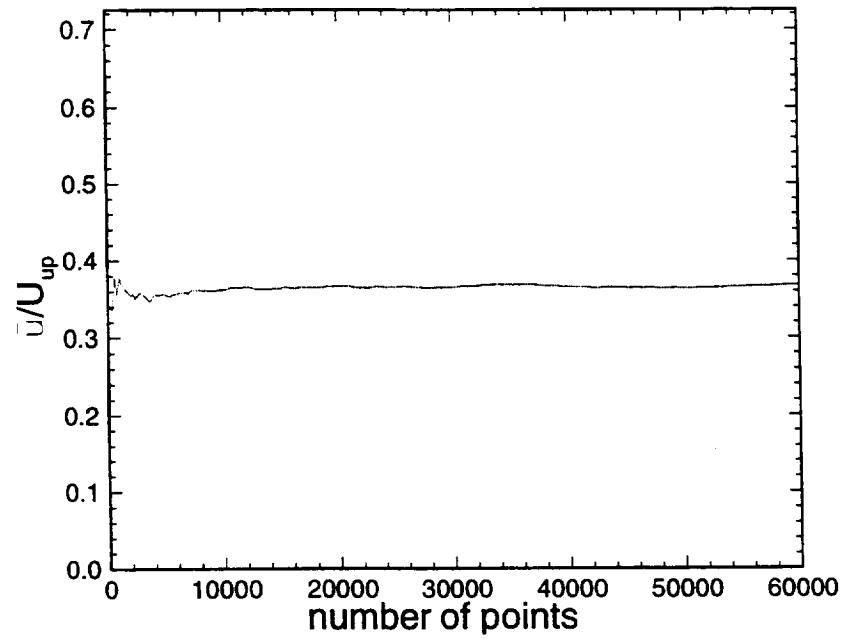

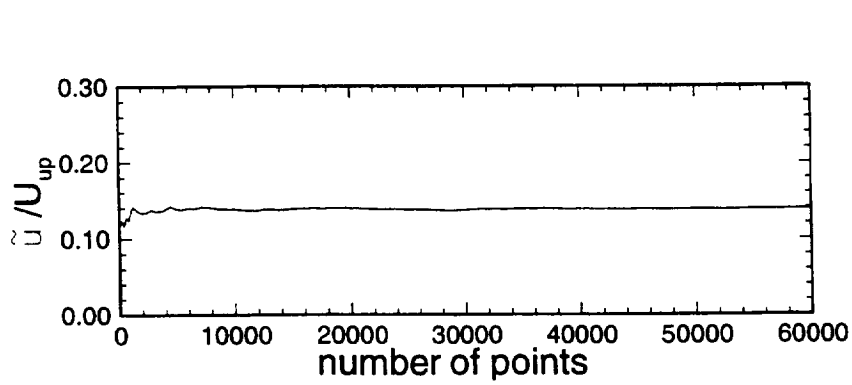

Figure 4.5: Statistical collapse for $\bar{u}/ U_{up} \approx 0.3$ in the side wall shearlayer, a) average, b) rms.

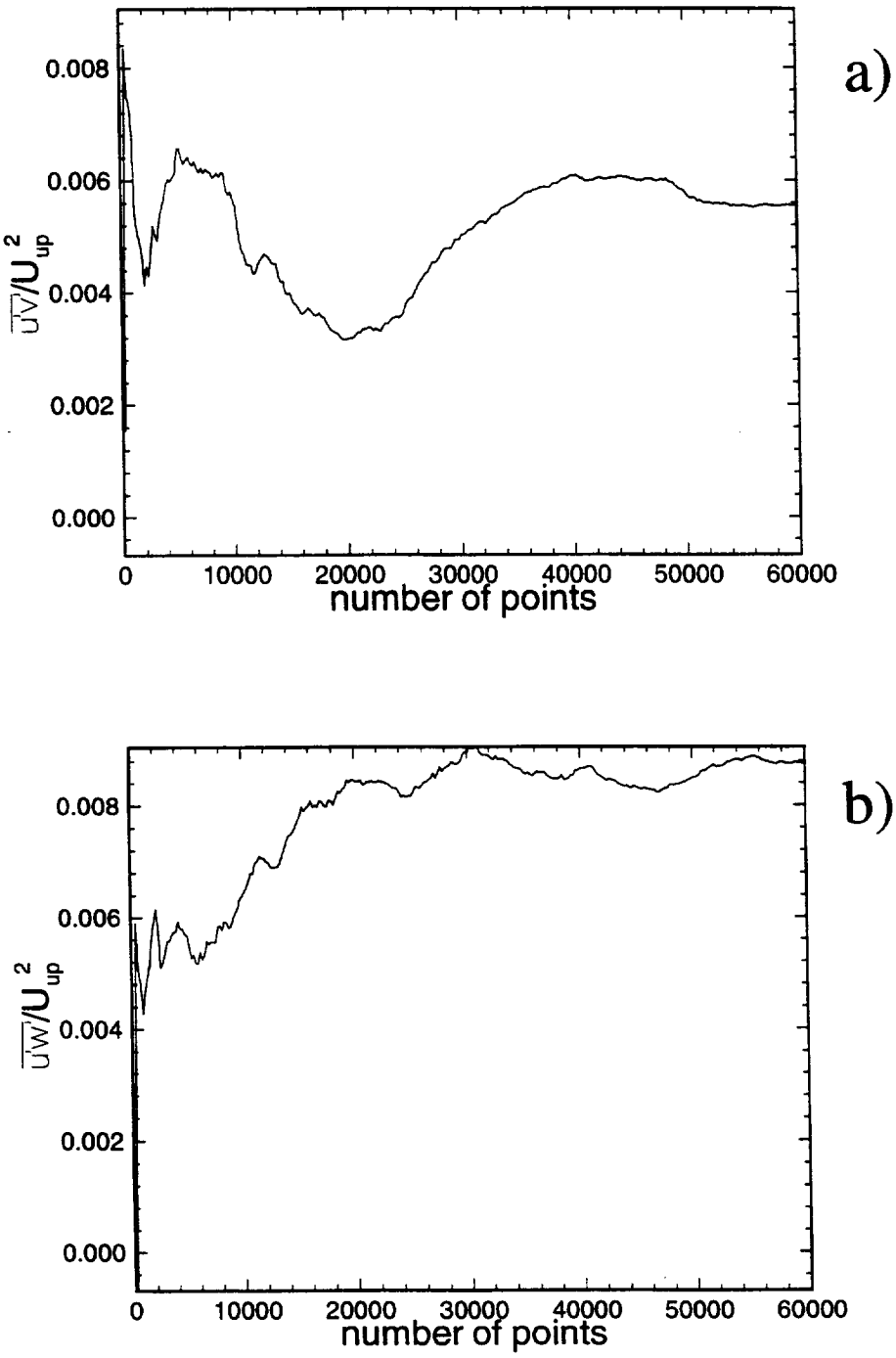

Figure 4.6: Shear stress calculation convergence, a) $\overline{u' v'}/ U_{up}$, b) $\overline{u' w'}/ U_{up}$.

5. RESULTS AND DISCUSSION

5.1 Introduction

The results of this study are divided into two parts. The first part, section 5.2, details the untabbed jet results. These data were used to provide a reference case for the tabbed jet results. The results for the tabbed jets are presented and discussed in sections 5.3-5.6. The initial results (static pressure, streamwise velocity and surface streak patterns) for the primary tab geometry are first presented (section 5.3). These data provided the details which served as a basis for the modification of the tabbed jet. This section is followed by a discussion on the orientation of the secondary tabs for the modified tab geometry (section 5.4). The initial results for the modified geometry are then presented (section 5.5). Finally the remaining results for tabbed jet geometries are compared and discussed (section 5.6).

5.2 Untabbed Jet Results

5.2.1 Exit Boundary Layer Survey

A velocity survey using a single sensor hot-wire probe was conducted at the exit of the tunnel extension to provide detailed information about the approach boundary layer for the untabbed jet. The results, shown in Figure 5.1, indicated that the approach boundary layer had: a boundary layer thickness, δ, of 3mm (0.015b), a displacement thickness, δ_d, of 1.27mm (0.0064b) and a momentum thickness, θ, of 0.52mm (0.0026b). The approach boundary layer remained laminar up to the exit as indicated by the shape factor H, which was found to be 2.47. (H for the Blasius solution is 2.59.) The peak

fluctuating velocity value was $\tilde{u}_{max} = 0.014U_{up}$ at $y/\theta = 3$. The fluctuating values were seen to decrease to nominally $0.006U_{up}$ as the observation point approached the core flow. This turbulence level indicated that the tunnel flow conditioners were able to quiet any disturbances created by removing the test section and opening the tunnel to the laboratory flow. Note also the fluctuating velocity profile shown in Figure 5.1 was consistent with that made rational by Foss (1977) for a laminar boundary layer. That is, the peak in the fluctuation intensity and the shape of the $\tilde{u}/U_{up}$ distribution could be explained by a modulation in the height of the boundary layer and a proportionate variation ($\delta y/y$=constant) for y values less than δ. There was a local maximum in the velocity profile ($\bar{u} = 1.02\ U_{up}$) at $y/\theta \approx 7$. This maximum in the velocity profile was an artifact of the contraction in the tunnel upstream of the measurement location. The velocity profile appeared to be relaxing to $\bar{u} = U_{up}$ for y/θ greater than 10.

5.2.2 Upstream Pressure Distribution

The upstream static pressure survey, Figure 5.2, showed that the untabbed tunnel had a static pressure upstream of the tunnel exit nominally equal to the atmospheric value. Note that all pressure distributions within are gage pressures with the atmospheric pressure as the reference. This result was expected given the small percentage (0.1%) change in area of the tunnel calculated from the momentum thickness. The peak values of these data were $P^* = \pm 0.02$. Note that these results indicated that the pressure taps were functioning properly.

5.2.3 Velocity Magnitude Profiles

Figures 5.3a-5.5a show the average streamwise velocity field downstream of the tunnel exit for the untabbed jet. The results from these data indicated the development of the untabbed jet to be as expected. Specifically, the shear layer, as described by the isotach lines, remained strongly aligned with the tunnel top and side walls as the downstream distance was increased. The shear layer grew into both the core and ambient regions with slightly more penetration of the shear layer into the ambient region. This was expected given the higher momentum of the core flow and the entrainment of ambient fluid.

Turbulence intensity values are presented in Figures 5.3b-5.5b. The maximum turbulence intensity for the three measurement planes was located at x/b=0.7 (nominally $\tilde{u}_{max} \approx 0.18U_{up}$). This value was located near the center of the shear layer. The values indicated that the velocity field was highly turbulent in the sheared region of the free jet. Note that these maxima are characteristic of single stream shear layers (Wygnanski and Fiedler (1970) and Bruns et. al. (1991)).

5.3 Primary Tab Jet: Preliminary Results

5.3.1 Upstream Pressure Distribution

Figure 5.6 shows the upstream static pressure distribution for the primary tab geometry. A static pressure distribution, P(x,y), was indicated upstream of the tab. This pressure distribution was created as a result of placing the primary tab into the core flow and changing the streamline patterns upstream of the tab. The observed peak static pressure was found to be $P^*=0.7$ at x/b=-0.05 and y/b=0. (Larger pressures could exist

closer to the tab/nozzle wall junction as suggested by Figure 5.6.) A significant drop in static pressure occurred along the centerline of the tunnel from x/b=-0.05 to x/b=-1. That is, the static pressure decreased from P^*=0.7 to P^*≈0.2 for these values. From x/b=-1 to x/b=-1.95 (the farthest upstream measurement location) the static pressure decreased from 0.2 to 0.15. A pressure distribution, in the y-direction, was also indicated by Figure 5.6. These pressure values ranged from a maximum value of 0.7 at x/b=-0.05 and y/b=0, to nominally atmospheric at x/b=-0.05 and y/b=-1.4. Note that this static pressure distribution was qualitatively similar to that reported by Zaman et. al. (1994) for a round tabbed jet.

5.3.2 Surface Streak Observations

Surface streaking experiments were performed upstream of the tab face to further clarify the flow characteristics. The streaks were acquired by taping mylar sheets to the tunnel surfaces upstream of the exit and to the tab faces. The tab faces were then cut out of the mylar sheet such that the mylar sheet covered only existing surfaces. A red pigment (Day-Glo Red AX-13) was mixed with kerosene and was painted onto the mylar sheet. The tunnel was then turned on with an approach velocity of nominally 10.5 m/s and the streaking was allowed to progress until the mixture dried. The pigment was affixed to the mylar sheet with a clear spray fixative. The streak patterns were photo-reduced and scanned into electronic format.

Figure 5.7 shows the surface streaking results for the primary tab geometry. Note that the tab orientation was the same for these data as for the other data presented in this report (Figure 2.4) although the results for the tunnel and tab surfaces are presented as

though they existed on the same x-y plane. These traces show the complex surface pattern created by the primary tab geometry. Four singular points can be identified along the centerline of the flow field. Specifically (from left to right) a saddle, node, saddle, node pattern was observed as shown in Figure 5.8. Two topological arguments were made to show that this pattern was allowable. Viewing the geometry from the top, a sphere with two holes was drawn as shown in Figure 5.9. The sphere, in this case, was flattened such that its upper and lower surfaces contain the vector field defined by the wall shear stress distribution. The holes are selected such that the velocity is perpendicular tot he exposed edges. The lateral edges of the flattened sphere are referred to as seams. The subject vector field is everywhere tangent to a seam. Note that a sphere with two holes has an Euler characteristic, $\chi_{surface}$, of zero. This value, $\chi_{surface}$, was found by identifying the Euler characteristic for the present surface as that for a sphere (+2) with the with the addition of two holes (-1 each). Hence, for the present case, $\chi_{surface}=0$. The sum of the indices of the singular points on the subject surface is equal to the Euler characteristic for that surface by:

$$\sum N - \sum S = \chi_{surface} \tag{5.1}$$

where N and S are the number of nodes and saddles respectively. There had to be an equal number of nodes and saddles in this case for the nodal pattern to be allowed; thus the pattern shown in Figure 5.9 was allowed, but not unique.

This limitation (i.e. the lack of a unique solution) of a topological analysis is made clear if the node on the primary tab face (N2) is examined. In Figures 5.7 this node appeared to be a line of singular points. An alternate topological argument could be made

if one considered the node (N2) to be part of the following pattern: node, saddle, node, saddle, node as shown in Figure 5.10. This configuration of singular points had one net node and therefore had the same implications topologically as the one node (N2) used in the previous analysis. Any combination of nodes and saddles which had one net node to replace N2 was therefore an allowable pattern. Figure 5.8 shows the simplest topological argument that was permitted.

A second topological inference was made by viewing the flow in the x-z plane as shown in Figure 5.11. In this view there was also a flattened sphere with two holes($\chi_{surface}$=0). Note that, the sphere, in this case, was flattened. Equation (5.1) is modified to accommodate the flattened sphere by:

$$2\sum N + \sum N' - 2\sum S - \sum S' = \chi_{surface} \qquad (5.2)$$

where N' and S' are nodes and saddles that lie on the seam of the flattened sphere (note these singular points are dubbed "half nodes" and "half saddles"). The indicated surface singular points were four "half saddles" in this case. These singular points gave -4 which was not equal to $\chi_{surface}$. Note that two half saddles, S2' and S4', were shown in Figure 5.9 as nodes N1 and N2. This change in from node to saddle was due to the change in orientation of the analysis. The sum of the singular points on the surface points indicated that more singular points in the flow field were required. These were inferred to be located above the surface as shown in Figure 5.11. The inferred pattern was the least complicated pattern that satisfied the topological constraints of the system. It is important to realize that the distances of the four full singular points, from the bounding surface, is exaggerated in Figure 5.11. (Note also that the following inferences are made rational by

the streamwise vorticity data presented in sections 5.6.6 and 5.6.7.) The value of $\chi_{surface}$ was zero with these full nodes and saddles added in. The most upstream node (N1) represented the approach boundary layer vorticity which separates from the surface. This vorticity is related to the organized motion that has been referred to as the "necklace vortex" by various authors; see, e.g., Zaman et.al. (1991). The second half saddle point (S2') was an attachment point for the flow (N1 in Figure 5.9). It was inferred that the second node (N2) was characterized by vorticity with the opposite sign as compared with the approach boundary layer. In particular, the sign of the vorticity in N2 is compatible with the dominant streamwise vorticity downstream of the exit. As shown below, this inferred sign of the vorticity in N2 is required to account for the "solenoidal condition" ($\nabla \cdot \vec{\omega} = 0$) of this dominant motion. (These dominant motions correspond to the vorticity created by the upstream pressure distribution.) The final full node (N3) denotes vorticity with the same sign as the approach boundary layer and corresponds to the second attachment point. Note that the full saddle (S5) was required to create a smooth vector field in the indicated plane and to bring the sum of the singular points to zero.

The streak lines presented in Figure 5.8 were used to describe the s- and b- directions at the wall used in (1.6) to determine the flux of vorticity into the flow from the pressure gradient. Recall that the s-direction was parallel to the direction of the flow, and was therefore described by the direction of the streaks. The b-direction was perpendicular to the streaks such that $\hat{s} \times \hat{n} = \hat{b}$. In Figure 5.8 the s-direction would be the x-direction and the b-direction would be the y-direction well upstream of the tab. This implied a flux of

ω_y into the flow because of the tab induced pressure gradient ($\partial P / \partial x$ greater than 0 for $y \approx 0$). As the separating streamline was approached along the centerline (i.e. for y=0) the s-direction shifted to become aligned with the y-direction. The s-direction was strongly aligned with the y-direction in the separated region directly upstream of the tab indicating a flux ω_x from the pressure gradient into the flow.

Note that it was not possible to determine, from the streak patterns alone, what happened to the vorticity once it was introduced into the flow. The streak results indicated some of the boundary conditions for the flow field. The streamwise vorticity results (presented in sections 5.6.6 and 5.6.7) also represent part of the solution of the flow field. Flow mechanics may be inferred by using these data in combination. These inferences will be made once the streamwise vorticity data are presented.

5.3.3 Streamwise Velocity Distributions

Figures 5.12a-5.14a show the average streamwise velocity magnitudes plotted for the primary tab geometry. These data show the effect that the passive mixing tabs had on the average streamwise velocity field; namely,the shear layer became aligned with the side of the tab and the tunnel side wall. Near the top of the tunnel a "plume" of fluid, ejected from the core region into the ambient region, was shown. A significant region of high speed fluid was found above the projected tunnel exit in the plume region unlike the distributions for the untabbed geometry. This area of high speed fluid appeared to be increasing in size for the downstream locations investigated. A large region of low speed flow was seen directly aft of the tab. This low speed region also grew in size as the downstream distance was increased. In addition, these data also suggested that the flow

was displaced laterally as the downstream distance was increased. This was shown by the increased distance of the isotach lines from the tab and tunnel side wall. These observations illustrated the strong tendency of the tabbed jet core fluid to expand rapidly into the ambient region.

The turbulence intensity values, Figures 5.12b-5.14b, also revealed an important aspect of this flow. The maximum turbulence intensity was found to be nominally $\tilde{u}=0.18U_{up}$. This value was found in the region of the shear layer where the jet fluid was penetrating into the ambient region, i.e. in the plume. It is instructive to note that the peak turbulence intensity showed no increase when compared to that for the untabbed geometry. This suggested that the large scale exchange of fluid was not associated with an increase in the turbulence levels, but rather it was a result of the streamwise vorticity that was present at the jet exit plane created by the upstream "pressure hill". Note however that the use of a tab has also been shown to increase the small scale mixing and dissipation in the shear layer (Foss and Zaman, (1996)) which suggests that the passive mixing tabs could be used to enhance both large scale and small scaling mixing.

5.4 Addition of the Secondary Tabs

5.4.1 Motivation for Modification of the Primary Tab Geometry

One of the goals of the present study was to determine methods for increasing the large scale exchange of fluid between the core and ambient regions using the tabbed jet concepts. The modified tab geometry was conceived using the results from Section 5.3. It was noted while performing the experiments on the primary tab geometry that the flow had a naturally "upward" (+z direction) trajectory along side of the primary tab, i.e. for

y/b<-0.5. Using a woolen tuft this trajectory was estimated to be nominally 10 degrees at the tunnel exit. It was surmised that the expansion of the core fluid into the ambient region could be increased if attachment surfaces were provided. It was found that when the secondary tabs were added, the flow could achieve an upward trajectory of nominally 45 degrees before separation from the secondary tabs was detected.

5.4.1 Determination of the Secondary Tab Orientation

The final orientation for the secondary tabs was determined by varying the angle of the secondary tabs and measuring the static pressure just upstream of the exit for each of these angles. Figure 5.15 shows the results of this survey. This survey was conducted by setting the angular position of the secondary tabs and surveying the static pressure for y-locations from y/b=-0.5 to -1.2 for x/b=-0.05 (the taps closest to the exit plane of the jet). The angular position of the secondary tabs was varied from 0 degrees, i.e. horizontal, to 50 degrees up from horizontal. These data indicated that there were two distinct angular positions of the secondary tabs that created locally minimum pressure regions in the upstream pressure field. From σ=10 to σ=15 degrees a small region of negative pressure was found upstream of the secondary tab. The second region was from σ=20 degrees to σ=50 degrees. The selected position of σ=40 degrees for the secondary tabs was chosen because it contained the largest negative static pressure region in the survey. Note that as of the time of this report no additional data have been acquired for other angular positions of the secondary tabs. All further data presented within this report were for σ=40 degrees.

5.5 Modified Tab Geometry: Preliminary Results

5.5.1 Upstream Pressure Distribution

The results of the upstream static pressure distribution are shown in Figure 5.16. These data show that the upstream static pressure distribution for the modified geometry was qualitatively similar to the primary tab geometry shown in Figure 5.6. However, there were two significant differences in the pressure fields. First, the observed peak value of the pressure coefficient increased from 0.70 for the primary tab geometry to 0.72 for the modified tab geometry. Second, a region of subatmospheric pressure was measured at the exit of the tunnel, i.e. for x/b=-0.05 and y/b from -1.1 to -0.8.

5.3.2 Surface Streaking Observations

The results of the surface streaking for the modified tab geometry are presented in Figure 5.17. These observations showed the same trends upstream of the primary tab as were discussed in section 5.3.3.

An interesting pattern was seen on the surfaces of the secondary tabs. The streak patterns in these regions showed a bifurcation line (i.e. a line along which two distinct flow patterns are merged) which followed along the face of the secondary tab. The flow separated from the outer portion of the secondary tab as indicated in Figure 5.17 while remaining attached to the inner portion. This indicated that only a portion of the secondary tab may be needed for the same effect to be achieved. This was significant in that it may be possible to optimize the shape of the secondary tabs to reduce the projected area of the secondary tabs in the ambient flow. Note, in a typical gas turbine engine this

outer region is composed of cool co-flowing fluid. It will be desirable to minimize the projections of tabs into this flow in order to maximize the fan flow.

The direction re-oriented boundary layer vorticity was tracked upstream of the tunnel exit using a wool tuft. Its trajectory was very similar to the streak pattern of Figure 5.17. Specifically, the re-oriented boundary layer followed a path similar to the bifurcation line on the tunnel wall and proceeded along this side of the secondary tab nominally with the same path as the bifurcation line shown in Figure 5.17. The re-oriented boundary layer vorticity separated from the tab face at nominally half way up the outer edge. The orientation of this vorticity upon leaving the surface was such that there were significant non-streamwise components of vorticity (ω_y and ω_z). This was shown by the direction of the tuft which was not directly in the streamwise direction at the point of separation. This was rational since the inferred velocity gradient in the re-orientation term $\omega_y \partial u / \partial y$ from (1.7) was small in this region. This was in direct contrast to the inner edge of the secondary tab, y/b=-0.5, and at the tunnel surface where the vorticity induced by the pressure hill was strongly streamwise due to the large inferred $\partial u / \partial y$ in that region. Note that in a jet flow with both a core flow and a co-flow this velocity gradient should be larger which will re-orient the boundary layer vorticity more into the x-direction. This in turn should increase the effectiveness of the modified tab geometry even further.

5.5.3 Streamwise Velocity Distributions

The results for the streamwise velocity surveys for the modified tab geometry are shown in Figures 5.18-5.20. The average velocity and turbulence intensity results

showed similar trends as were seen in Figures 5.12-5.14 for the primary tab geometry. A comparison of the results for all three geometries will be made in section 5.6.3.

5.6 Comparison of Jet Geometries

5.6.1 Discussion of the Static Pressure Fields

Tuft observations showed that the flow had approximately 10 degree upward (+z) trajectory in the plume region at the exit plane of the jet for the primary tab geometry. This upward trajectory was increased to approximately 45 degrees for the modified tab geometry. These observations can be used to describe the differences in the static pressure fields of the two tabbed geometries.

Figures 5.21 and 5.22 are schematic representations of the streamlines at some y location near a secondary tab ($y/b \approx -1$). The flow had a slight upward trajectory with only the primary tab, as shown in Figure 5.21. The associated streamline curvature created a pressure gradient perpendicular to the streamlines. Given the Euler-n equation evaluated for a steady flow:

$$\frac{\partial P}{\partial n} = \rho \frac{V^2}{R} \tag{5.3}$$

the pressure will increase on a curve drawn in the outward normal direction and perpendicular to the streamlines. Equation (5.3) indicated that the pressure at locations along the exit of the tunnel, where there was an upward trajectory of fluid present, must have been subatmospheric. Note that in the case of the primary tab geometry this effect did not extend into the tunnel far enough to be detected by the pressure taps closest to the exit (i.e. for x/b=-0.05). In contrast, the streamlines for the modified tab geometry were

characterized by a smaller radius of curvature because the flow remained attached to the secondary tabs. This is shown schematically in Figure 5.22. The change in the streamline curvature resulted in the modified upstream static pressure field shown in Figure 5.16. Specifically, because the curvature of the streamlines was more compact (i.e. smaller R) for the modified tab jet, the magnitude of the pressure gradient normal to the streamlines increased and the subatmospheric region increased in size and magnitude.

Figure 5.23a shows the pressure distribution as a function of y for x=-0.05b (the most downstream pressure tap). These data support the above analysis of the flow field using the inferred streamlines. Specifically, the region of negative pressure was clearly shown for the modified tab geometry. Note that a negative streamwise pressure gradient is favorable to the boundary layer. The modified tab geometry also showed an increased peak pressure at x=-0.05b and y=0 when compared to the primary tab geometry. Equation (1.6) indicated that a pressure gradient in the y-direction will flux ω_x into the flow field. This quantity was calculated and plotted in Figure 5.23b. These data show that the peak in the pressure gradient ($\partial P^* / \partial(y/b)$) occurred at y=-0.5b (the edge of the primary tab) and that there was a slightly higher peak in the positive gradient for the modified tab geometry.

An interesting feature of Figure 5.23b was the local minimum value for the modified tab geometry at y=-0.9b. The pressure gradient changes sign for the modified tab geometry from y=-0.8b to y=-1.2b. This indicated that a flux of $+\omega_x$,which served to reinforce the reoriented boundary layer vorticity, was introduced into the flow in that

region. This change in the pressure distribution represented a significant change in the flow fields for the two tabbed geometries.

A plot of $P^*(x,y=0)$ is presented in Figure 5.24a. These data again show the slightly higher peak P^* value for the modified tab geometry at x=-0.05b and y=0. Note that the pressure distributions become nearly identical for x<-0.85b. Equation (1.5) indicated that a pressure gradient in the x-direction (shown in Figure 5.24b) will flux ω_y into the flow field. These data indicated that a slightly higher flux of ω_y will occur for the modified tab geometry. It was instructive to note in Figure 5.23a the slight back pressure shown for the untabbed jet which indicated that the flow continued to accelerate slightly in the tunnel extension.

5.6.2 Comparison of the Streamwise Velocity Fields

Several parameters were created in order better quantify the changes in the distortion of the average streamwise velocity field for the three geometries. These parameters, evaluated from the average streamwise velocity fields, were developed to aid in the interpretation of the available data. Figure 5.25 shows the definition of the three penetration measures overlaid on the modified tab geometry streamwise velocity data at x/b=2.0.

The maximum penetration of the shear layer into the core region, as defined by the minimum z-location along the 0.95 contour line at y=0, was described by δ_{core}. Figure 5.26 shows this measure plotted versus the downstream distance. It was clear that the tab created a large low speed region downstream of the primary tab. It was also clear that this wake region did not display typical characteristics. Specifically, the velocity deficit (U_{up} -

$\overline{u}$) remained constant rather than decreasing and the area of high velocity deficit (i.e. low $\overline{u}$) increased in size. These data implied that the penetration of the wake into the core region continued well past x/b=2.0 for the tabbed jets. This observation was supported by the results of Zaman et. al. (1992) which showed that the jet bifurcated into two distinct regions of core fluid at a downstream distance of x/D=4.0 for a round jet with two primary tabs. (D was used to designate the diameter of the round jet.) The degree of penetration, as revealed by this measure, did not appear to be significantly different between the primary tab and modified tab geometries.

A second measure of the distortion in the flow field was described by $\delta_{ambient}$. This measure, shown in Figure 5.27, was defined by the maximum z-location that the shear layer penetrated into the ambient region along the $0.15U_{up}$ contour line; see Figure 5.25. This measure clearly detailed both the distortion in the flow field by the primary tab alone and the enhanced distortion created by the addition of the secondary tabs. The primary tab geometry showed a nominally 250% increase in the depth of penetration of the shear layer into the ambient region over that observed for the untabbed geometry. The addition of the secondary tabs increased the penetration to nominally 400% over the untabbed geometry.

Finally, in a typical jet flow the shear layer grows into both the core region and the ambient region. The average streamwise velocity results for both tabbed geometries showed that there was a significant region of high speed fluid above the projected exit plane of the jet. Figure 5.28 shows $\delta_{high\ speed}$ versus the downstream distance. $\delta_{high\ speed}$ was defined by the maximum z-location of the 0.95 contour line; see Figure 5.25. These data showed that early in the tabbed jet development, the high speed fluid (i.e. fluid with

$\bar{u}$ greater than $0.95U_{up}$) extended well into the ambient region. It was expected that this penetration of the high speed fluid from the core flow would decrease as the jet continued to develop downstream. Specifically, as the jet becomes fully developed the region described by the $0.95U_{up}$ contour will decrease in size; hence $\delta_{high\ speed}$ will first decrease to zero, then become negative. Note that the untabbed geometry showed a negative penetration of high speed fluid indicating that the high speed fluid was , as expected, contained within the core region.

An alternate measure of the growth in the shear layer was represented by the shear layer momentum thickness, θ, defined by

$$\theta = \int u^* (1-u^*)\, dn \tag{5.4}$$

where

$$u^* = (u-u_{min})/(u_{max}-u_{min}) \tag{5.5}$$

and n is the direction of the velocity survey in the y-z plane. This direction was different for the three surveys performed. See Figure 5.29. Note that in (5.8) u_{min} was the minimum velocity (nominally $0.1U_{up}$) measured in each traverse. Equation (5.8), typical of a two stream mixing layer, was adopted to normalize the velocity traverses for this section of the results because of the difficulty in accurately measuring flow speeds below the minimum calibration speed (section 4.2). Three regions of the shear layer were investigated to provide a measure of the shear layer characteristics. Note that (5.7) was first evaluated using data from the velocity surveys already presented. These data were found to have too few data points in the shear layer for an accurate calculation of the momentum thickness. Therefore, additional single sensor hot wire data were taken to

allow better calculation of θ. Figure 5.29 shows the locations where the shear layer thickness was evaluated for the primary tab geometry at x/b=2.0.

The plume, where the penetration of the shear layer into the ambient region was a maximum, was the first region investigated. The shear layer thickness was found to have a maximum value in this region. The location of this survey was determined by viewing the average velocity profiles and determining the y location where $\delta_{\text{high speed}}$ was a maximum. At this location the shear layer thickness was a maximum and a line drawn perpendicular to the isotachs was oriented nominally in the z-direction. If a traverse were conducted at another location then the shear layer momentum thickness would have been artificially inflated. This can be clearly seen for the traverse indicated by the dashed line in Figure 5.29. Two checks of the results were made to guard against this potential. First, if a velocity survey were not perpendicular to the shear layer there would be a region in the traverse data where the velocity profile was distorted. For example, in the limiting case where a velocity survey was parallel to an isotach the velocity would be constant and the velocity profile would not have been as expected for a shear layer. All surveys were plotted and visually checked to avoid this condition. The second check was a self consistency check. A zero pressure gradient shear layer will have a growth rate that becomes constant in the self preserving region. The data were checked against this trend. Results which did not fit this trend were retaken.

The second interrogated region was the shear layer that was aligned with the side of the tab. In this survey, a traverse was performed perpendicular to the edge of the tab and at the midpoint of the edge of the tab. The third survey was conducted in the z-direction

off the tip of the tab. Both of these surveys were also checked through the plotting of the surveys and by checking for linear growth.

The shear layer momentum thickness in the plume was plotted versus the downstream distance for all three geometries in Figure 5.30. Data for the untabbed jet were taken at the top center line of the tunnel. The data for the untabbed jet showed the expected characteristics. Specifically, the shear layer growth quickly became linear. Although it was not shown here, the first three measurement locations in the downstream survey displayed laminar/transition shear layer characteristics. The growth rate, $d\theta/dx$, found by fitting the points in the survey from x=0.4b to x=2.0b, had a value of 0.035. This was consistent with experimental values from other single stream shear layers (see Leipmann and Laufer (1947) and Bruns et. al. (1991)).

The results from the plume region illustrated the increased distortion of the modified tab geometry. The momentum thickness for the primary tab geometry was slightly larger than that for the untabbed jet due to the distortion in the shear layer in this region. However, the primary tab geometry had the same growth rate ($d\theta/dx$=0.035) as was found for the untabbed jet. The modified tab geometry results indicated that the momentum thickness was nominally twice those for both the untabbed jet and the primary tab geometry. In addition the growth rate had increased from 0.035 to 0.050. These data implied that the modified tab geometry deformed the shear layer in the plume region.

The side and bottom momentum thickness surveys, Figure 5.31, showed that the primary tab and modified tab geometries had similar effects on the flow field. The bottom momentum thickness, θ_{bottom}, was the smallest of all of regions investigated. This

was not surprising since this shear layer originated at the location where the tip of the tab ended in the flow field, at a downstream distance of x/b=0.61. The growth rate, 0.024, was much smaller than the untabbed jet's growth, 0.035. This result was supported by the observation that the shear layer in this area grew almost exclusively into the high speed, high momentum region. The high momentum of the core flow retarded the growth rate of the shear layer in this region. Along the side of the tab the momentum thickness, θ_{perp}, and the associated growth rate, 0.027, were between those reported for θ_{bottom} and θ_{plume}. These data indicated that the shear layer thickness and growth rate increased as the top of the tunnel was approached from the core region.

It was also made clear from these data that the effect of the secondary tabs was localized to the top portion of the flow field. Specifically, both the penetration measures and the momentum thickness measures below the tunnel top (for z<0) showed identical values for both geometries. These same measures above the tunnel were substantially increased for the modified geometry.

Figures 5.18a-5.20a, when viewed in sequence, showed the flow field for the modified tab geometry to have experienced a large scale rotation in the plume. For these data at x/b=0.7 a line drawn perpendicular to the plume contour lines pointed in the -y and + z direction. At x/b=1.2 this same line appeared to be directed in the +z direction. And finally at x/b=2.0 the line pointed in the +y and +z direction. Note that the apparent center of the rotation was displacing laterally (i.e. in the -y direction) with the shear layer as the downstream distance was increased. This apparent large scale rotation in the plume was less evident in the primary tab geometry data but it was apparent given close

inspection. It should be noted that the turbulence intensity plots, Figure 5.18b- 5.20b, also showed this same large scale rotation in the flow field.

A significant difference between the average streamwise velocity data presented for the primary and modified tab geometries was most clearly seen at x/b=2.0. In Figure 5.20a there was a large region of fluid with a significant streamwise velocity in the wake region of the tab. During the data acquisition at x/b=2.0, and to a lesser extent at x/b=1.2, for the modified geometry it was noted noted that in the low speed region of the flow field downstream of the tab the flow was highly intermittent. Oscilloscope traces revealed that highly turbulent/active fluid periodically passed by the probe. These times of "active" fluid passage were separated by what appeared to be times of nominally quiescent low velocity fluid.

A comparison of the peak value of the turbulence intensity for the three geometries revealed a slight increase for the modified tab geometry. The peak values were found to be $0.18U_{up}$ for the untabbed and primary tab geometries and $0.21U_{up}$ for the modified tab geometry. These results further support the conclusion that the characteristics as well as the shape of the shear layer were changed for the modified tab geometry.

5.6.3 In-Plane Velocity Results and Comparison

The in-plane velocity results at x/b=1.2 and 2.0 indicated the source of the strong outflow of the core fluid into the ambient region. Figures 5.32 and 5.33 show the average lateral, $\overline{v}$, velocity contours for the primary tab and modified tab geometries respectively. These data show a significant lateral velocity ($\overline{v} \approx -0.2U_{up}$) away from the tab in the core region. Note that the modified tab geometry showed a distinctly larger lateral velocity

($\overline{v}_{max} = -0.24U_{up}$) when compared to that of the primary tab geometry ($\overline{v}_{max} = -0.21U_{up}$) indicating an increased expansion rate for the flow field. Additionally, there was a significant lateral velocity above the projected top surface of the tunnel for both geometries, although this region extended farther into the ambient region for the modified tab geometry.

At x/b=2.0 the $\overline{v}$ velocities decreased in magnitude for both geometries. The primary tab geometry, Figure 5.32b, showed a small decrease in magnitude of the maximum in lateral velocity along side of the tab (from $\overline{v}_{max} = -0.21U_{up}$ at x/b=1.2 to $\overline{v}_{max} = -0.20U_{up}$ at x/b=2.0). There continued to be a significant lateral velocity above the top of the tunnel. The results for the modified tab geometry, Figure 5.33b, showed a more significant decrease in magnitude of $\overline{v}$ (from nominally $-0.24U_{up}$ to $-0.18U_{up}$), however the lateral velocity in the plume region continued to be significant showing very little decrease in magnitude.

The $\overline{w}$ profiles, shown in figures 5.34 and 5.35, confirmed the upward (+z-direction) flow trajectory for $y \approx -b$ and $z \approx 0$ as well as the downward (-z-direction) trajectory for $y \approx 0$ and $z < -0.8b$. The velocity in the second region resulted from the re-direction of the upstream core fluid by the physical surface of the tab. The re-direction of the core flow has been shown to bifurcate a jet into two distinct regions of high speed fluid for a round jet with two opposing tabs (Zaman et. al.(1992)).

These data for the modified tab geometry data at x/b=1.2, shown in Figure 5.34a, showed that the up-wash, i.e. expansion into the ambient region, effect was enhanced with the addition of the secondary tabs when compared to the primary tab geometry; see

Figure 5.33a. Specifically, in the plume region the $\overline{w}$ magnitudes were seen to be significantly larger than those seen for the primary tab geometry ($0.21U_{up}$ compared to $0.16U_{up}$). It was instructive to note the downward flow below the projected tip of the tab (for the modified tab geometry) had nominally the same value as was seen for the primary tab geometry at the same location. This observation was in agreement with the earlier results which showed that the effects of the secondary tabs were limited to the portion of the flow above the projected tunnel top wall.

Figures 5.34b and 5.35b show the $\overline{w}$ velocity contours at x/b=2.0 for the primary tab and modified tab geometries respectively. These data indicated that the plume region continued to have a strong $+\overline{w}$ velocity component although the magnitudes had decreased. The downward penetration of the shearlayer also appeared to be slowing as expected since the high x-momentum of the core fluid will overcome the downward momentum of the fluid redirected by the tab.

The turbulence intensity data for the y-z plane velocity components are presented in Figures 5.36-5.39. The shear layer was aligned with the side walls and tab surfaces and the peak values occurred in the plume region of the flow. Note that the location of the high fluctuations corresponded to the location of the largest gradient in the average streamwise velocity as would be expected if these peak values represented the effects of turbulence kinetic energy production. The peak values for the lateral and normal velocity fluctuations were nominally $0.16U_{up}$. This was in contrast to the streamwise velocity component which showed a peak fluctuating value of nominally $0.18U_{up}$ for the primary tab geometry and $0.21U_{up}$ for the modified tab geometry. The fluctuating results were similar when the primary tab and modified tab geometry results were compared.

5.6.4 In-plane Vector Results and Comparison

Vector fields made up of the $\bar{v}$ and $\bar{w}$ values were plotted to better allow the y-z plane features of the flow field to be determined. Each data set is presented with both scaled and unscaled vectors, see Figures 5.40-5.43.

The scaled y-z plane vector plots are presented in Figures 5.40a -5.43a. All four figures showed similar trends with varying magnitudes. The region behind the tab (in the wake of the tab) had a very small in-plane velocity with respect to the free stream value. This was expected in that the fluid flow in this region will be a result of either recirculation of core fluid or entrainment of ambient fluid. Both sources were expected to provide velocity magnitudes that were small compared to the approach velocity. Note that the vectors in this region were directed in the -z-direction which indicated there was an entrainment of ambient fluid into the core flow. A strong in-plane velocity was encountered primarily in the -z direction for z/b<-0.65 and y/b=0. This result was expected since the flow should be symmetric about the centerline of the tab. The y-z plane velocity vector in this region was found to be the strongest in the flow (nominally $0.27U_{up}$ for the modified tab geometry and 0.26 for the primary tab geometry at x/b=1.2). For y<-0.5b and z<0 (within the projection of the tunnel) there was a very strong outward velocity as shown by the vectors which pointed in the -y-direction (away from the primary tab). The y-z plane velocity vector was dominated by $\bar{v}$ in this region.

An interesting feature of these vector plots was found in the plume region above the projected top of the tunnel wall. There was a strong ejection of fluid from y=-0.7b to -1.1b for z greater than 0. This ejection penetrated up to z=0.5b in the ambient region for

the modified tab geometry. The velocity magnitudes in this region were near, but slightly less than, the velocity magnitudes seen below the tab in the core region (i.e. $0.24U_{up}$ compared to $0.27U_{up}$ for the modified tab geometry at x/b=1.2). This observation indicated that the ejection of fluid from the core region was a strong feature of the flow field. Note that the velocities in the plume represented the most significant difference in the velocity field of the two geometries. Specifically, the y-z plane velocities were noticeably smaller in the plume region for the primary tab geometry at the same downstream location when compared to the modified tab geometries at the same location (i.e. $0.21U_{up}$ compared to $0.23U_{up}$ at x/b=1.2).

Unscaled vectors, i.e. vectors with constant length, are also presented with y-z plane streamlines in Figures 5.40b-5.43b. Simplified plots with streamlines and the indicated singular points are presented in Figures 5.40c-5.43c. These data indicated four singular points in the flow fields (2 nodes and 2 saddles) for all but the primary tab geometry at x=1.2b which showed two singular points (a node and a saddle). (Note the node at z/b=0.3 and y/b=-0.9 in Figure 5.43c does not show a spiral to the node. This is inferred to be a result of the data grid spacing.) At the singular points the in-plane velocity directions were indeterminate ($\overline{v}$ and $\overline{w}$ were both zero; see Figures 5.40c-5.43c) and a singularity resulted. In this flow field there were two saddle points and two nodal points. The two nodal points for these data indicated a flux of mass out of the y-z plane by the streamlines which pointed into both nodes. Figures 5.40d-5.43d also show schematic outlines of the domains for which an even number of nodes and saddles must be present. The surface was made up of a collapsed sphere with 2 holes ($\chi_{surface}=0$) which was balanced by the even number of nodes and saddles shown for all of the data.

5.6.5 Reynolds Shear Stress Results and Comparison

The turbulent shear stresses were calculated using the x-array data at x/b=1.2 and 2.0. There were two regions of peak negative values in the $\overline{u'v'}/U_{up}^2$ data; see Figures 5.44-5.47. These local minima occurred along the side wall and in the plume region. The stress values along the side walls were nominally the same with a peak value of $\overline{u'v'}/U_{up}^2$=-1.25x10^{-2} for both geometries. The results from the plume region showed that the modified tab geometry experienced an increased stress level when compared to the primary tab geometry. Specifically, peak values were nominally $\overline{u'v'}/U_{up}^2$=-1.25x10^{-2} for the primary tab geometry and $\overline{u'v'}/U_{up}^2$=-1.50x10^{-2} for the modified tab geometry. This was consistent with the the results in section 5.6.2 which showed an increased growth rate in the momentum thickness of the modified tab geometry in the plume region. It was instructive to note that the peak value for the primary tab geometry (-1.25x10^{-2}) corresponded to that measured for the shear layer on the side wall of the tunnel indicating that the shear stresses experienced in each region were comparable. This further reinforced the observation that the shear layer in the plume region for the primary tab geometry was not significantly different from the shear layer for the untabbed jet, although it was significantly displaced into the ambient region.

Both geometries also showed a region of positive stress in the shear layer aligned with the side of the tab. This corresponded to the change in sign of $\partial \overline{u}/\partial y$ in the average streamwise velocity field. Note also that the peak positive stress values were

significantly increased for the modified tab geometry. In the core region, where $\partial \bar{u} / \partial y$ was equal to zero the corresponding stress values were also nominally equal to zero.

Renormalizing these data as $\overline{u'v'} / \tilde{u}\,\tilde{v}$ provided information on the cross-correlation coefficients of the fluctuations in the data. These results, presented in Figures 5.48-5.51, showed that the peak correlations occurred in the regions where the peak stress values were noted.

The $\overline{u'w'} / U_{up}^2$ stress values are presented in Figures 5.52-5.55. These data showed positive values in the plume region as expected ($\partial \bar{u} / \partial z$ decreased in the entire region). The peak values again showed a significant increase from 1.25×10^{-2} for the primary tab geometry to 1.50×10^{-2} for the modified tab geometry. This again supported the previous observation of the increased growth rate in the plume region shear layer for the modified tab geometry. Note that along the wall, where the shear layer was oriented nominally vertically, the stress values were nominally zero.

The cross-correlation data, Figures 5.56-5.59, show that the peak positive correlations occurred in the region of the peak stress values. Again values were nominally the same for both geometries as was seen in the lateral results.

5.6.6 Qualitative Vorticity Results

The flow pitch angles were too severe near the exit of the jet for the use of x-arrays; therefore, quantitative measurements were not made near the exit, as was noted in Chapter 3. A cross-vane vorticity probe was used to determine some characteristics of the streamwise vorticity field very near to the exit of the tunnel . Figures 5.60 and 5.61

show the results for the downstream locations from 0.1 to 0.4 for the primary tab and modified tab geometries respectively. These data were instructive in that they clearly illustrated the effect of passive mixing tabs on on a jet flow as well as the differences between the geometries.

There were two regions of streamwise vorticity shown for both geometries . The region of positive sense vorticity (a result of the re-orientation of the vorticity in the boundary layer) had a sign that was as expected for a "necklace" vortex about a protrusion into the flow. The negative region of streamwise vorticity was a result of the vorticity fluxed into the flow by the upstream static pressure distribution (i.e. the "pressure hill").

A significant portion the streamwise vorticity was seen above the projected exit plane of the tunnel for both geometries at all locations. It was interesting to note that both geometries showed a significant portion of streamwise vorticity in the ambient region at the closest location x/b=0.1. These observations indicated the strong upward expansion of the flow occurs at the exit of the jet. Both geometries also showed the negative regions to be several times larger in area than the positive sense regions for $y<0$.

The qualitative use of the cross-vane vorticity probe did not provide quantitative results to be presented in this section. However, it was instructive to note that the rate at which the cross-vane probe rotated did vary visibly as the downstream distance was increased. It was observed that, at the more upstream locations, the cross vane probe spun "faster". Moreover, the delineation between "spin" and "no spin"was more clearly defined at the farther upstream locations. As the downstream distance was increased the probe spun slower and the boundaries become more difficult to discern. Additionally, the

area describing the regions of streamwise vorticity also increased as the downstream distance was increased. Note that the one exception to this trend was observed for the positive region in the primary geometry. These two observations implied that the negative sense streamwise vorticity in the flow was introduced very near to or upstream of the tunnel exit, and that the increased area was a result of the diffusion of this vorticity. This observation was supported by prior results that showed that it was the upstream pressure distribution, not the pressure distribution on the tab face that provided the major flux of the streamwise vorticity in the flow (Zaman et. al. (1994)). The one exception to this evolution was the region of positive sense vorticity in the primary tab geometry case which did not increase in area with increasing downstream distance. This was probably a result of its interaction with the larger and stronger negative sense vorticity.

The cross-vane observations also illustrated the differences between the two geometries. Specifically, the negative sense regions were slightly larger in area for the modified tab geometry than for the primary tab geometry at the same x-locations. This suggested a slightly larger total circulation for the modified tab geometry. The positive sense region was significantly larger in area for the modified tab geometry. This implied a significant increase in the total circulation for this region of vorticity.

5.6.7 Quantitative, Spatially and Temporally Averaged Streamwise Vorticity Results

The $\overline{v}$ and $\overline{w}$ data were processed using (3.22) to provide the spatially averaged streamwise vorticity, $\overline{\omega_x}^*$. Figures 5.62 and 5.63 show the streamwise vorticity results. These data clearly showed two counter rotating regions of streamwise vorticity. The

larger region was the negative sense vorticity created as a result of the upstream static pressure gradient on the top wall of the tunnel. This region had a peak value of $\overline{\omega_x}^*$=-1.60 for the primary tab geometry at x/b=1.2; see Figure 5.62a. The smaller region, a result of the re-orientation of the approach boundary layer vorticity, showed a peak positive vorticity value of nominally $\overline{\omega_x}^*$=1.22.

The equivalent data for the modified tab geometry at x/b=1.2 are presented in Figure 5.63a. These data showed the same two regions of counter rotating vorticity as were seen in the primary tab geometry data, however the effects of the secondary tabs were again illustrated in the differences between the data. The positive sense vorticity was nominally the same size and magnitude as was observed for the corresponding region for the primary tab geometry, although the peak value increased slightly to $\overline{\omega_x}^*$=-1.74 for the modified tab geometry. This indicated that the total circulation in the negative sense region was slightly higher for the modified tab geometry.

The primary difference between the two geometries was seen in the positive sense vorticity at x=1.2b. This region increased significantly in both area and magnitude (and hence in circulation) for the modified tab geometry. The peak value increased from $\overline{\omega_x}^*$=1.22 for the primary tab geometry to $\overline{\omega_x}^*$=1.67 for the modified tab geometry.

The downstream evolution of the streamwise vorticity is shown in Figures 5.62b and 5.63b. These data show that the streamwise vorticity magnitudes decreased as the downstream distance was increased. Note that the peak values were nominally the same for both geometries at this location ($\overline{\omega_x}^*$=-1.3 and $\overline{\omega_x}^*$=1.0). The increased spacing between the vorticity contours from x=1.2b to x=2.0b indicated the presence of

significant diffusion of vorticity within the flow field. The vorticity contours also indicated that the presence of the large scale rotation in the plume region described in section 5.6.2.

These data further clarify and explain the vector patterns shown in section 5.6.4. The two areas of counter rotating vorticity act as a "pump" to eject fluid from the core region into the ambient region. A "current" was created in between the two regions of vorticity because of the counter rotation. A fluid element caught in this "current" was ejected from the core region. The exchange of fluid seen in the tabbed jet was a result of this pumping action. Note that this explanation of governing phenomena is inherently different from that which would be related to enhanced turbulence intensities and shear stresses. Figure 5.64 shows a combined plot of the streamwise vorticity and the y-z plane vectors for the modified geometry at x/b=1.2. These data show that the ejection of fluid from the core occurred between the two regions of vorticity in the flow. Note that the y-z plane velocities seen in the plume between the two regions of streamwise vorticity had magnitudes near the maximum y-z plane velocity values. The flow accelerated between the regions and quickly decelerated after exiting the fluid "pump".

The streamwise vorticity results, in conjunction with the upstream static pressure results, were also used to infer some of the upstream flow mechanics. It was shown that there existed an adverse pressure gradient on the surface of the tunnel upstream of the tab. However near the exit of the tunnel the pressure gradient became favorable for the modified tab geometry in the region of y=-1.1b to y=-0.8b for x=-0.05b. In this region the sign of $\partial P/\partial y$ changed. Note that the sign of $\partial P/\partial x$ also changed for y constant over the same range of y values. It was clearly illustrated that the additional flux of vorticity

from the pressure gradient in this region significantly increased the streamwise vorticity in the re-oriented boundary layer vorticity (i.e. the positive region for $y<0$).

A schematic representation of the vorticity connections upstream of the tunnel exit can be inferred using a combination of the downstream streamwise vorticity observations and the surface streaking data. Figure 5.65 shows the inferred connections from these data. Specifically, the solenoidal condition requires that a vorticity filament: 1) end at a wall (as a singular point for a viscous fluid), 2) end at infinity, or 3) forms a closed loop. The regions of streamwise vorticity must, therefore, connect from one side of the tab to the other since there is no indication of a swirl pattern on the $\pm y$ sides of the region upstream from the tabs. The pattern shown is also compatible with the inferred pattern from the topological analysis. It is instructive to note that the vorticity which corresponds to N3 in Figure 5.11 did not appear in the downstream measurements. It is inferred that this region of vorticity must be weak when compared to the other regions.

5.6.8 Availability of Results

The experimental data described above is considered to represent a valuable resource for identifying the physics of tab jet flows and for the purpose of CFD code validation. For the latter, it is noted that the upstream boundary conditions are well defined as are the pressure values that will be part of the solution.

The interested reader may access these data by contacting Dr. John Foss at Michigan State University via e-mail at foss@egr.msu.edu.

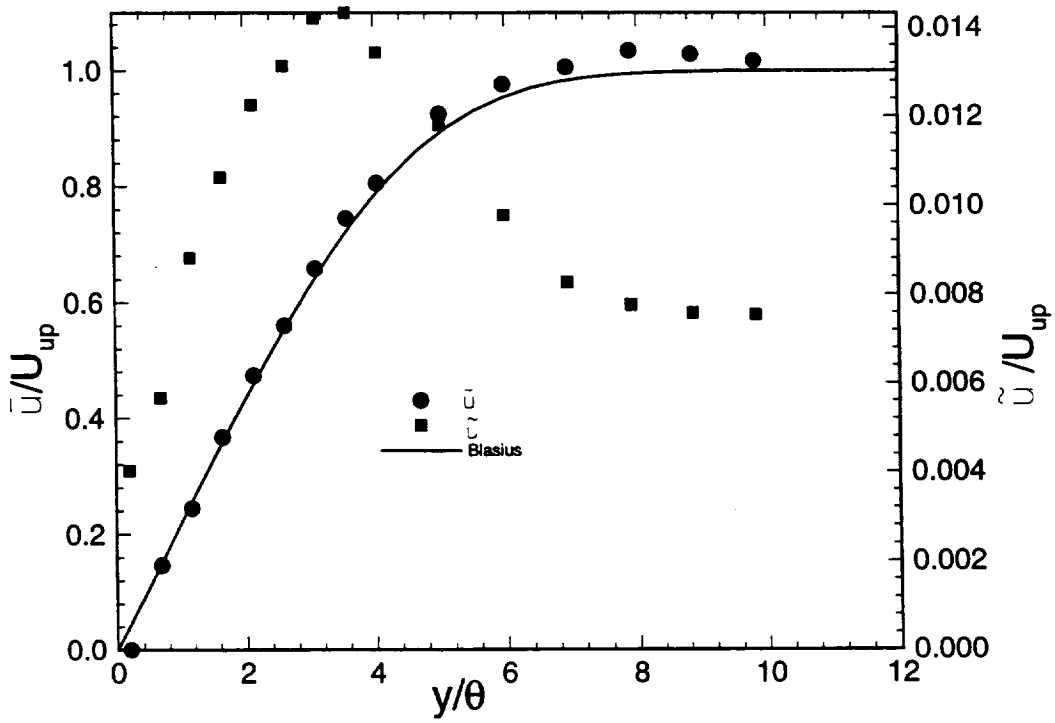

Figure 5.1: Exit boundary layer survey for untabbed jet.

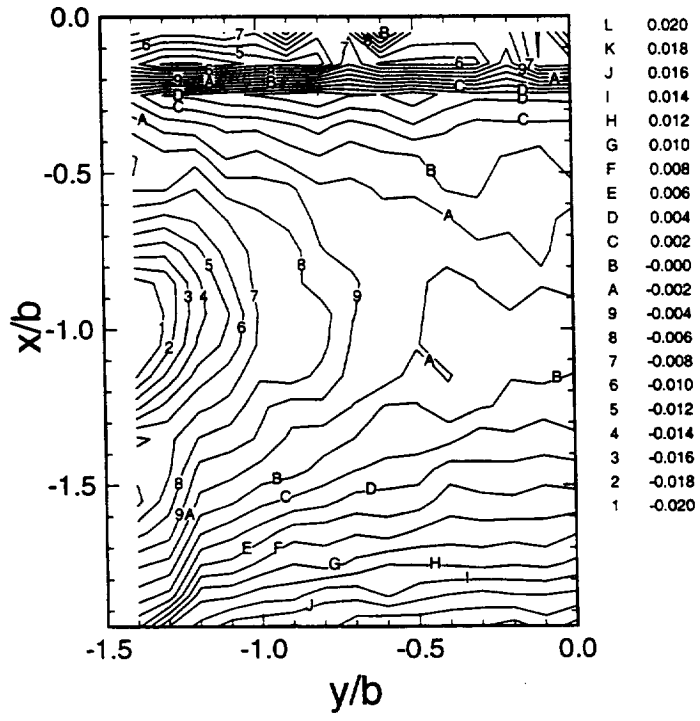

Figure 5.2: Upstream static pressure survey, $(p(x,y)-P_{atm})/0.5\rho U_{up}^2$, for the untabbed geometry.

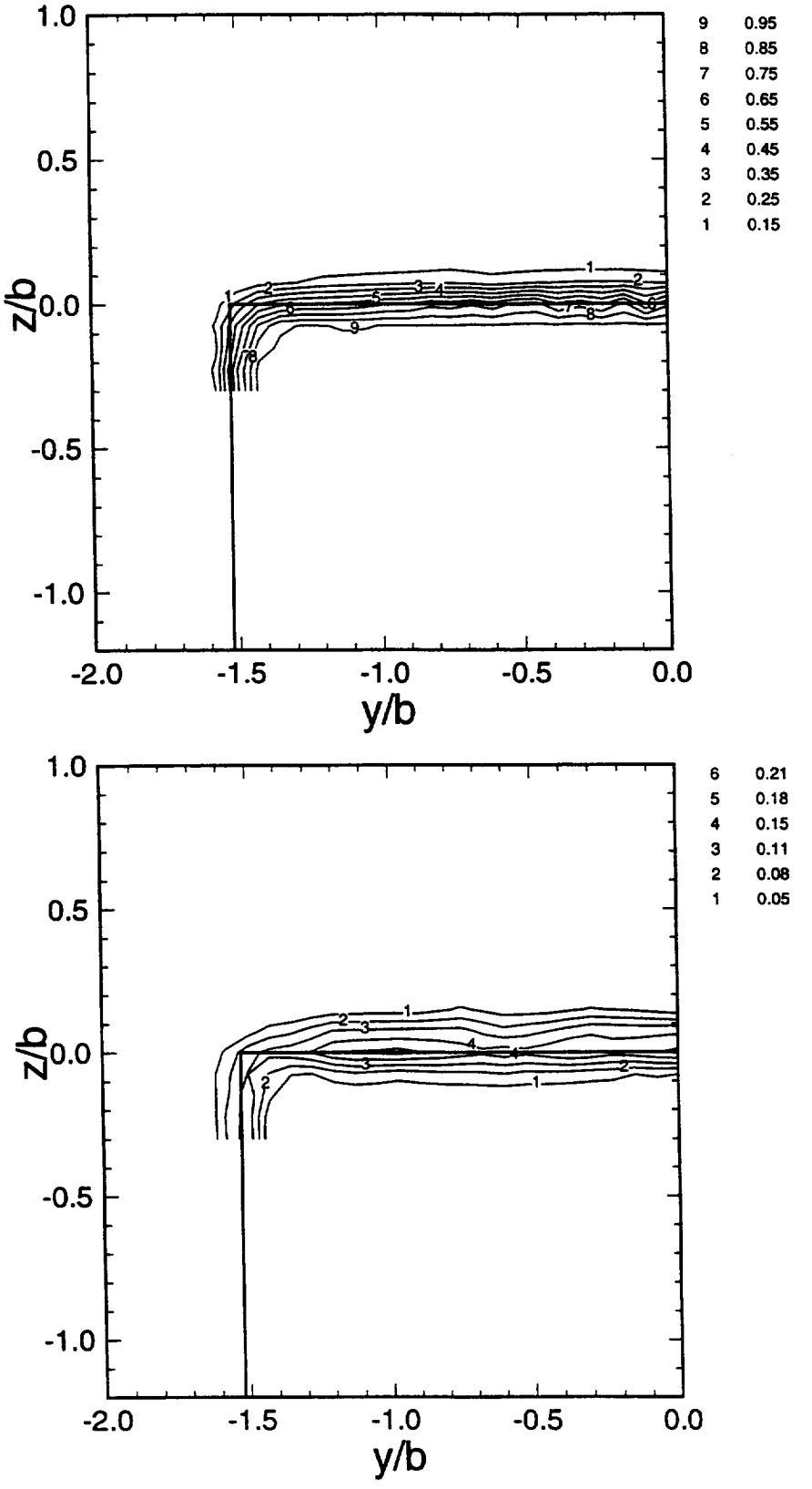

Figure 5.3: Velocity survey for untabbed geometry at x/b=0.7: a) $\bar{u}/U_{up}$, b) $\tilde{u}/U_{up}$.

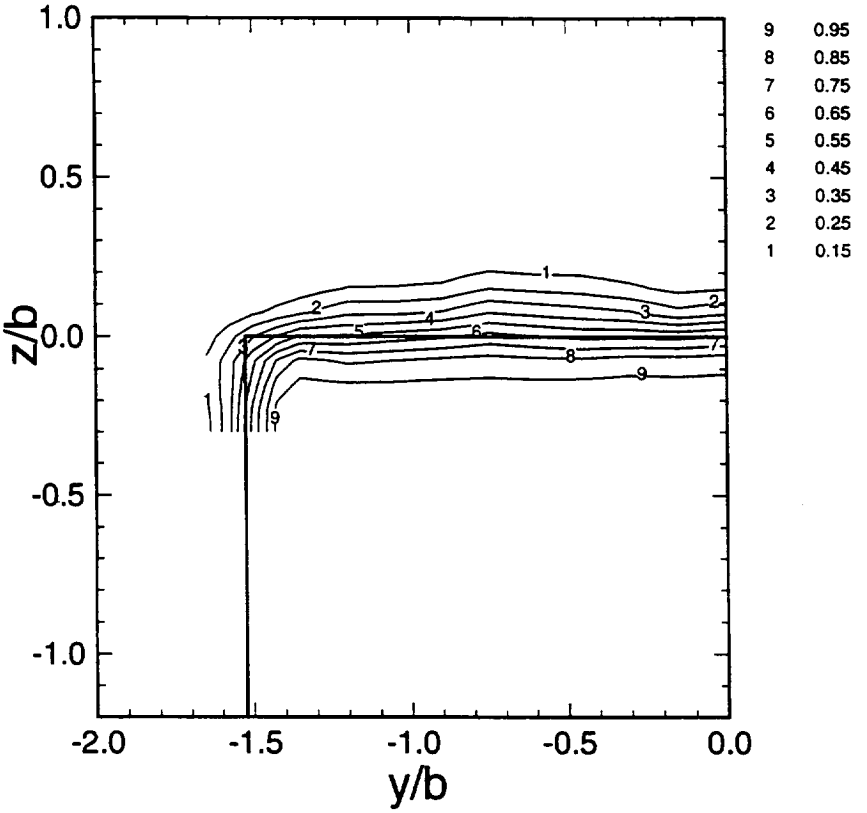

(a)

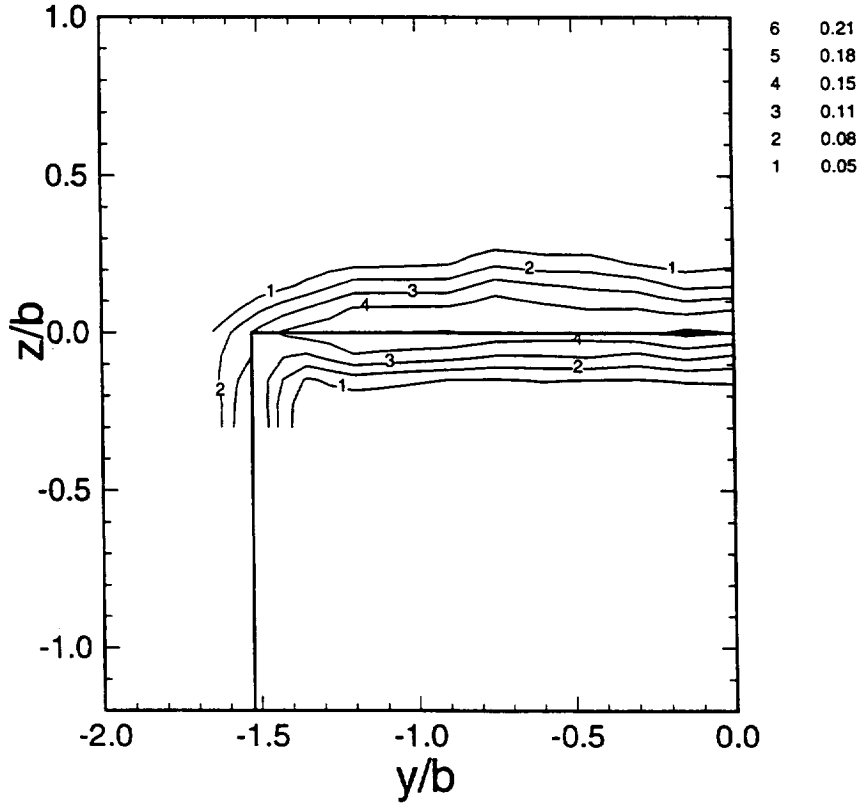

(b)

Figure 5.4: Velocity survey for untabbed geometry at x/b=1.2: a) $\bar{u}/U_{up}$, b) $\tilde{u}/U_{up}$.

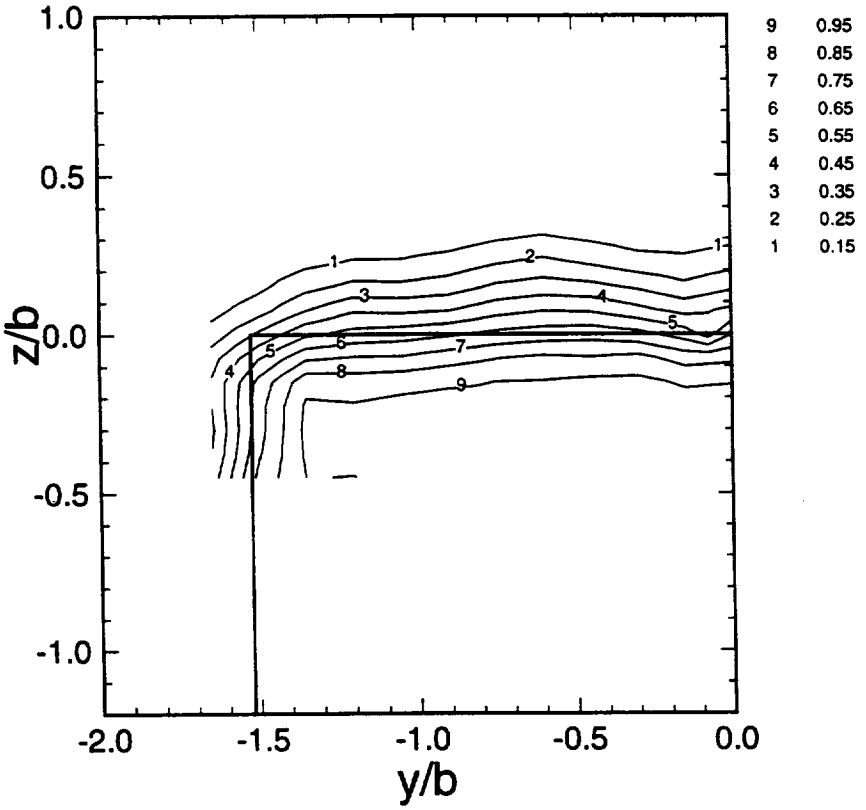

(a)

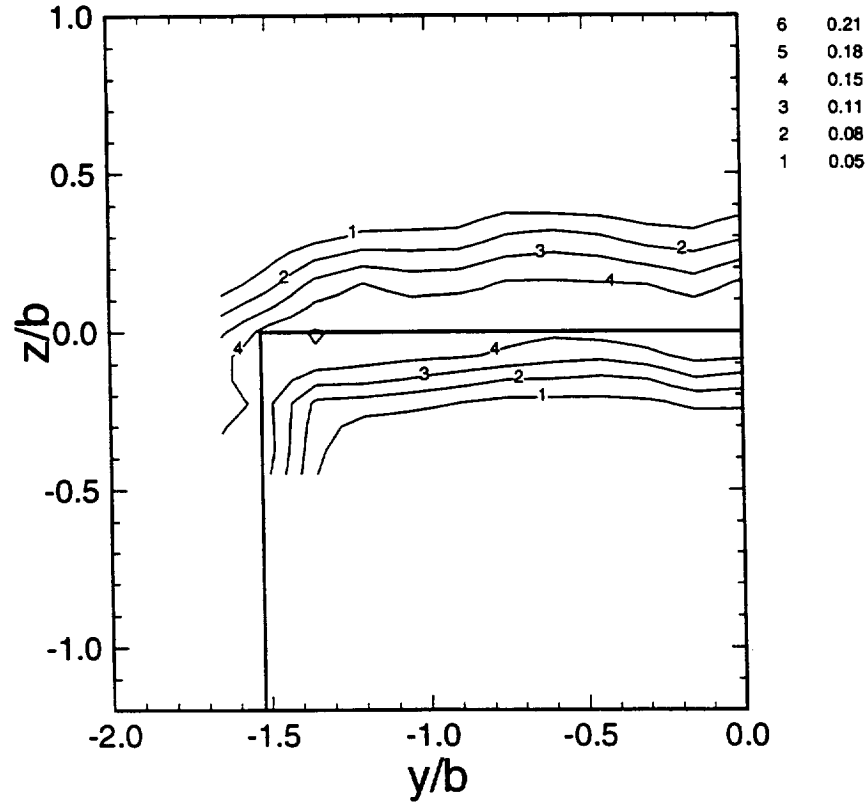

(b)

Figure 5.5: Velocity survey for untabbed geometry at x/b=2.0: a) $\bar{u}/U_{up}$, b) $\tilde{u}/U_{up}$.

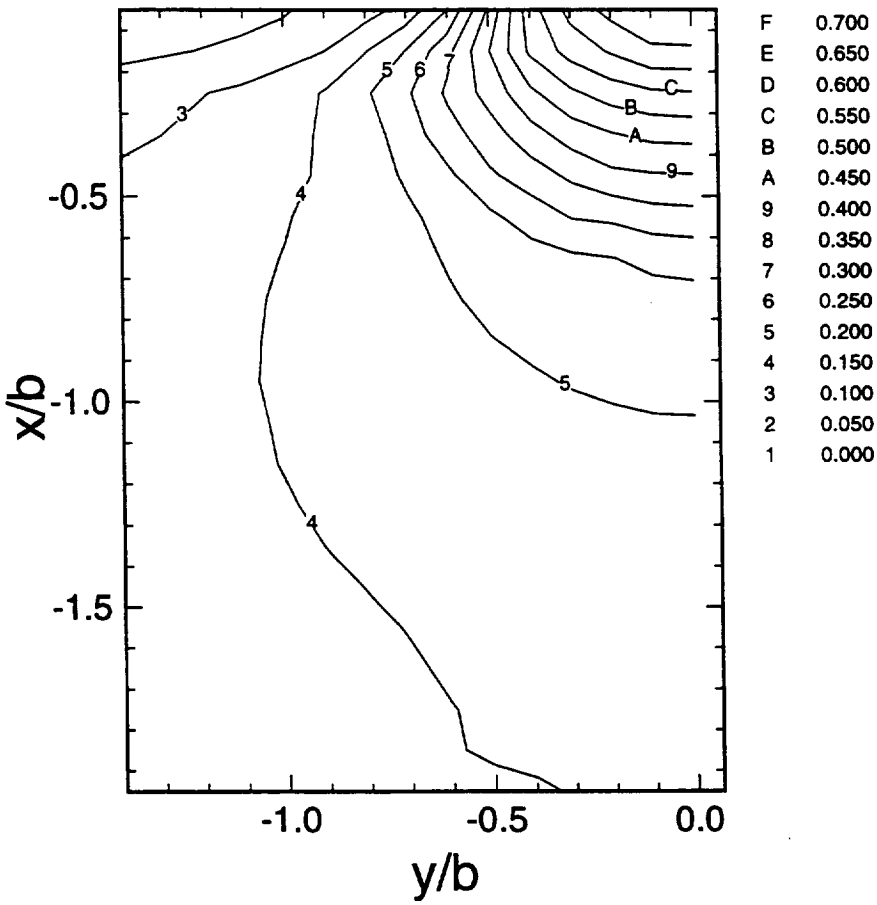

Figure 5.6: Upstream static pressure survey, $(p(x,y)-P_{atm})/0.5\rho U_{up}^2$, for the simple geometry.

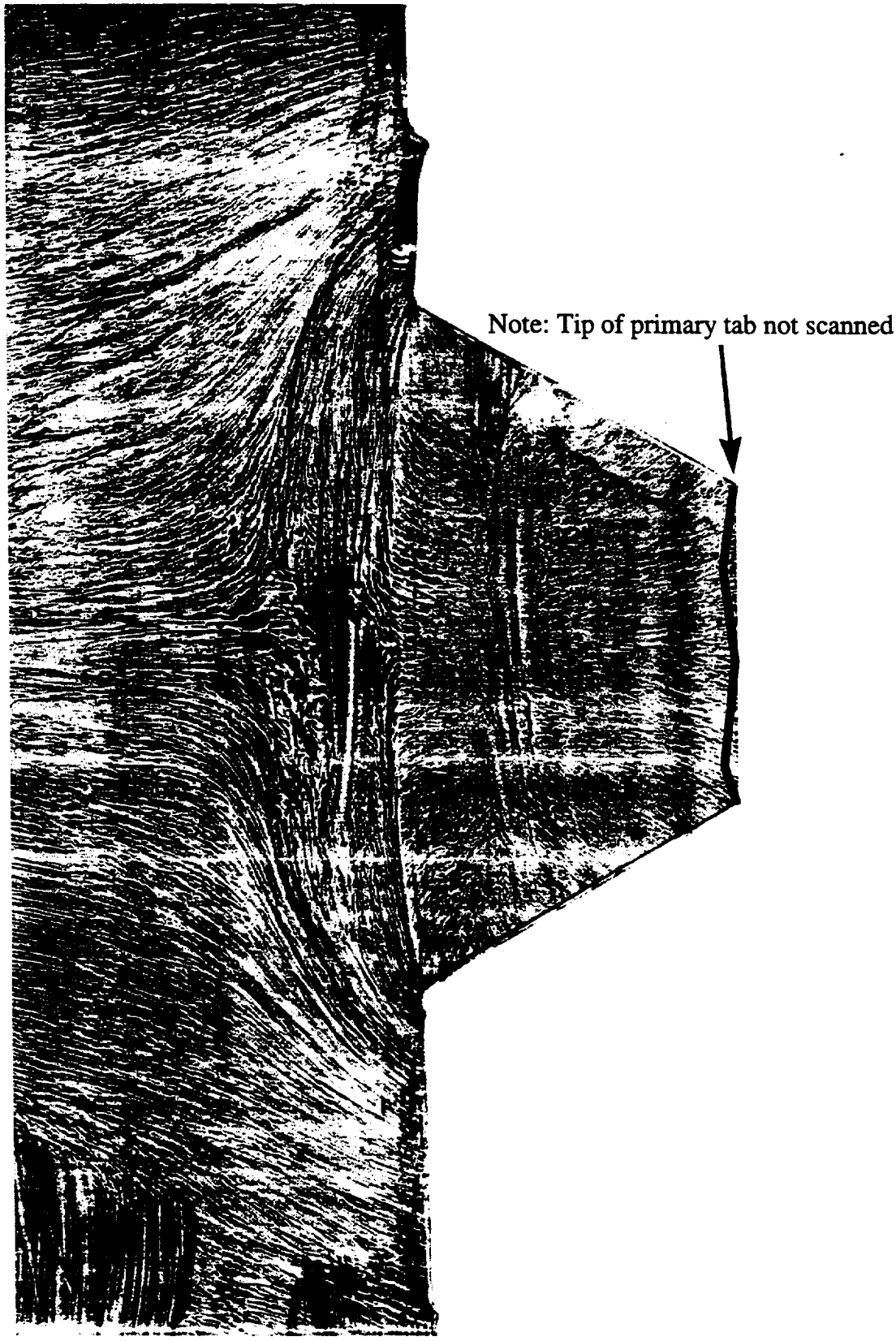

Figure 5.7: Surface streaking results for the primary tab geometry.

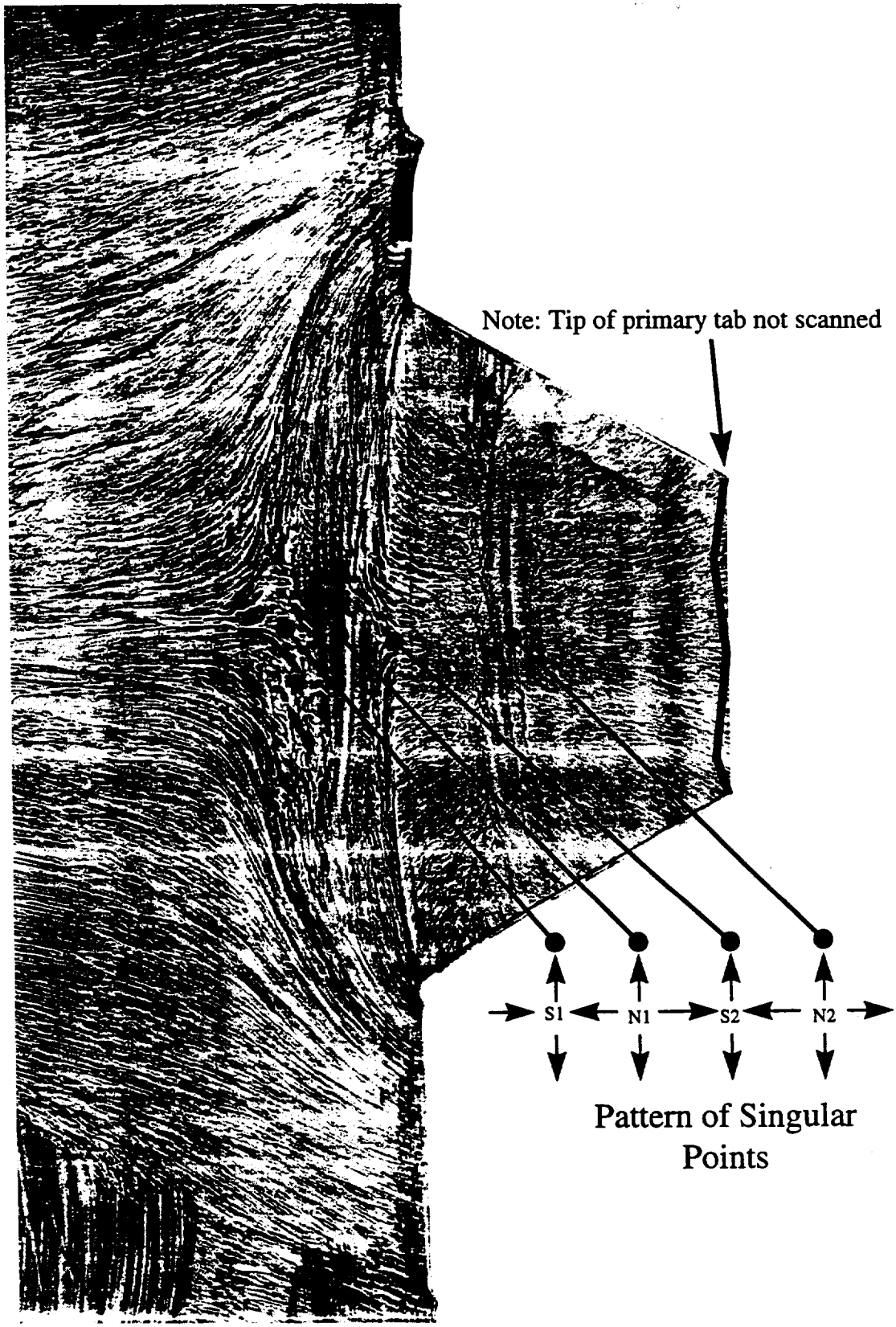

Figure 5.8: Singular points upstream of the primary tab.

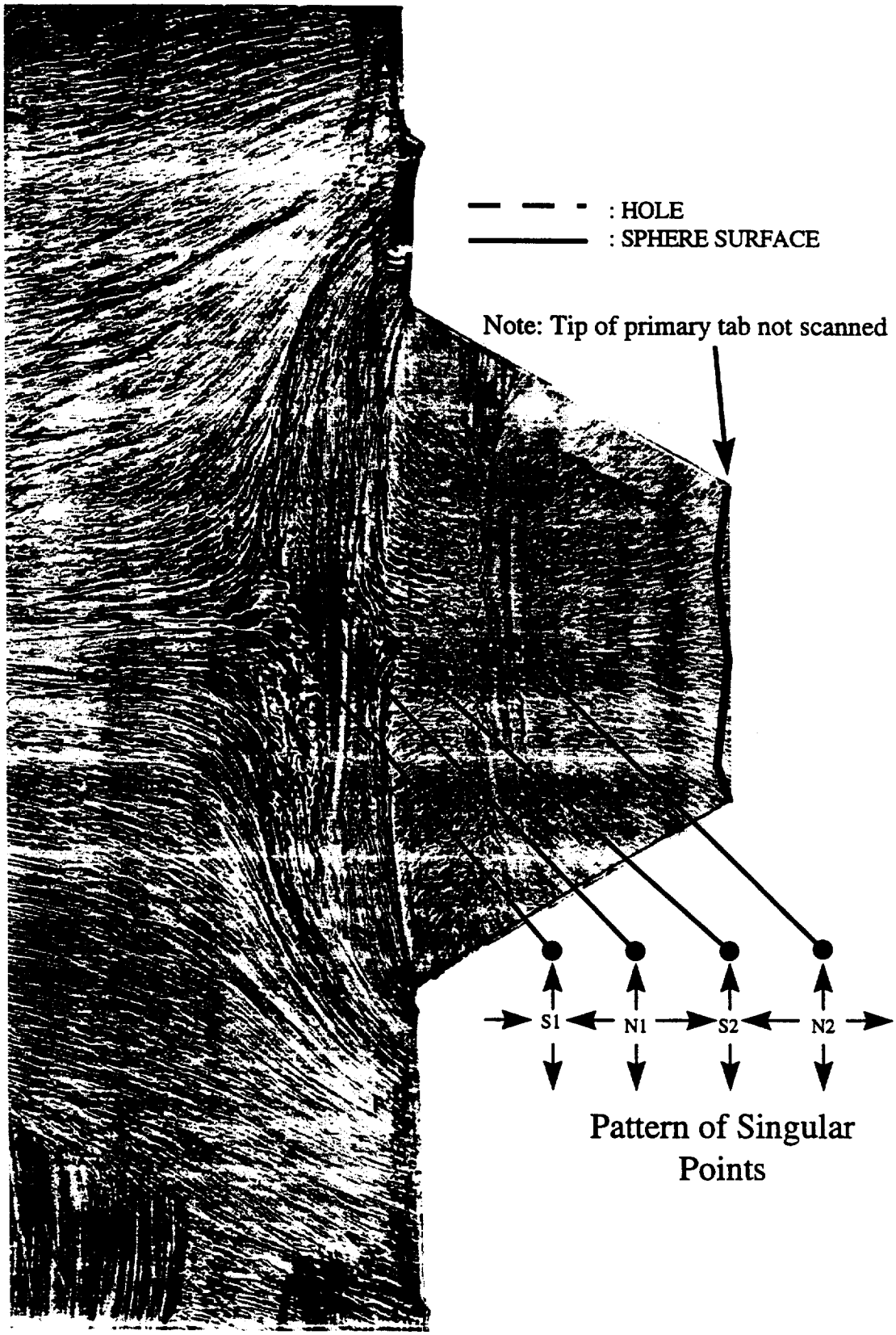

Figure 5.9: Top view topological analysis for the primary tab geometry.

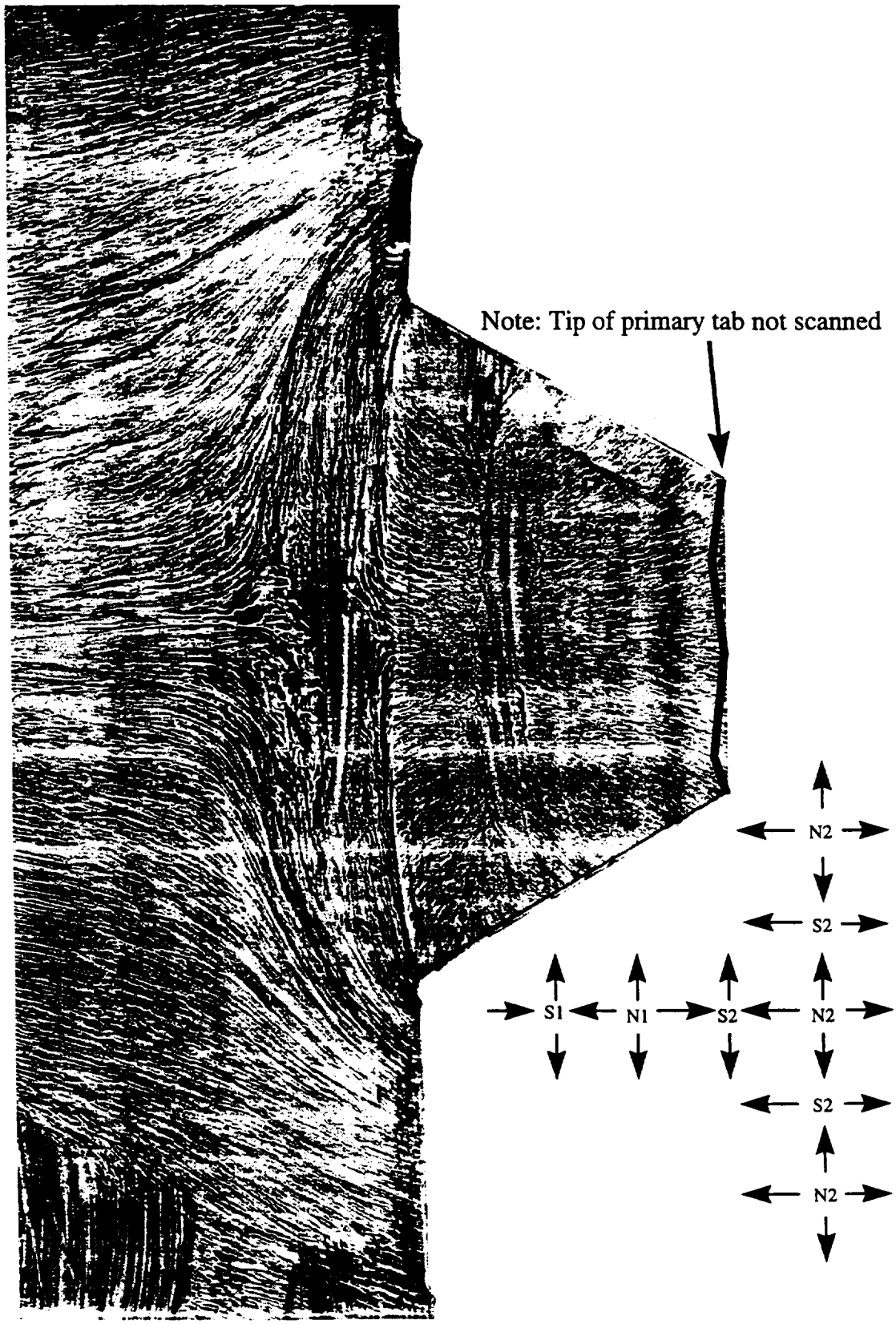

Figure 5.10: Alternate singular point pattern.

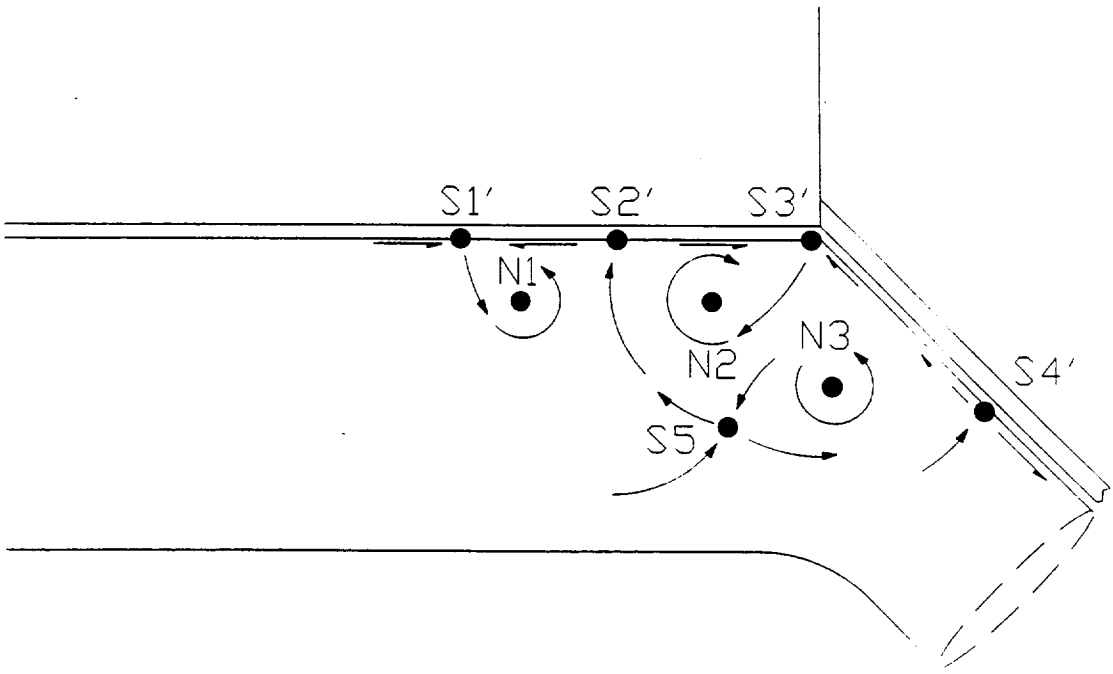

Figure 5.11: Side view, center plane topological analysis of the primary tab geometry.

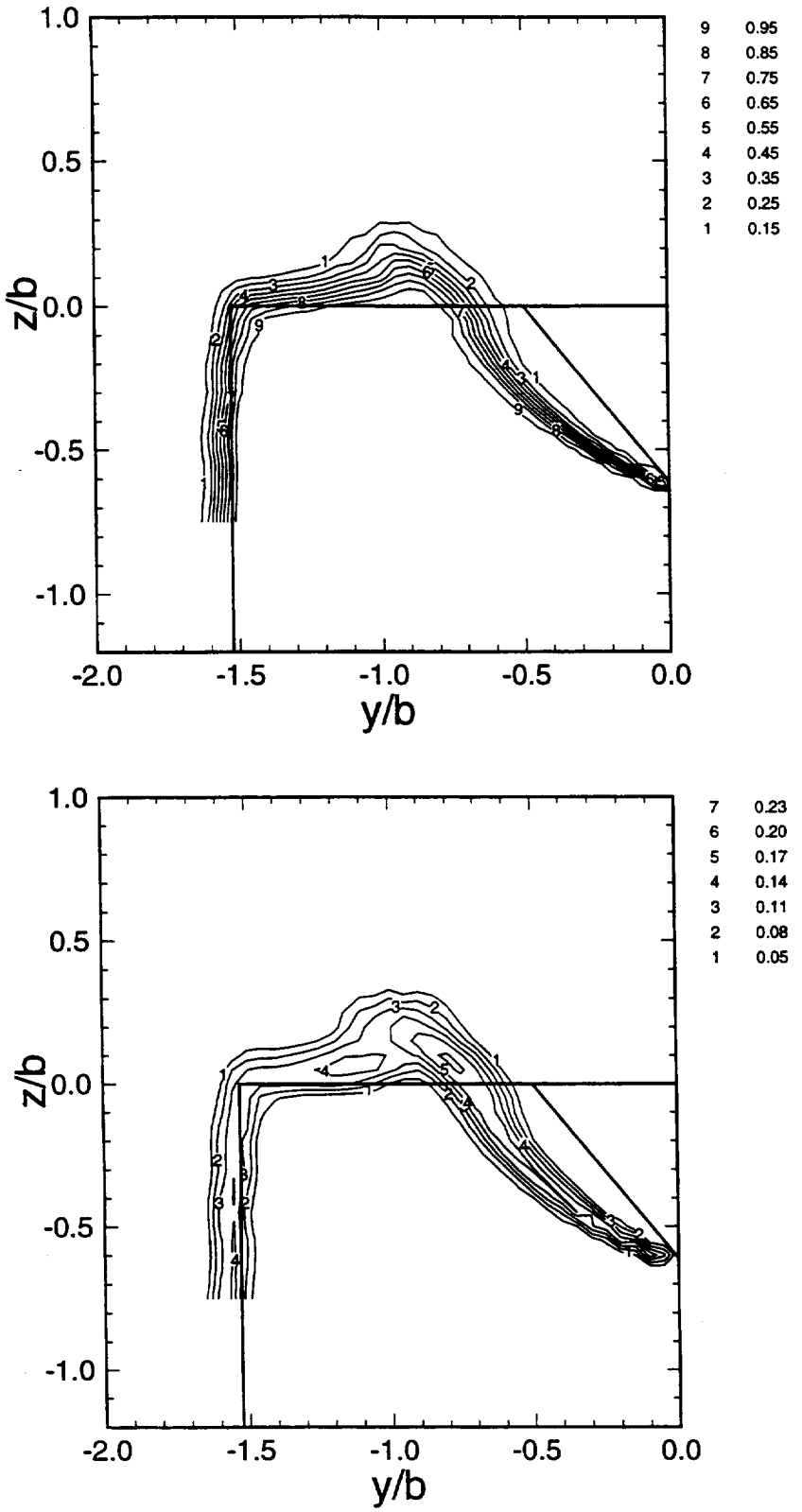

Figure 5.12: Streamwise velocity survey for the primary tab geometry at x/b=0.7: a) $\bar{u}/U_{up}$, b) $\tilde{u}/U_{up}$.

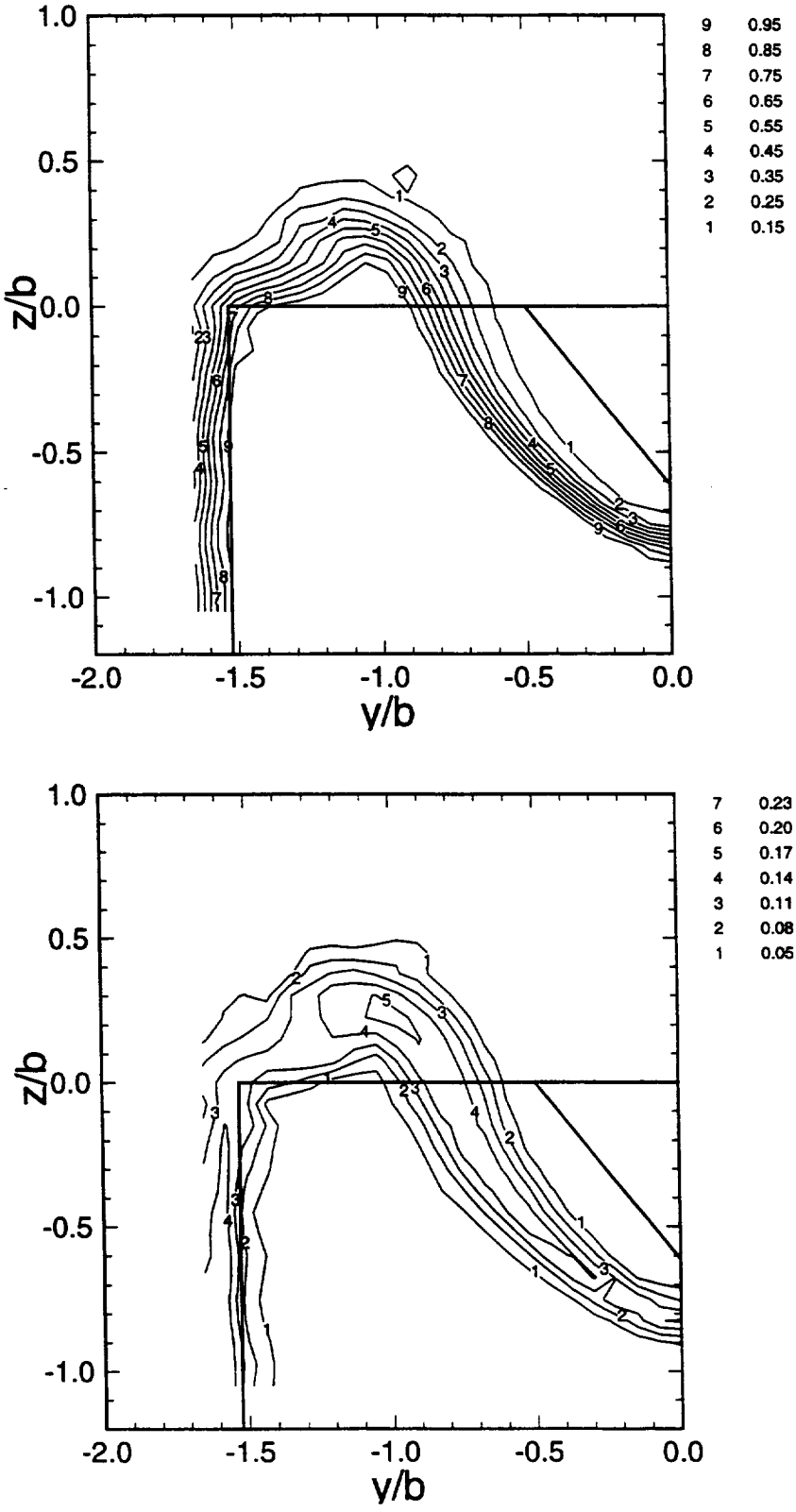

Figure 5.13: Streamwise velocity survey for the primary tab geometry at x/b=1.2: a) $\bar{u}/U_{up}$, b) $\tilde{u}/U_{up}$.

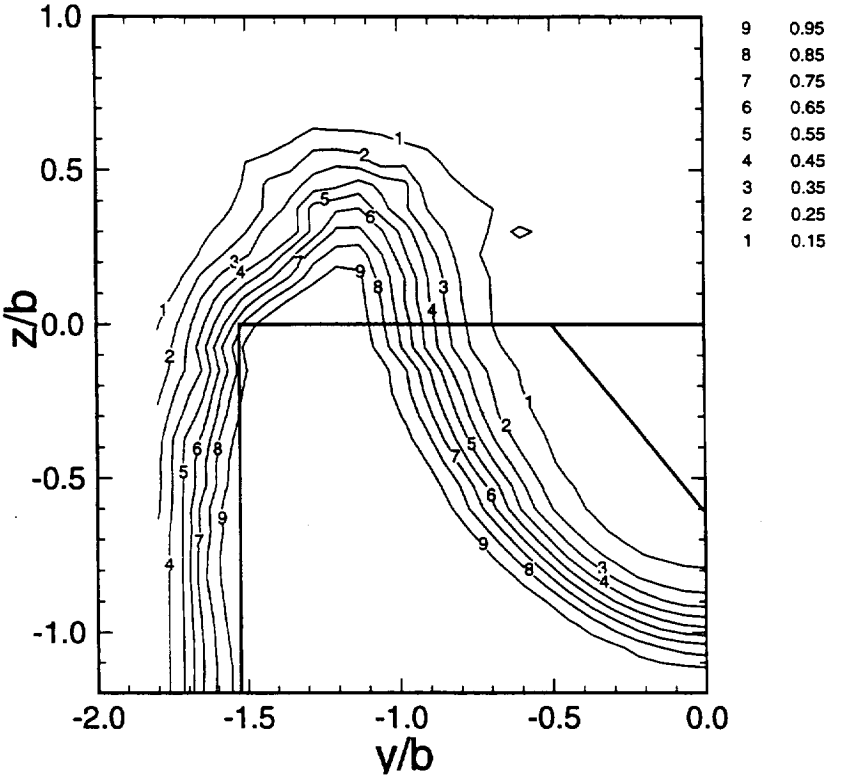

(a)

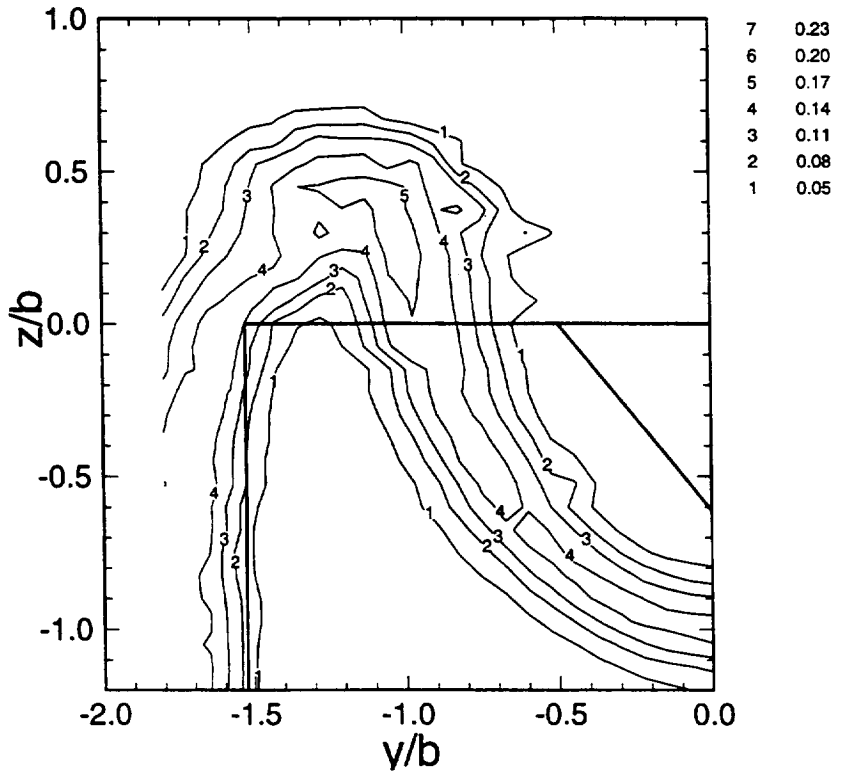

(b)

Figure 5.14: Streamwise velocity survey for the primary tab geometry at x/b=2.0: a) $\bar{u}/U_{up}$, b) $\tilde{u}/U_{up}$.

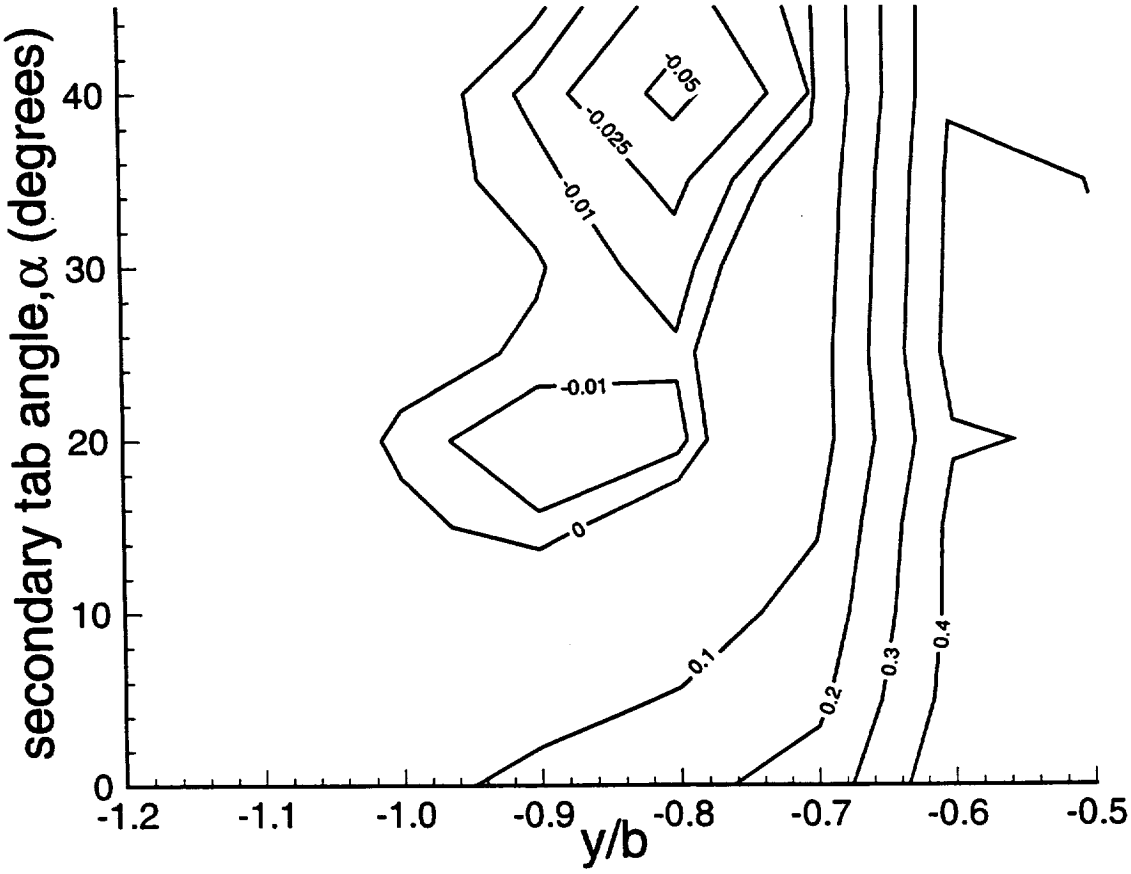

Figure 5.15: Static pressure at x/b=-0.05 versus angle of secondary tabs.

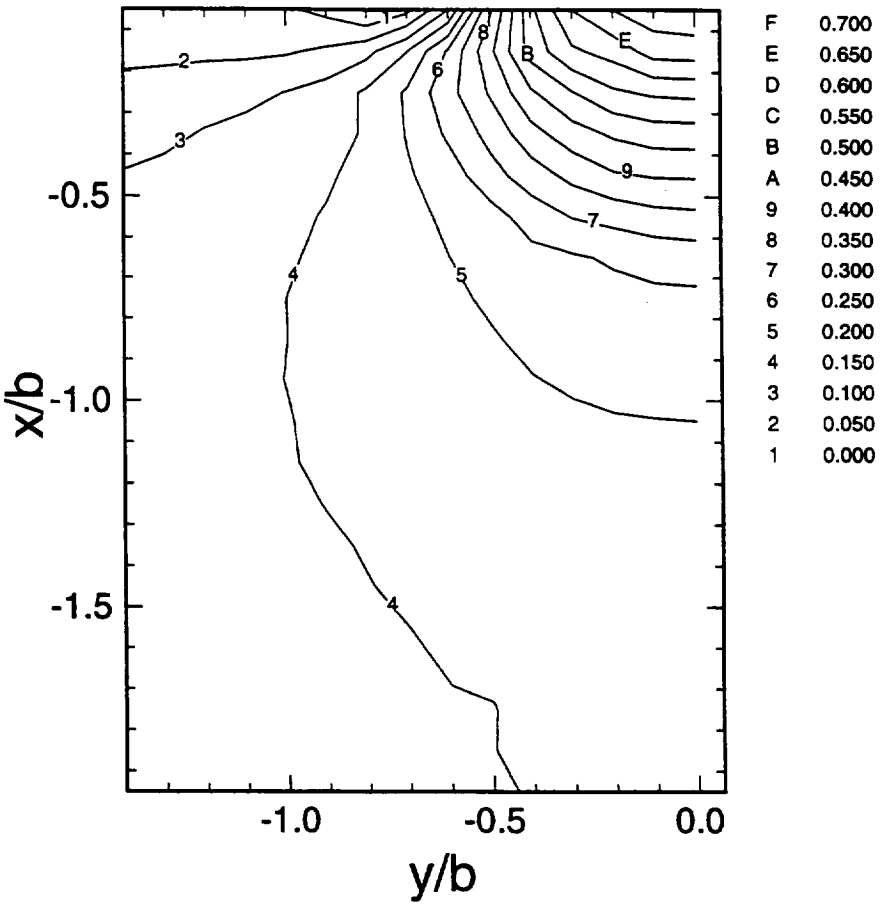

Figure 5.16: Upstream static pressure survey, $(p(x,y)-P_{atm})/0.5\rho U_{up}^2$, for the modified tab geometry.

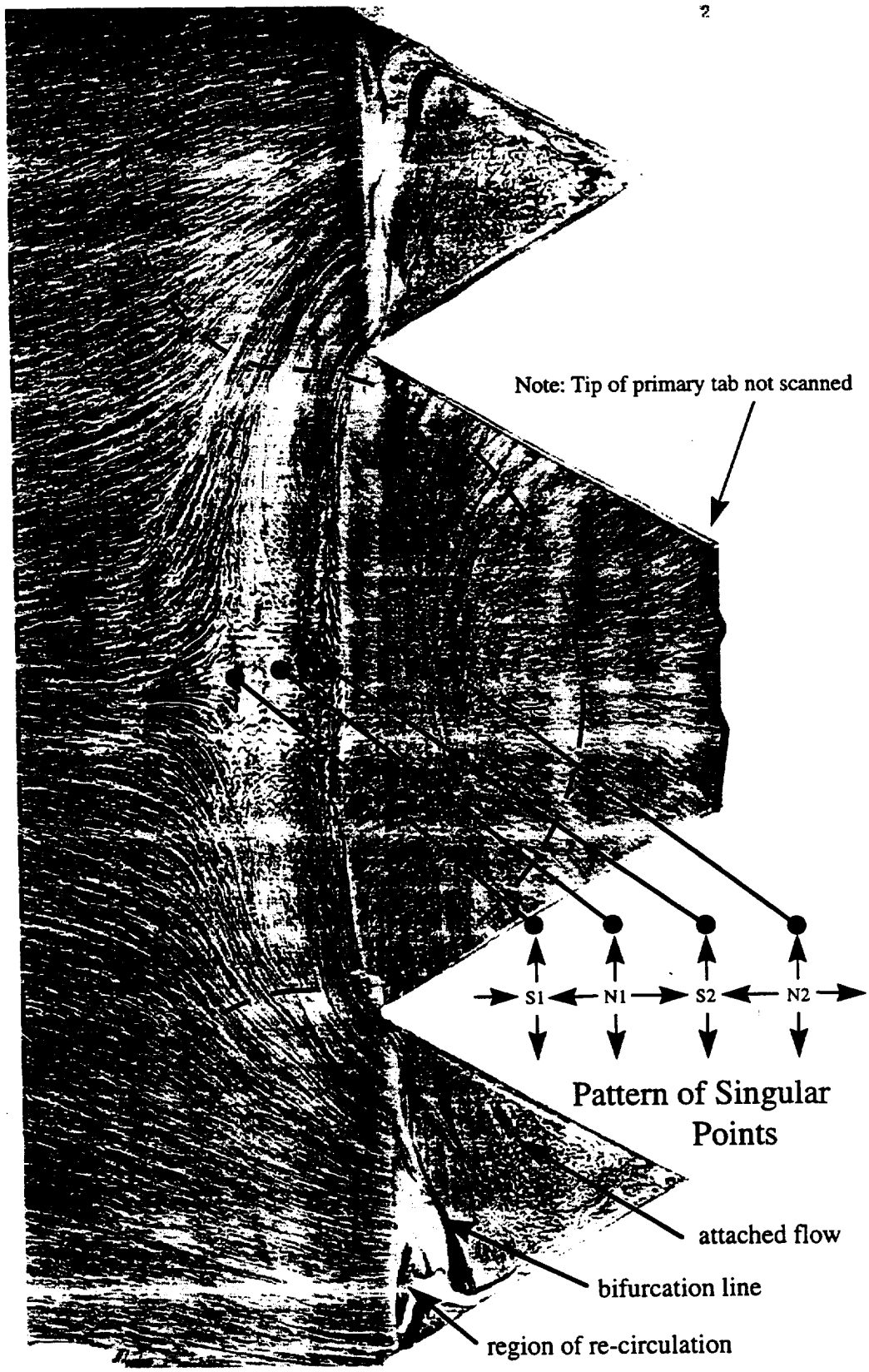

Figure 5.17: Surface streaking results for the modified tab geometry.

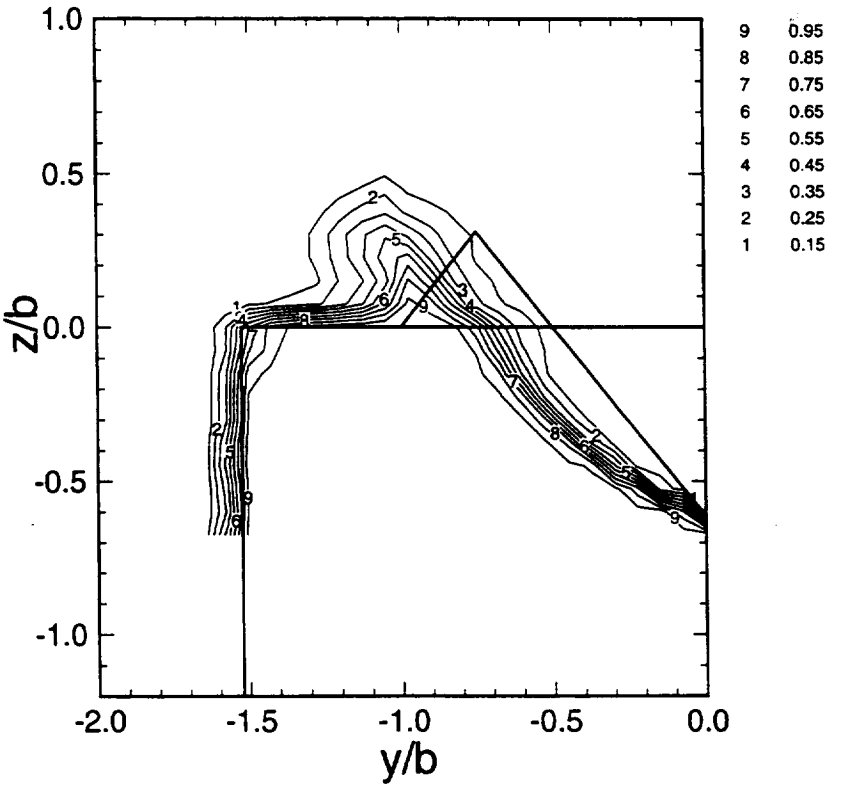

(a)

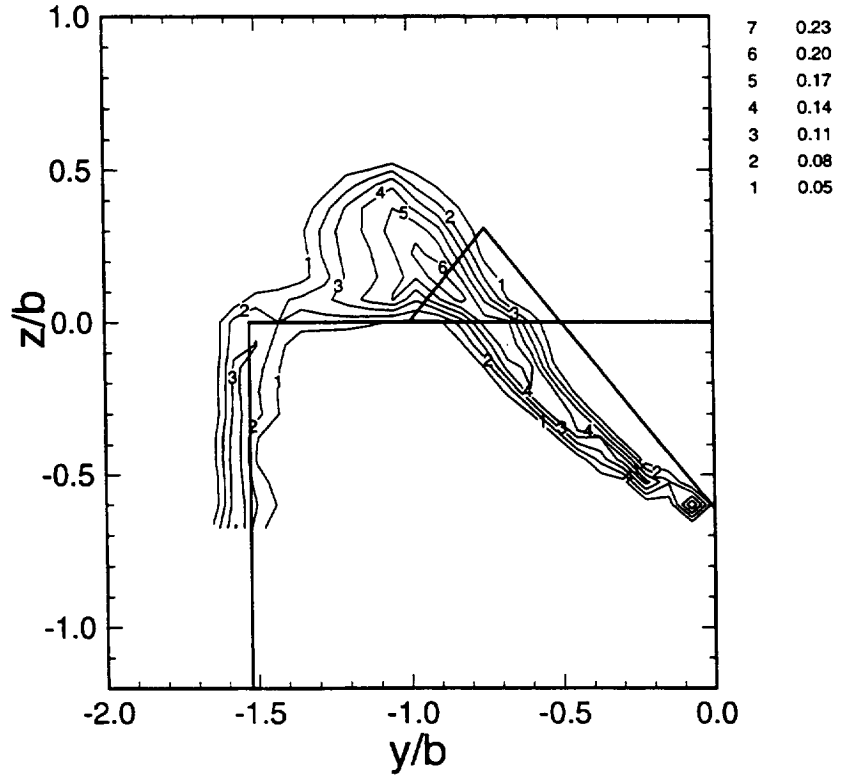

(b)

Figure 5.18: Streamwise velocity survey for modified tab geometry at x/b=0.7: a) $\bar{u}/U_{up}$, b) $\tilde{u}/U_{up}$.

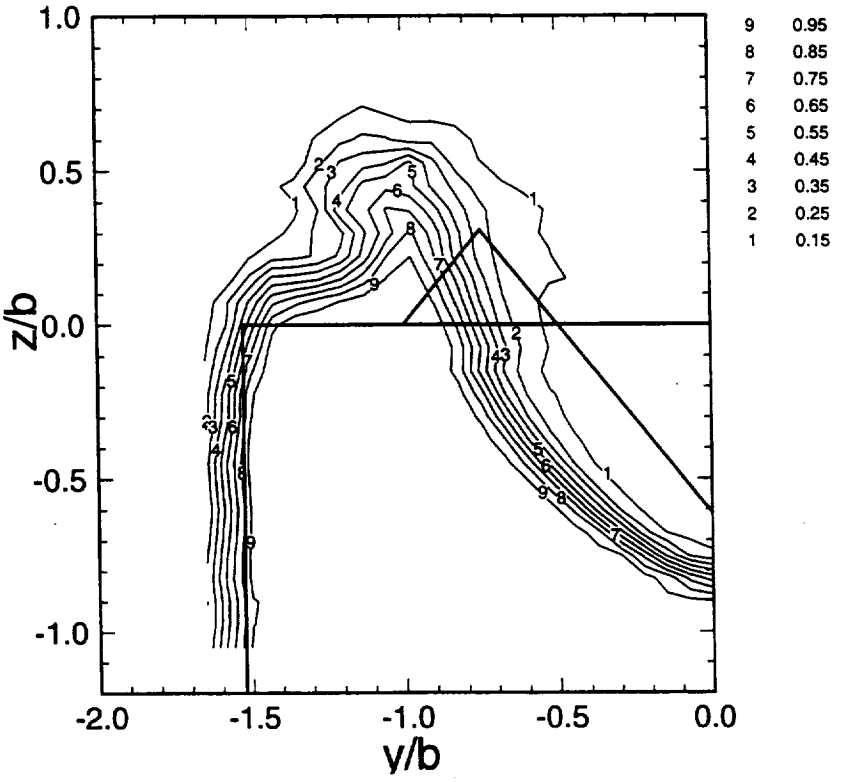

(a)

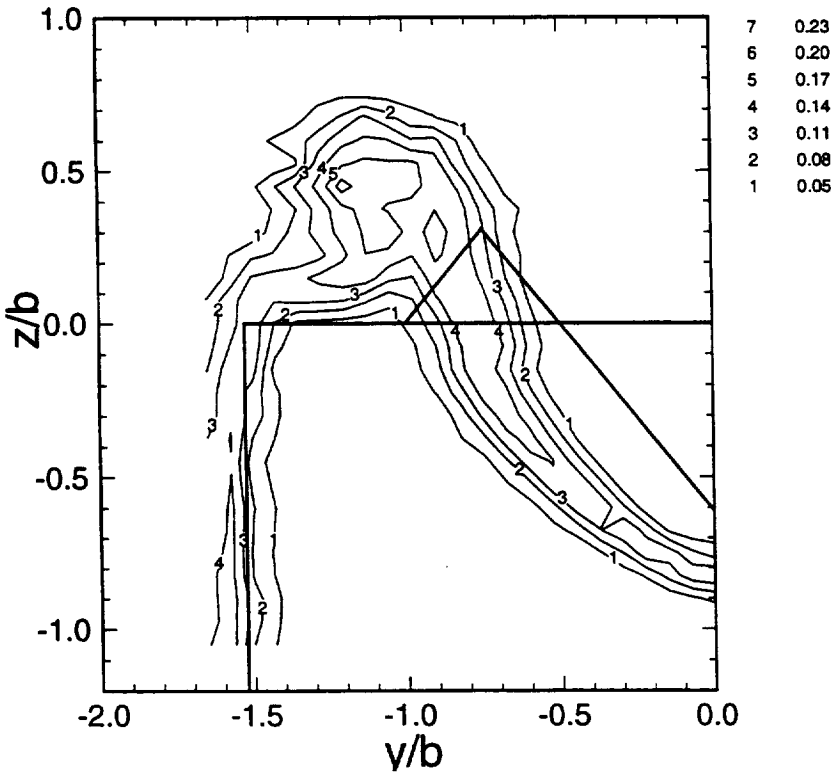

(b)

Figure 5.20: Streamwise velocity survey for modified geometry at x/b=1.2: a) $\bar{u}/U_{up}$, b) $\tilde{u}/U_{up}$.

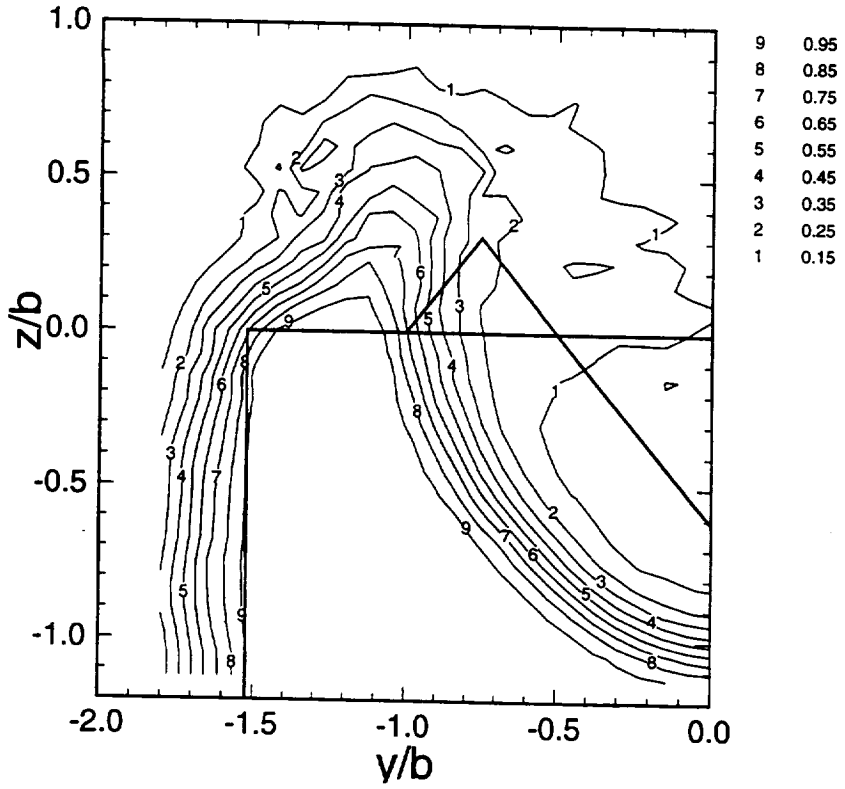

(a)

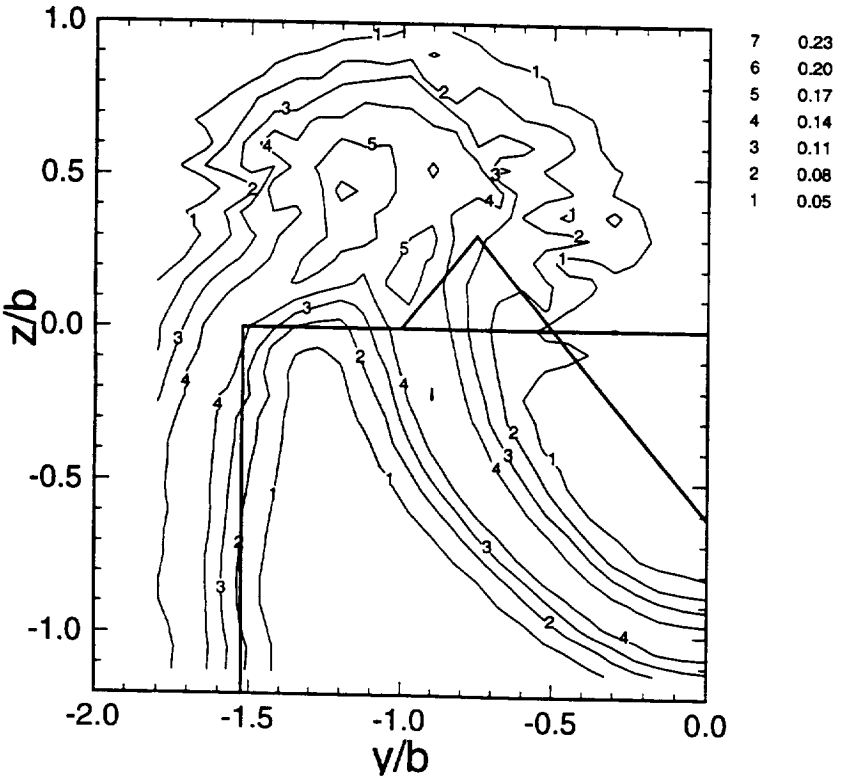

(b)

Figure 5.20: Streamwise velocity survey for modified geometry at x/b=2.0: a) $\bar{u}/U_{up}$, b) $\tilde{u}/U_{up}$.

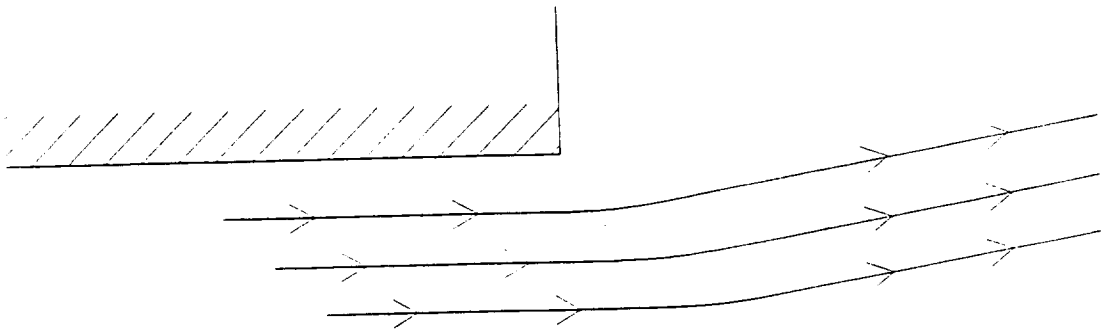

Figure 5.21: Schematic representation of streamlines for the primary tab geometry at y/b≈-1.0.

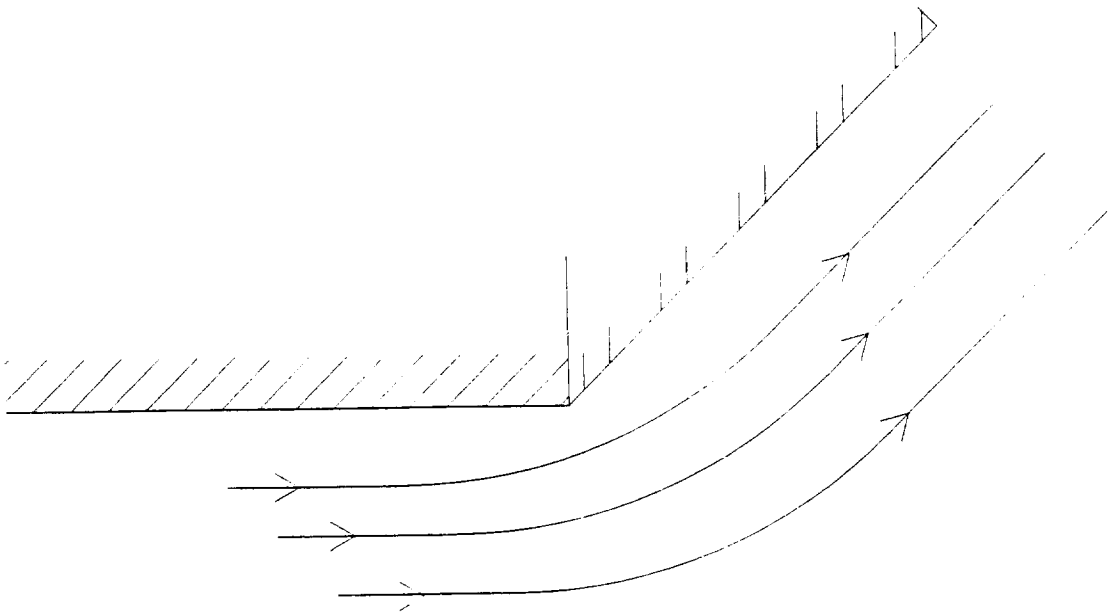

Figure 5.22: Schematic representation of streamlines for the modified tab geometry at y/b≈-1.0.

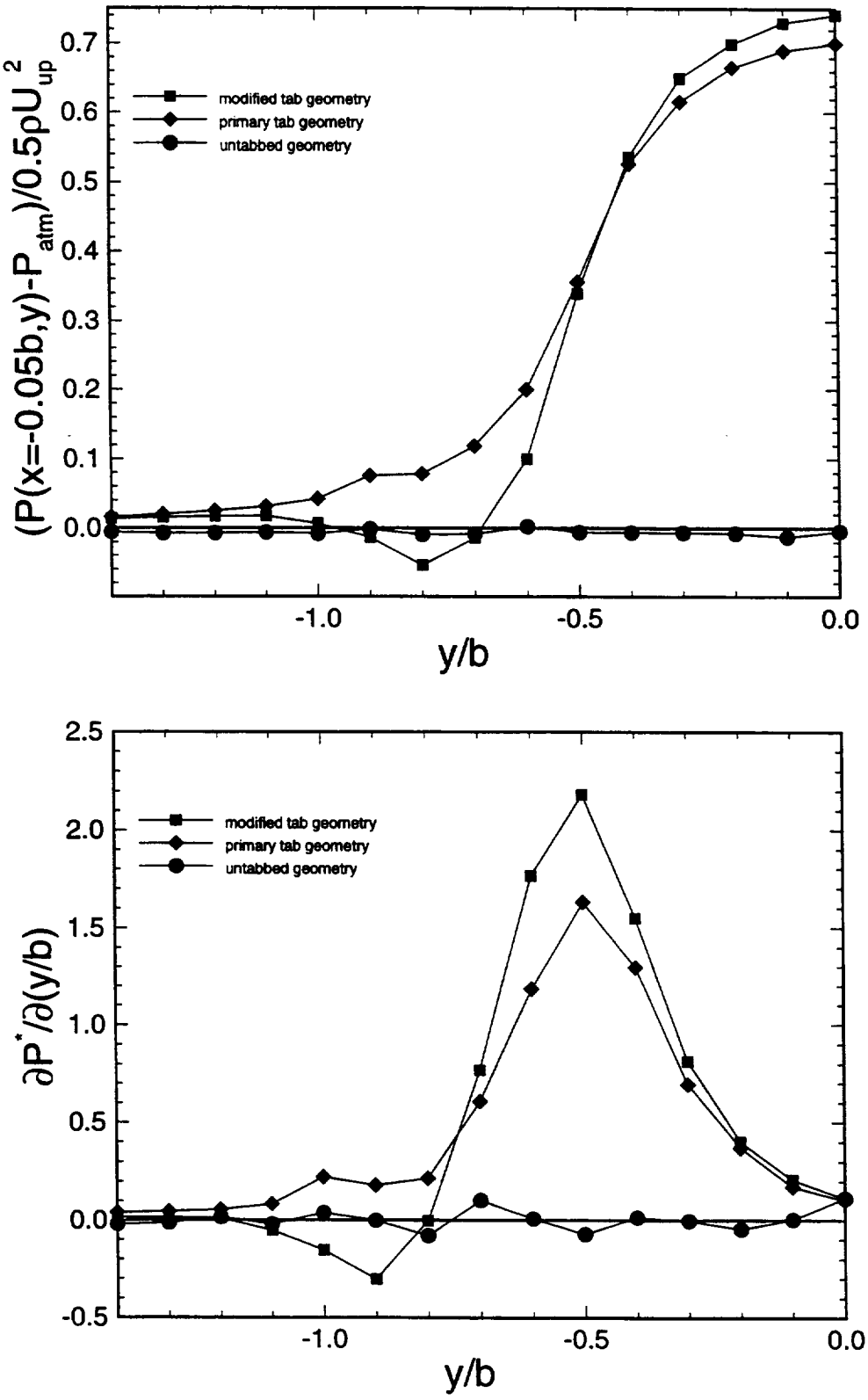

Figure 5.23: Pressure distribution for x=-0.05b: a)P*(x=-0.05,y), b)$\partial P^* / \partial ^x/_b$.

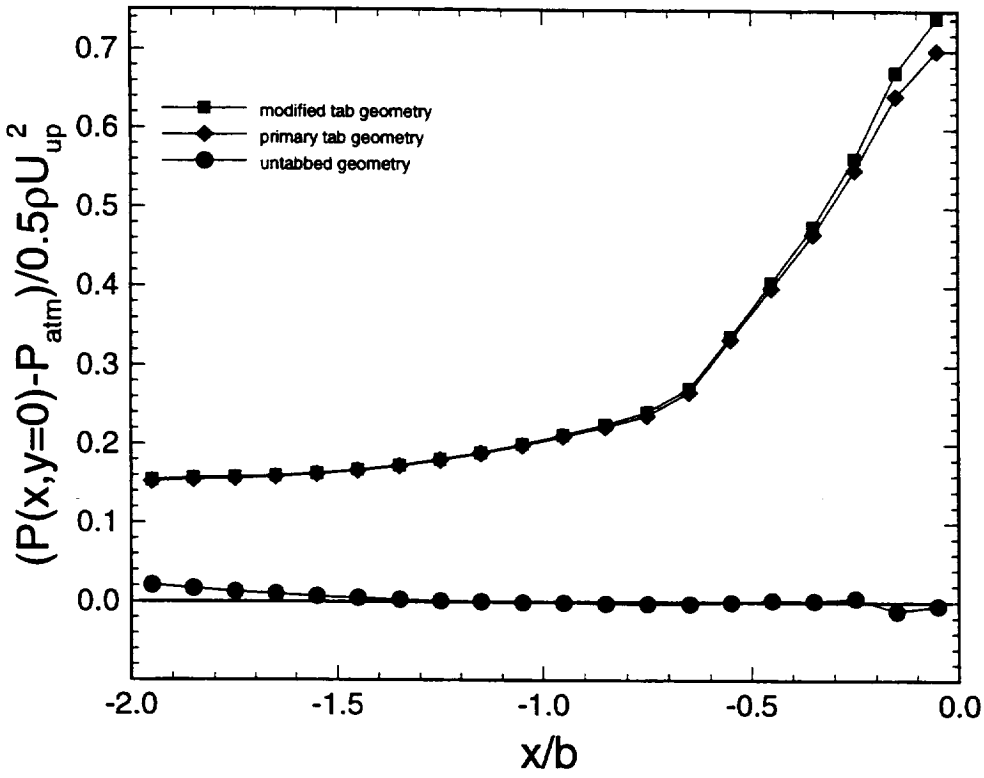

(a)

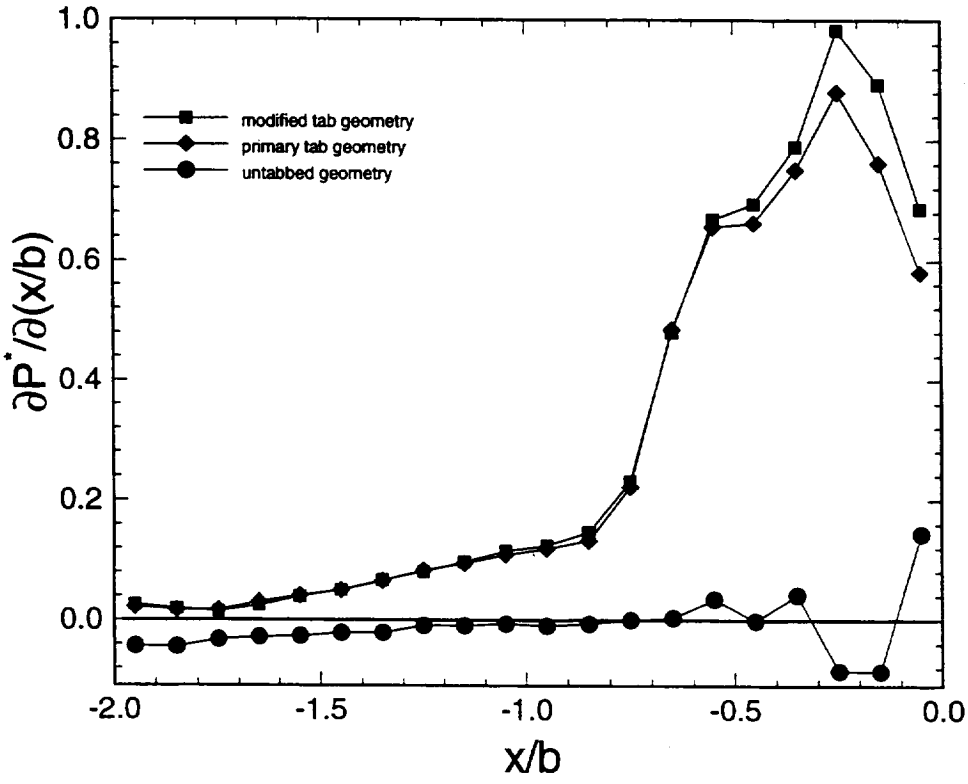

(b)

Figure 5.24: Pressure distribution for y=0: a)P*(x,y=0), b)$\partial P^*/\partial x/b$.

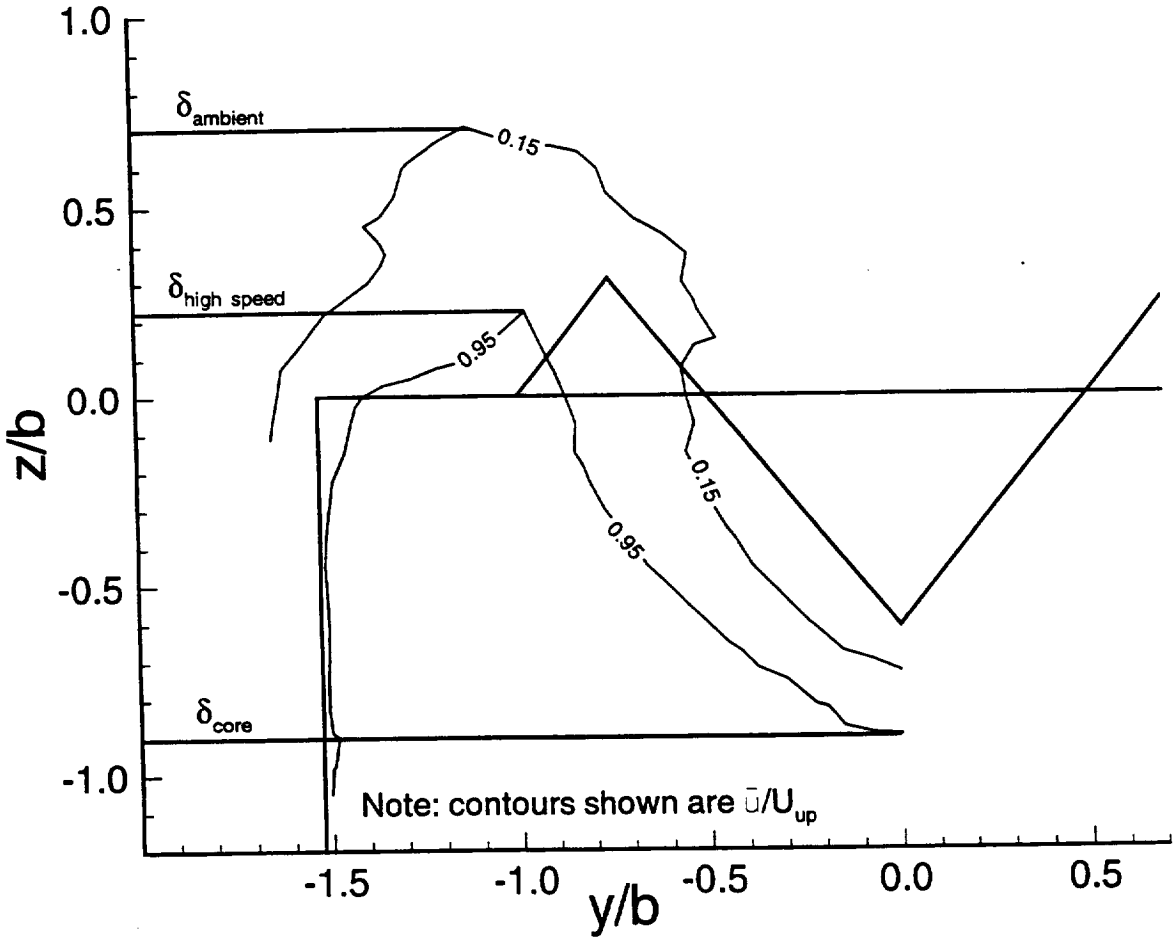

Figure 5.25: Definition of penetration measures.

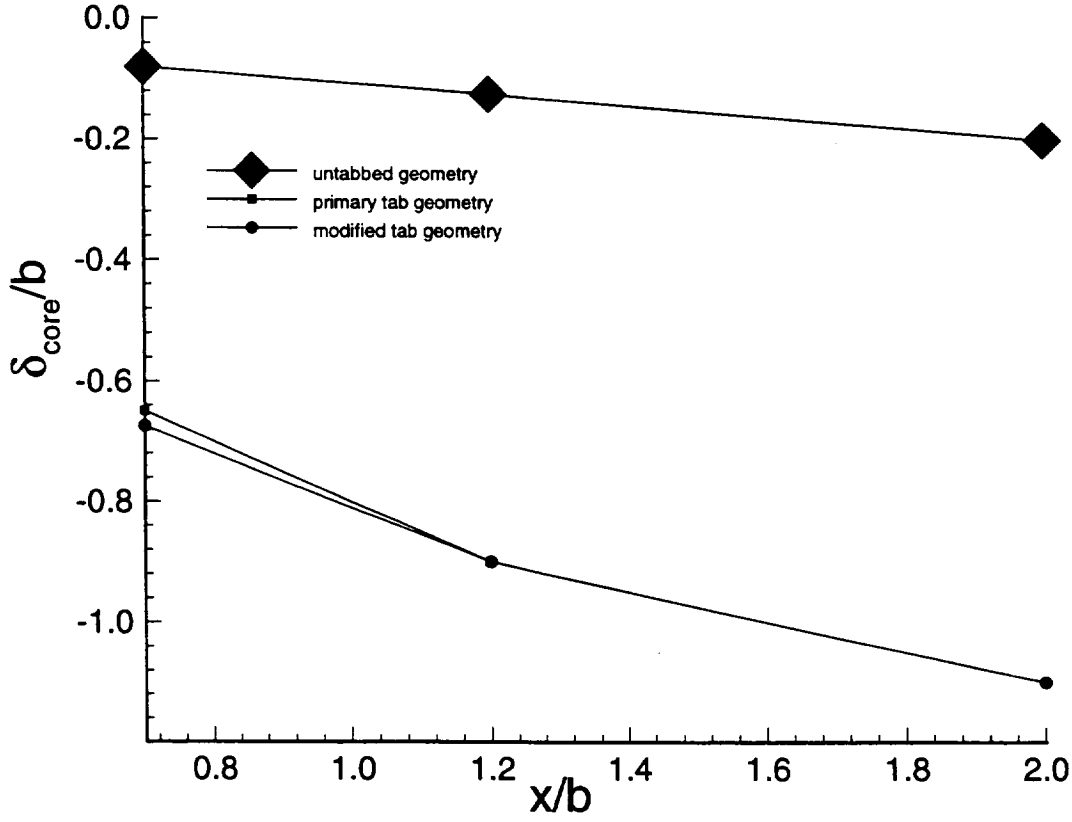

Figure 5.26: Penetration of the shear layer into the core region.

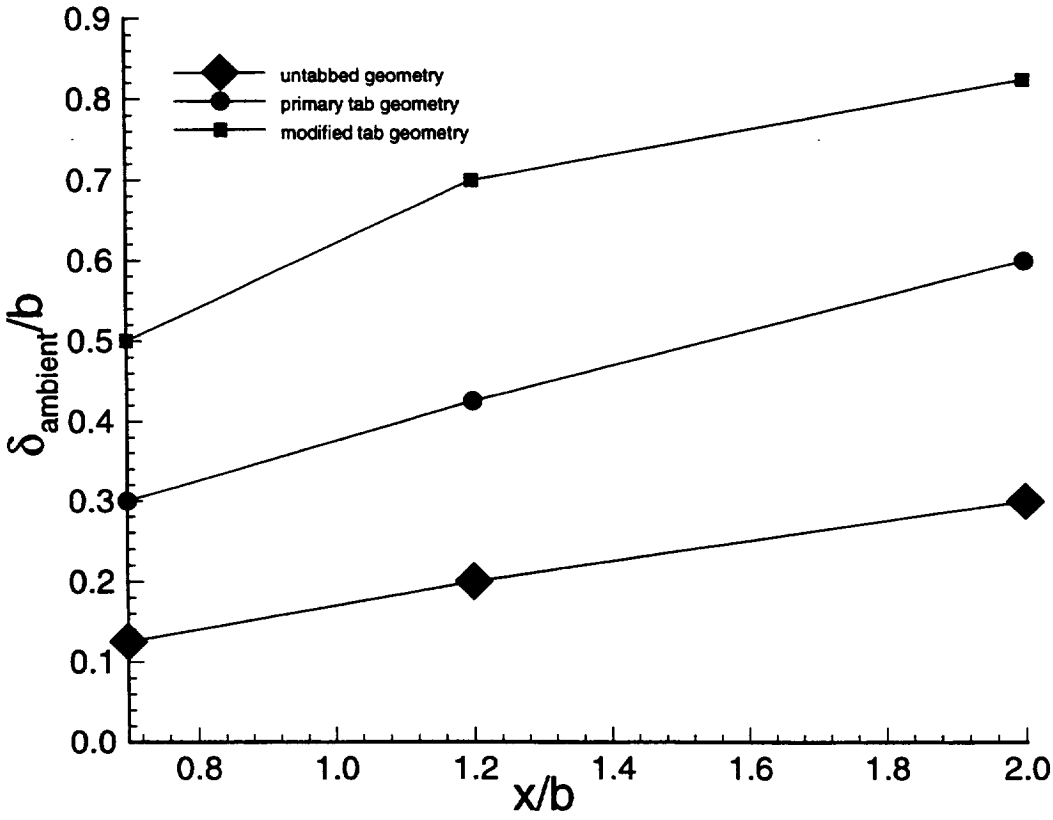

Figure 5.27: Penetration of the shear layer into the ambient region.

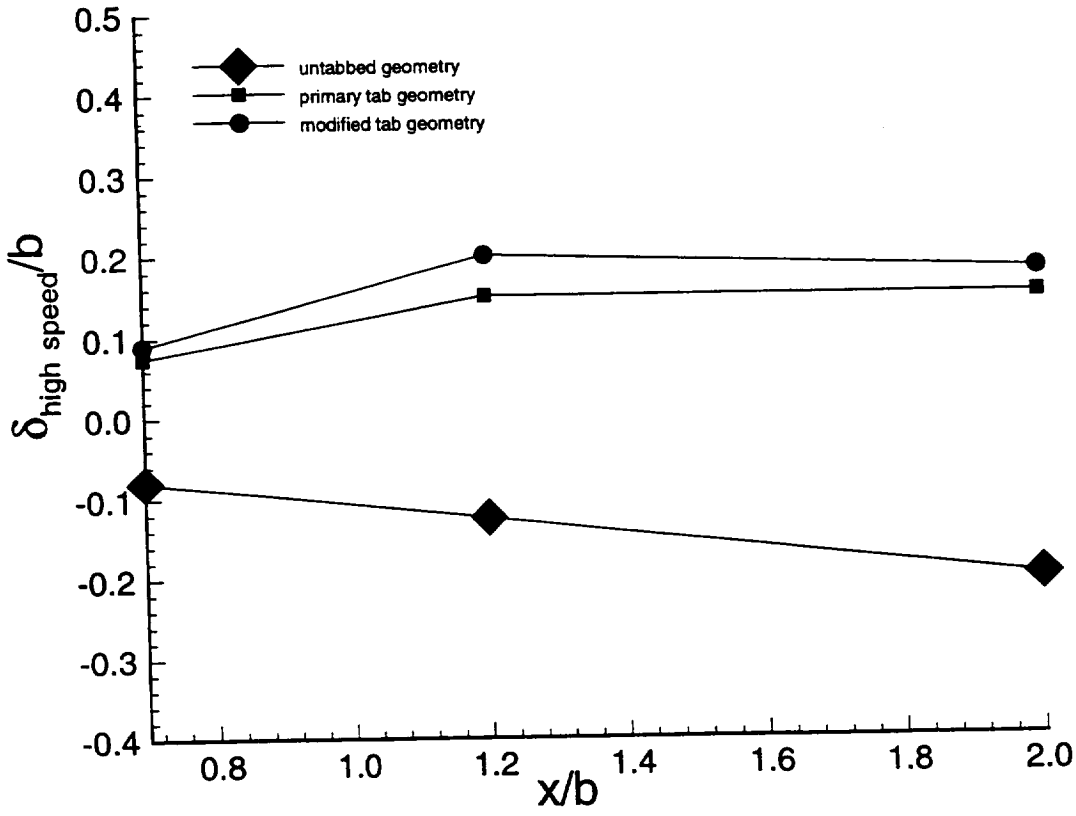

Figure 5.28: Penetration of high speed fluid into the ambient region.

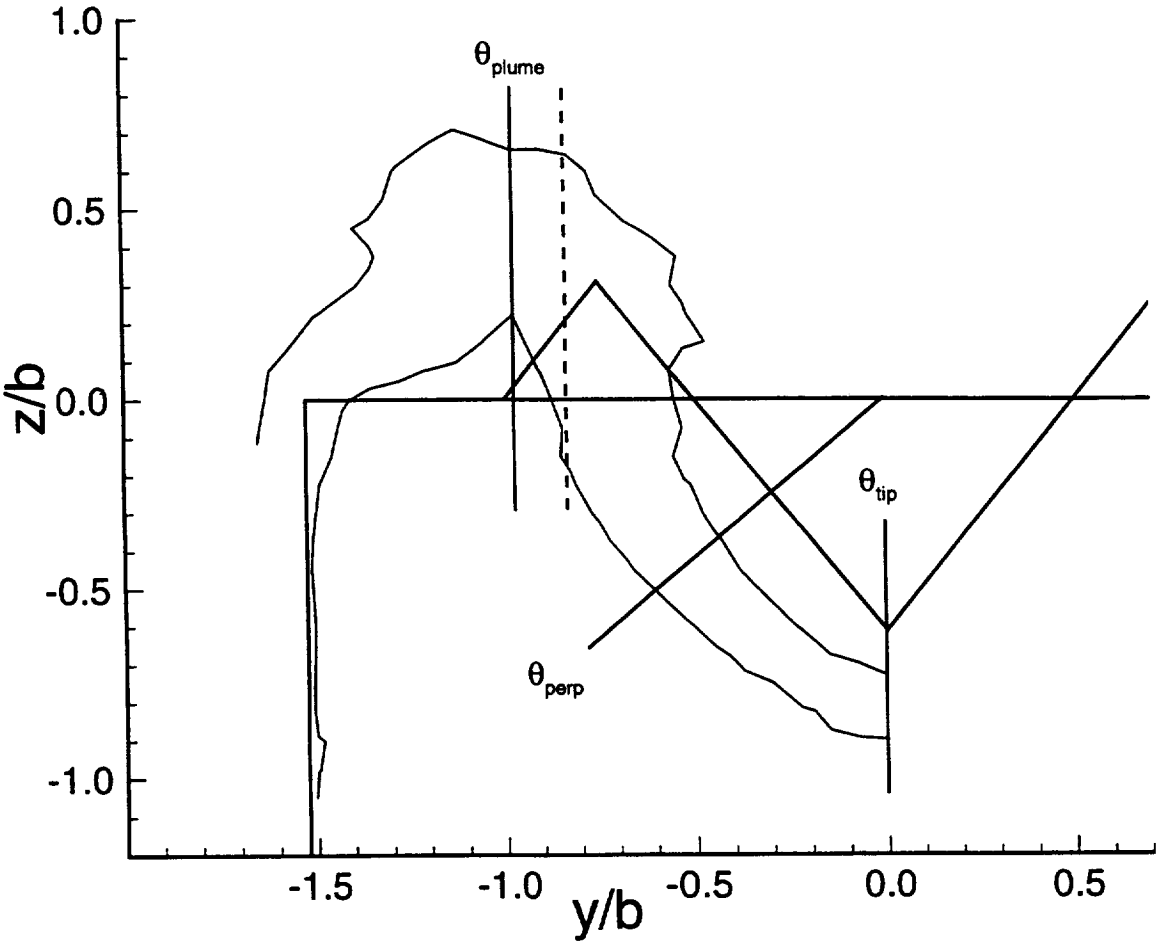

Figure 5.29: Location of shear layer momentum thickness measurements.

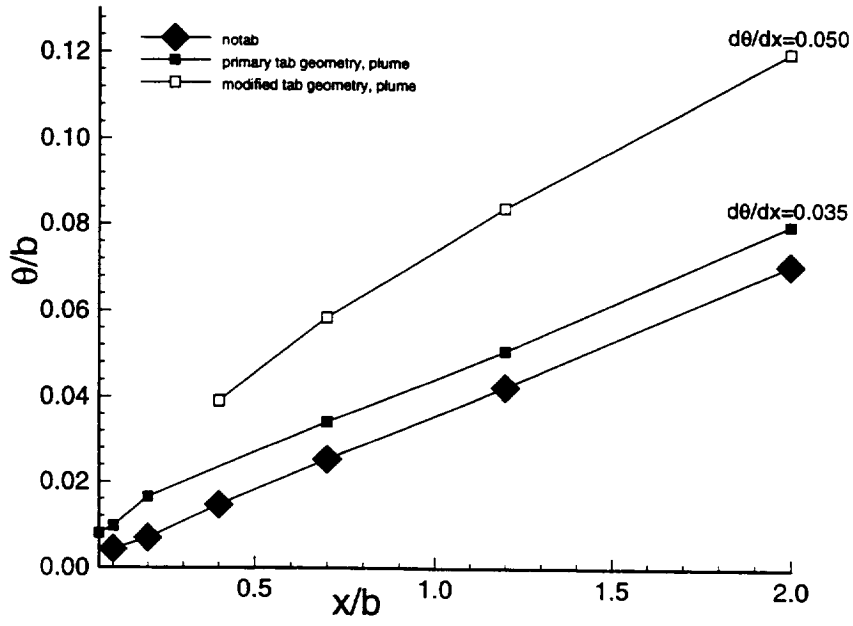

Figure 5.30: Shear layer momentum thickness,θ, for the plume.

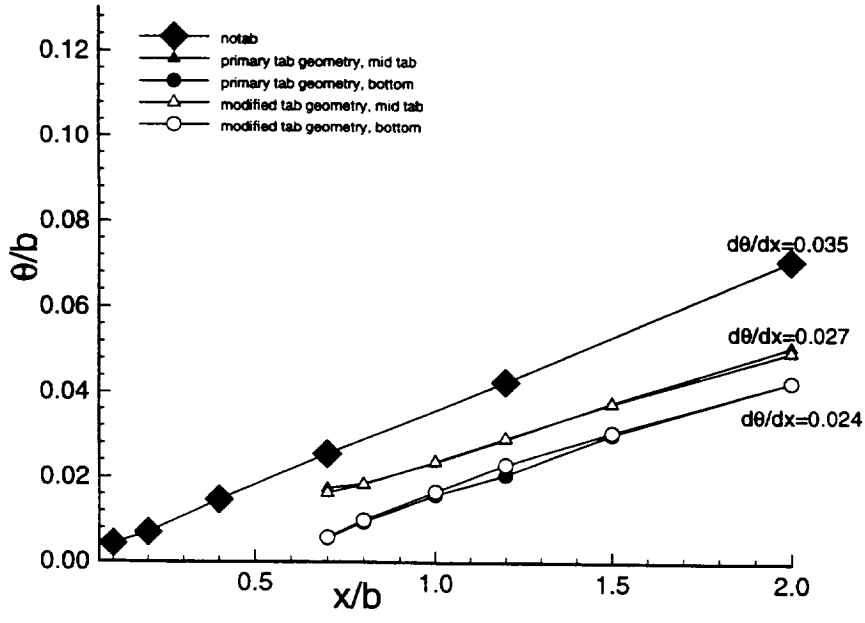

Figure 5.31: Shear layer momentum thickness,θ, for the side and tip shear layers.

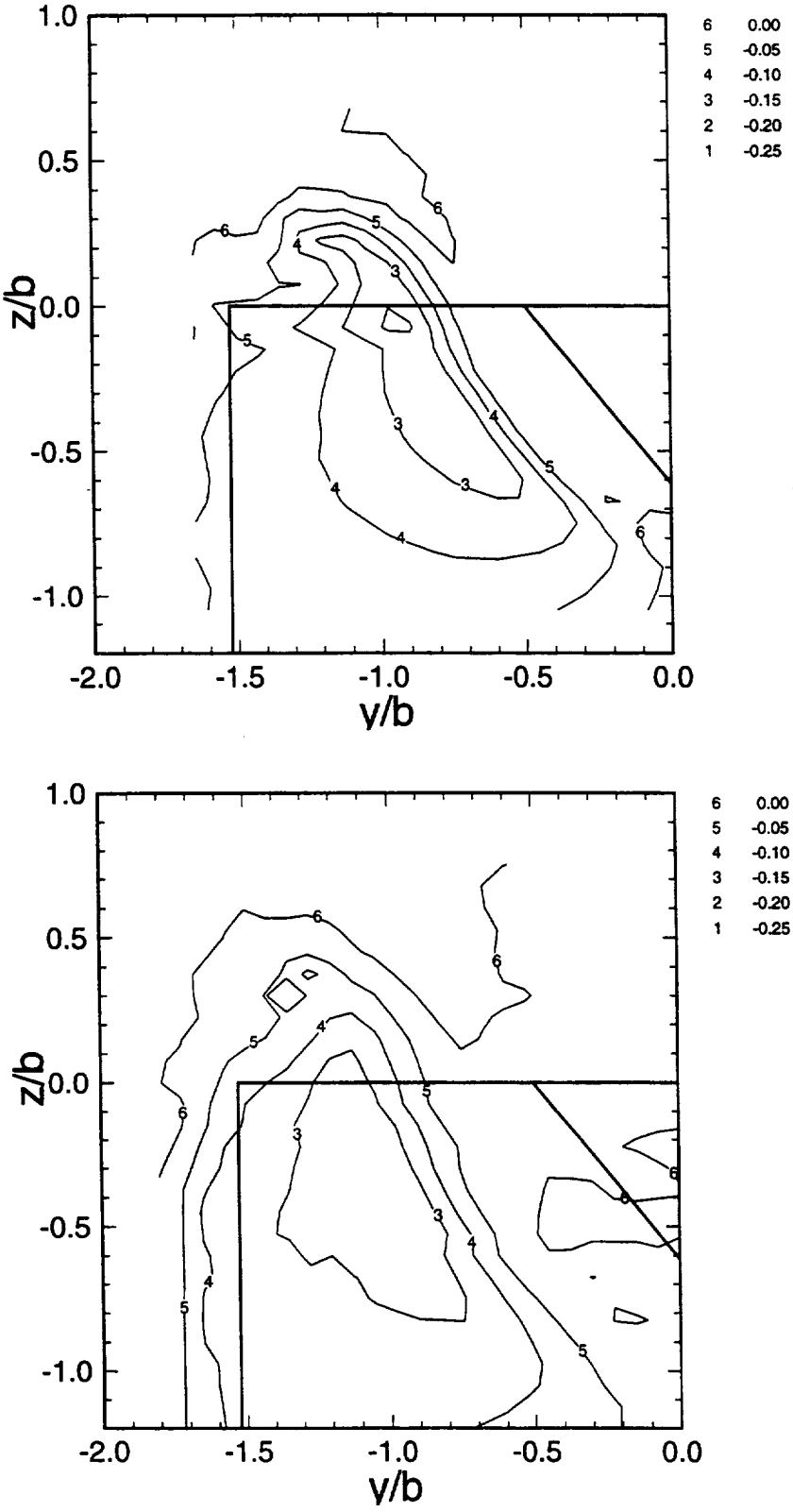

Figure 5.32: Average lateral velocity, $\overline{v}/U_{up}$, for the primary tab geometry: a)1.2, b)2.0.

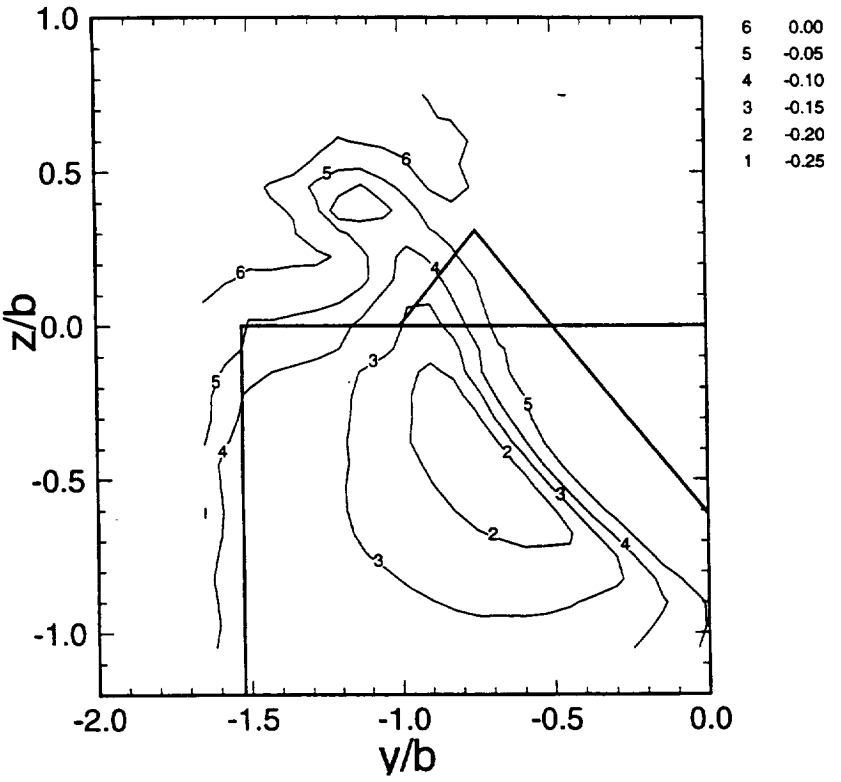

(a)

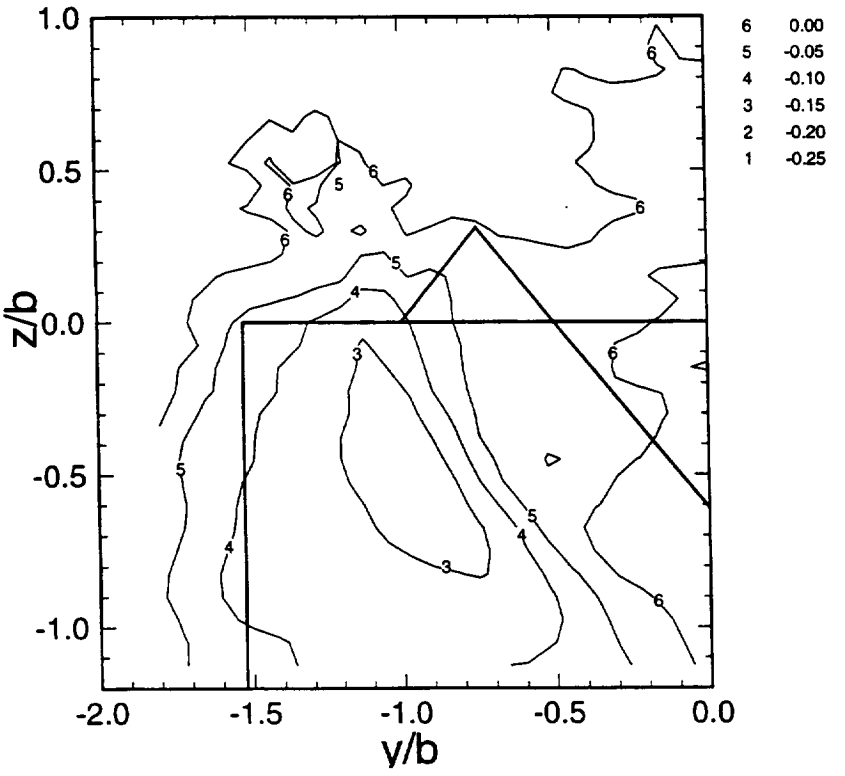

(b)

Figure 5.33: Average lateral velocity, $\overline{v}/U_{up}$, for the modified tab geometry: a)1.2, b)2.0.

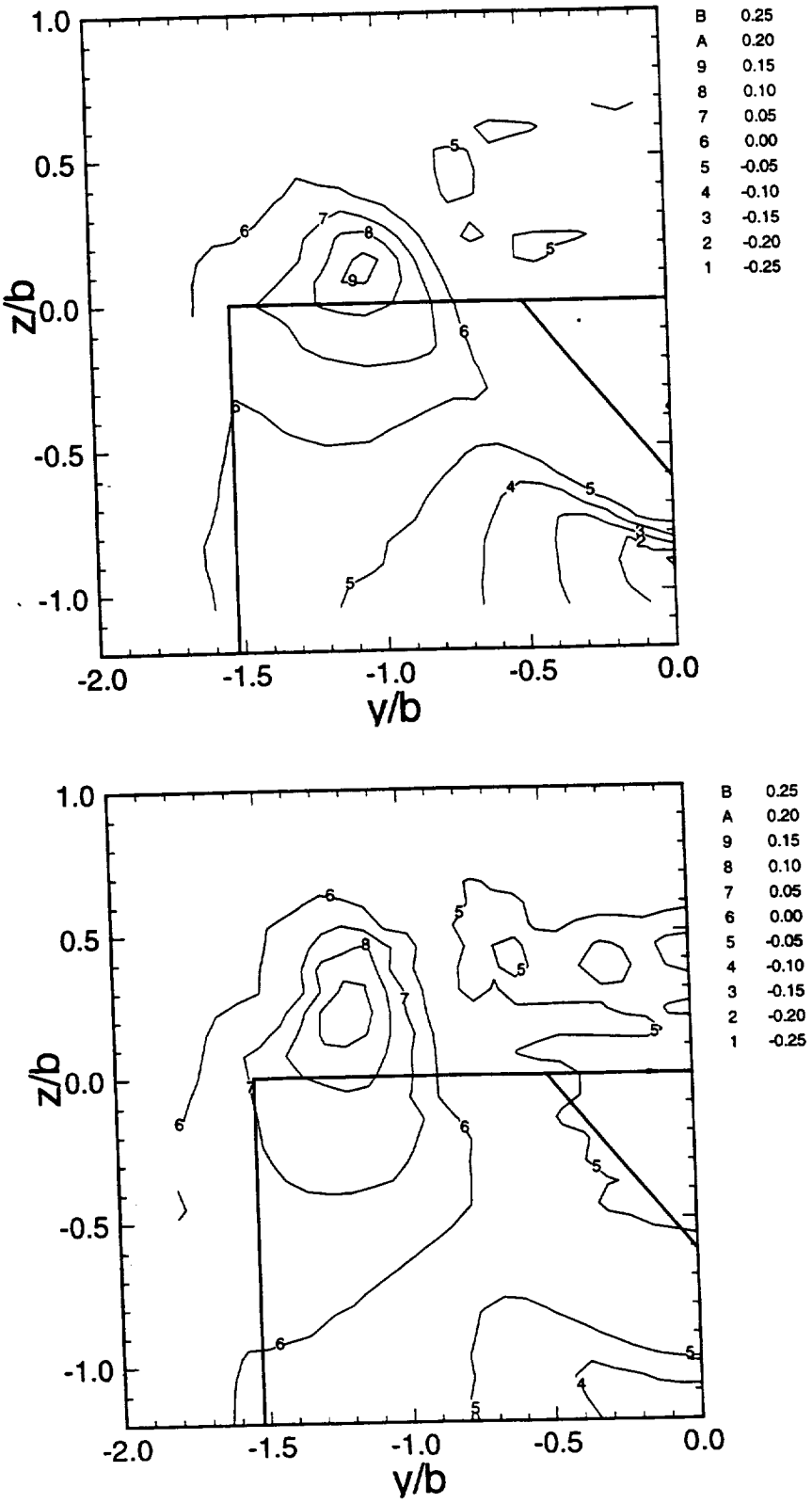

Figure 5.34: Average transverse velocity, $\overline{w}/U_{up}$, for the primary tab geometry: a)1.2, b)2.0.

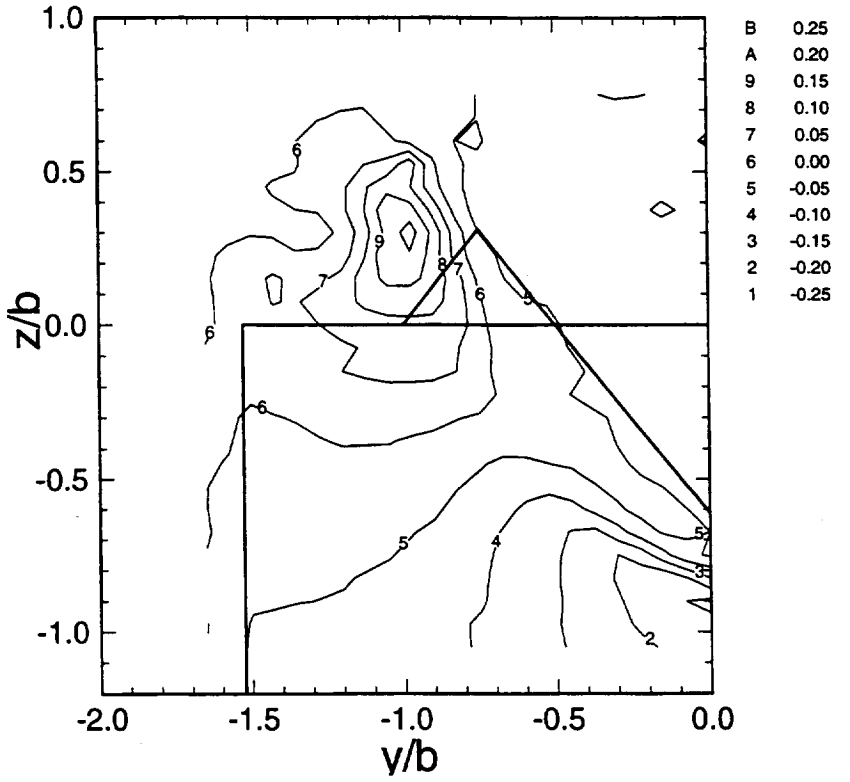

(a)

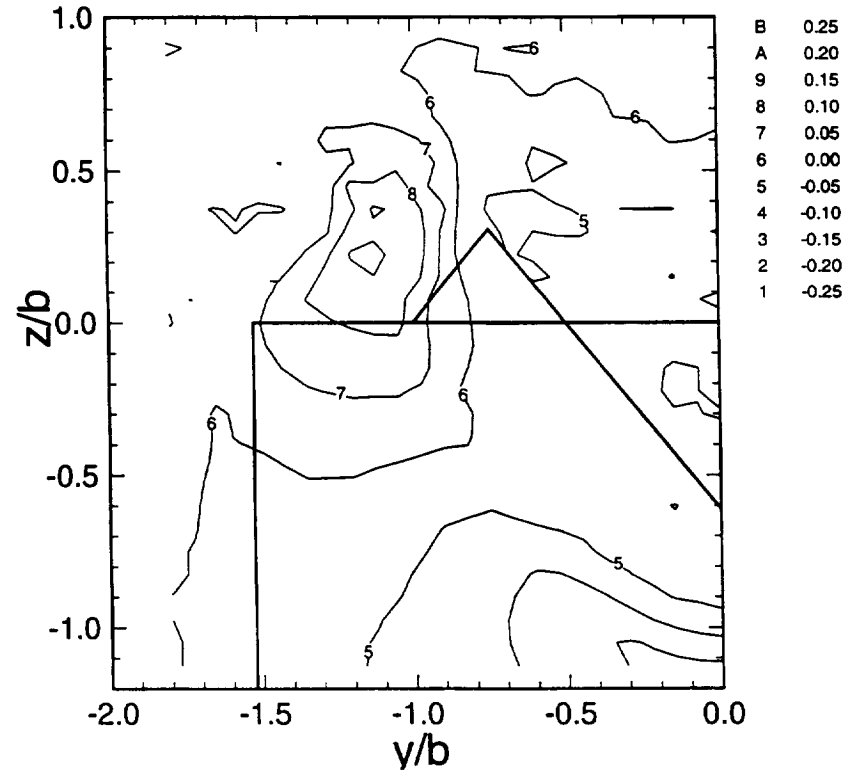

(b)

Figure 5.35: Average transverse velocity, $\overline{w}/ U_{up}$, for the modified tab geometry: a)1.2, b)2.0.

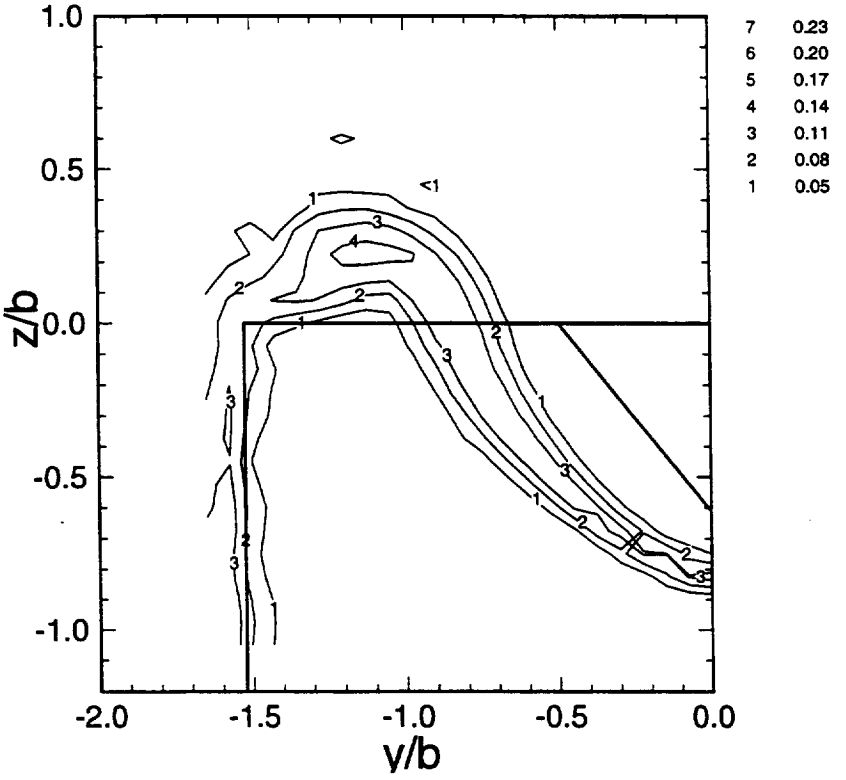

(a)

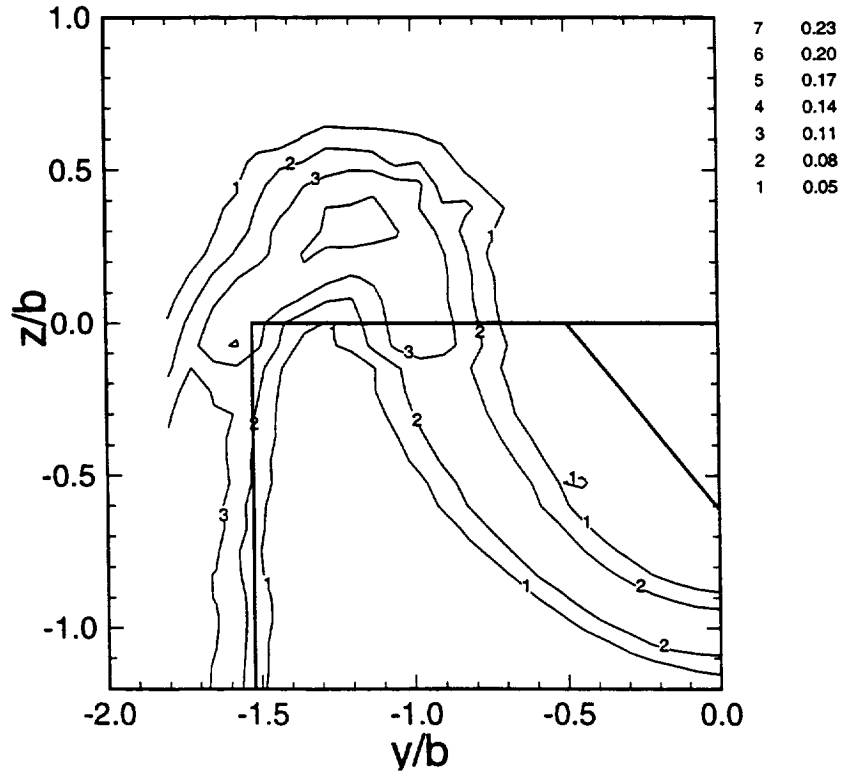

(b)

Figure 5.36: Fluctuating lateral velocity, $\tilde{v}/U_{up}$, for the primary tab geometry: a)1.2, b)2.0.

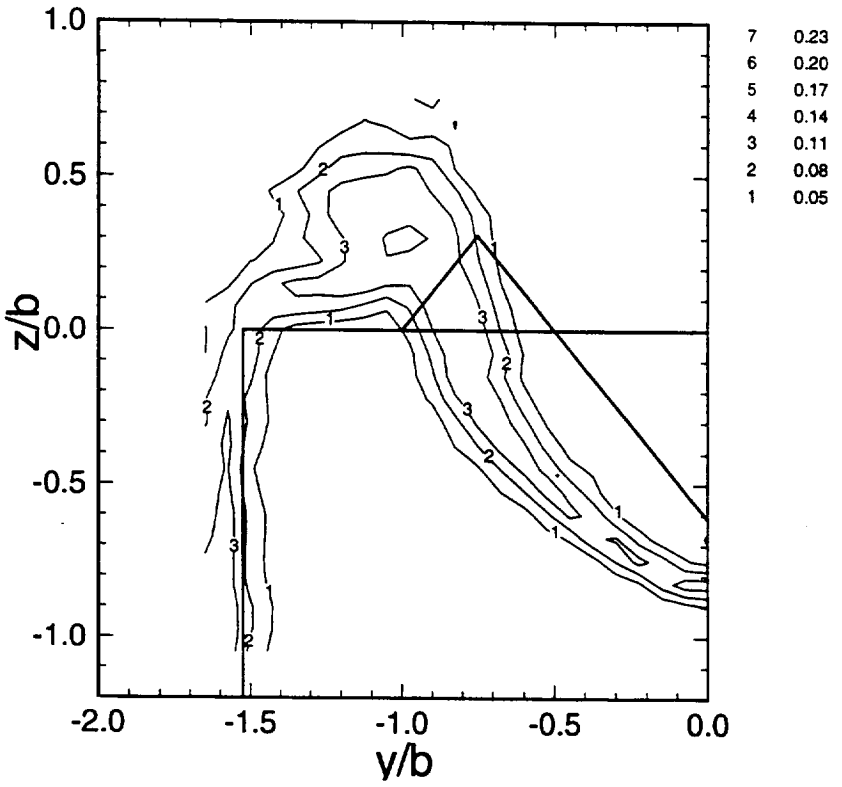

(a)

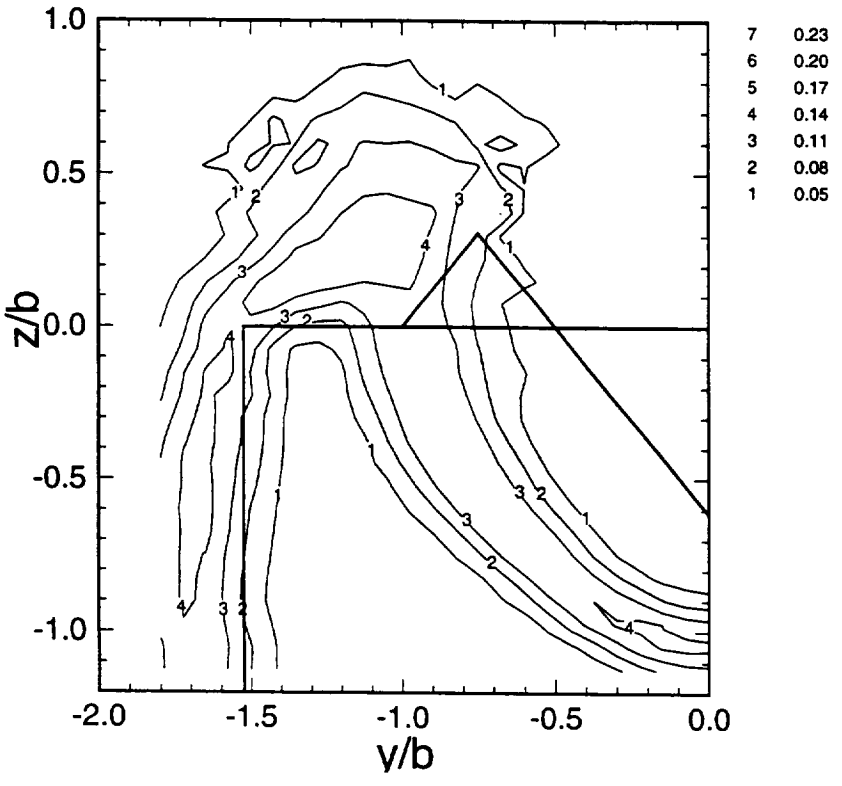

(b)

Figure 5.37: Fluctuating lateral velocity, $\tilde{v}/U_{up}$, for the modified tab geometry: a)1.2, b)2.0.

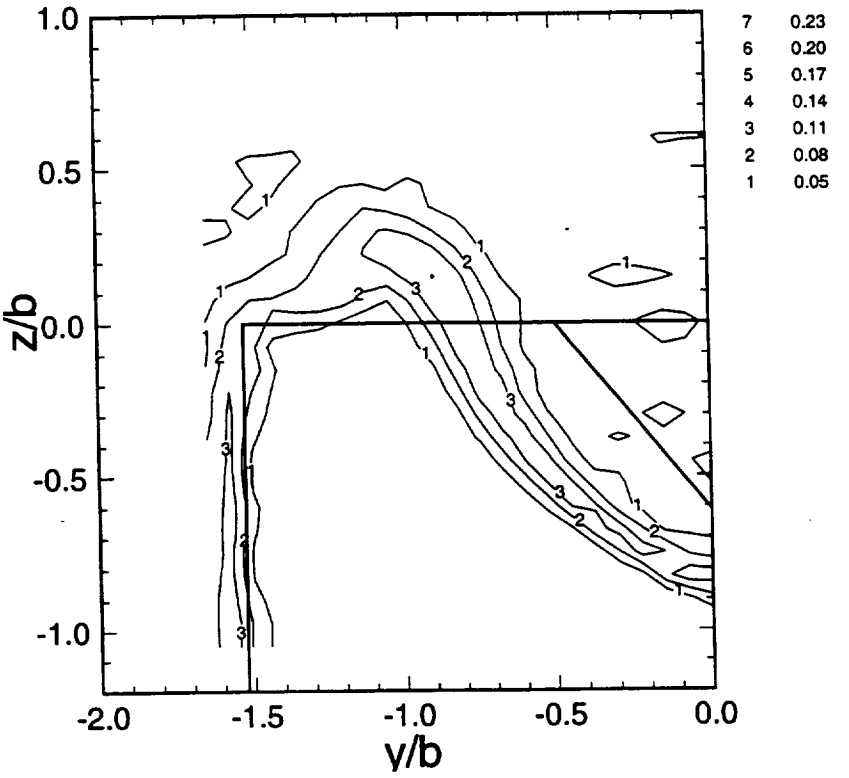

(a)

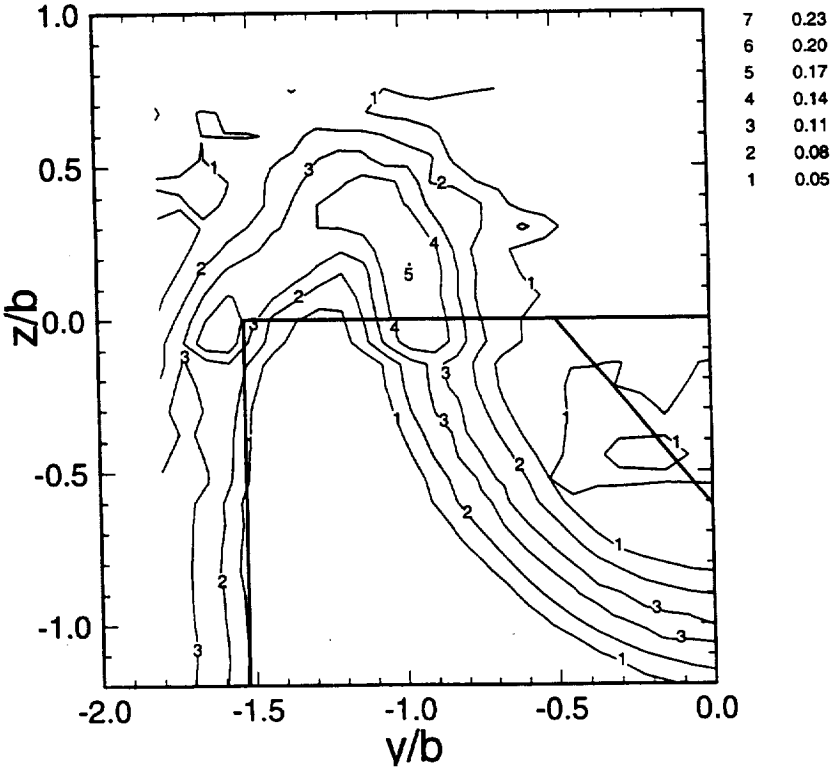

(b)

Figure 5.38: Fluctuating lateral velocity, $\tilde{w}/U_{up}$, for the primary tab geometry: a)1.2, b)2.0.

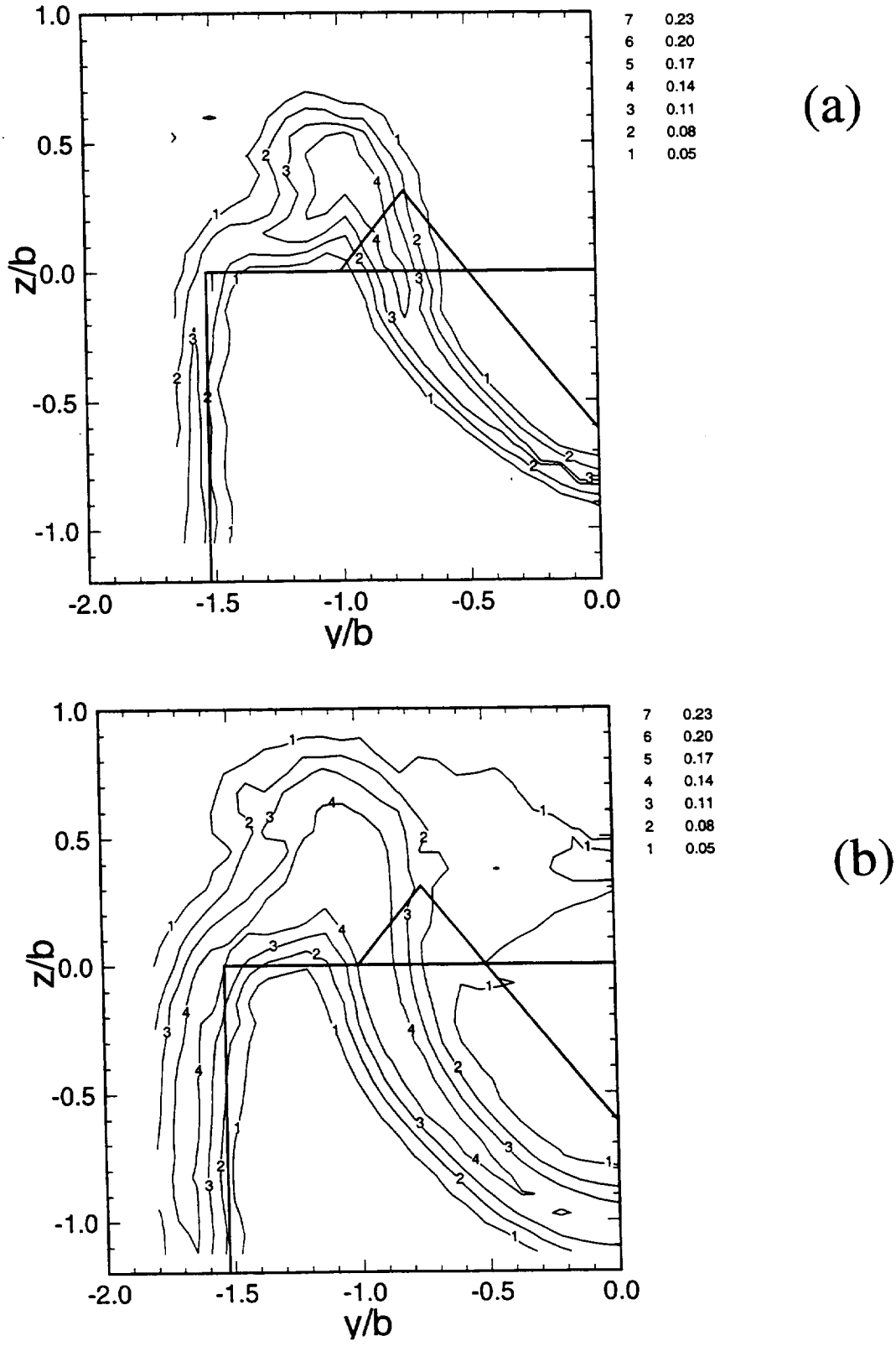

Figure 5.39: Fluctuating transverse velocity, $\tilde{w}/U_{up}$, for the modified tab geometry: a)1.2, b)2.0.

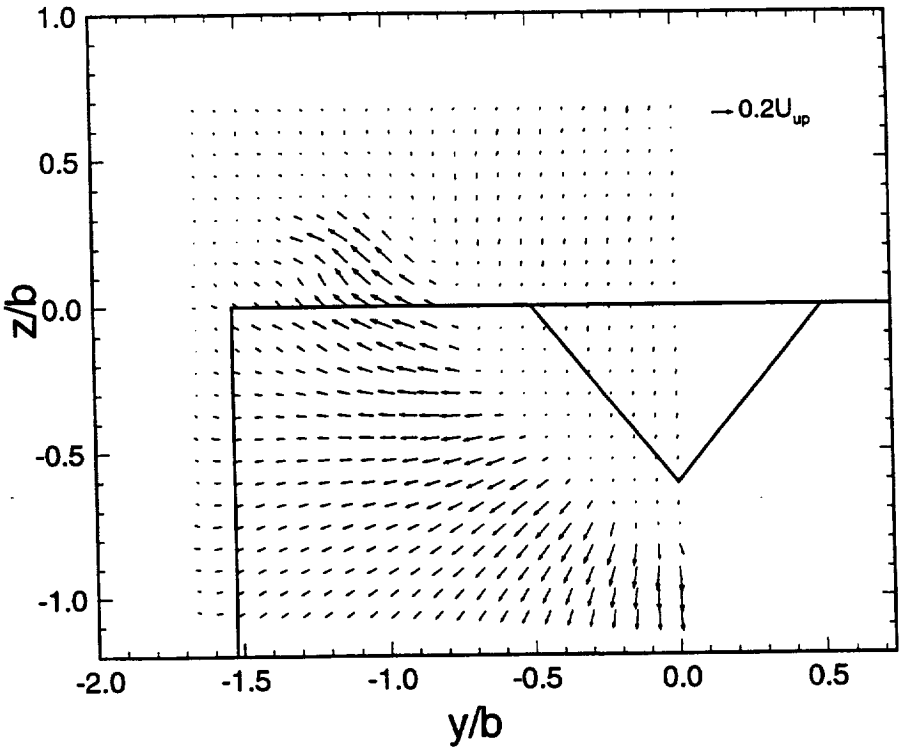

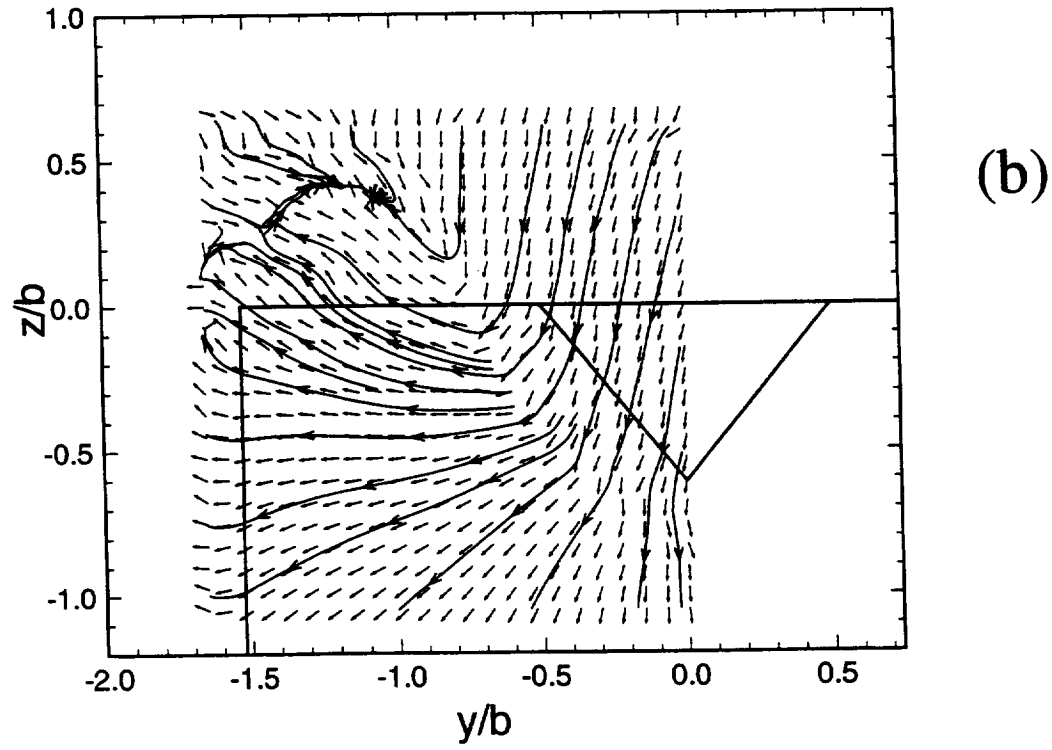

Figure 5.40: vw vector plot for the primary tab geometry at x/b=1.2: a) scaled, b) unscaled, c) $\overline{v} = 0$, $\overline{w} = 0$ intercepts d) singular points.

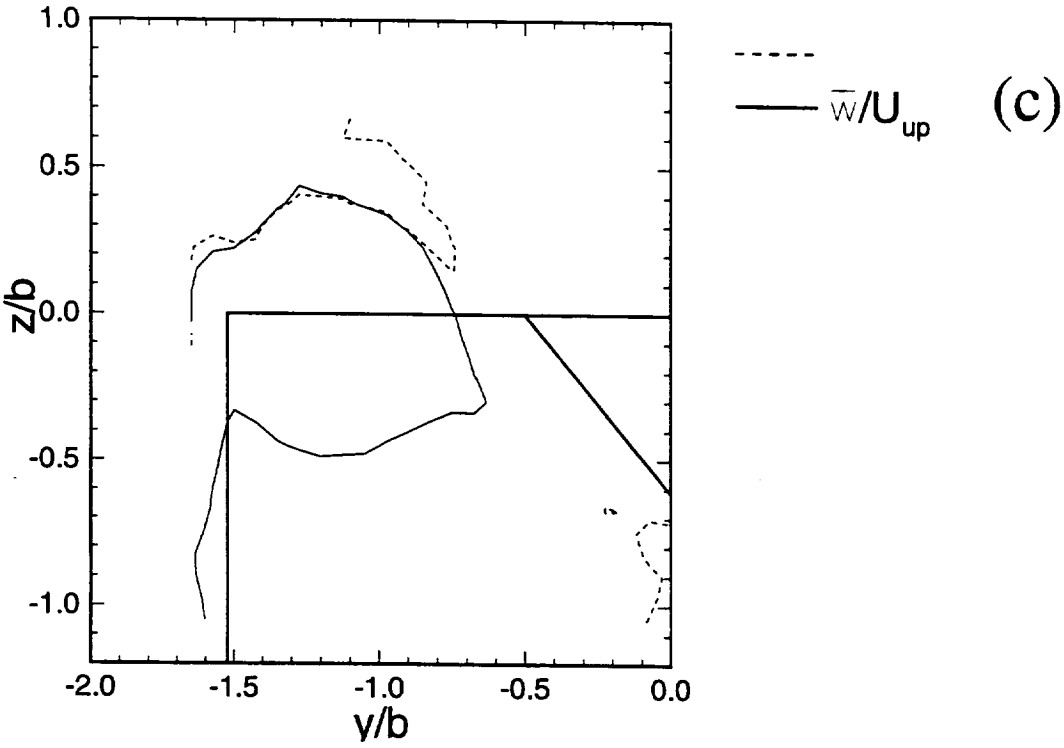

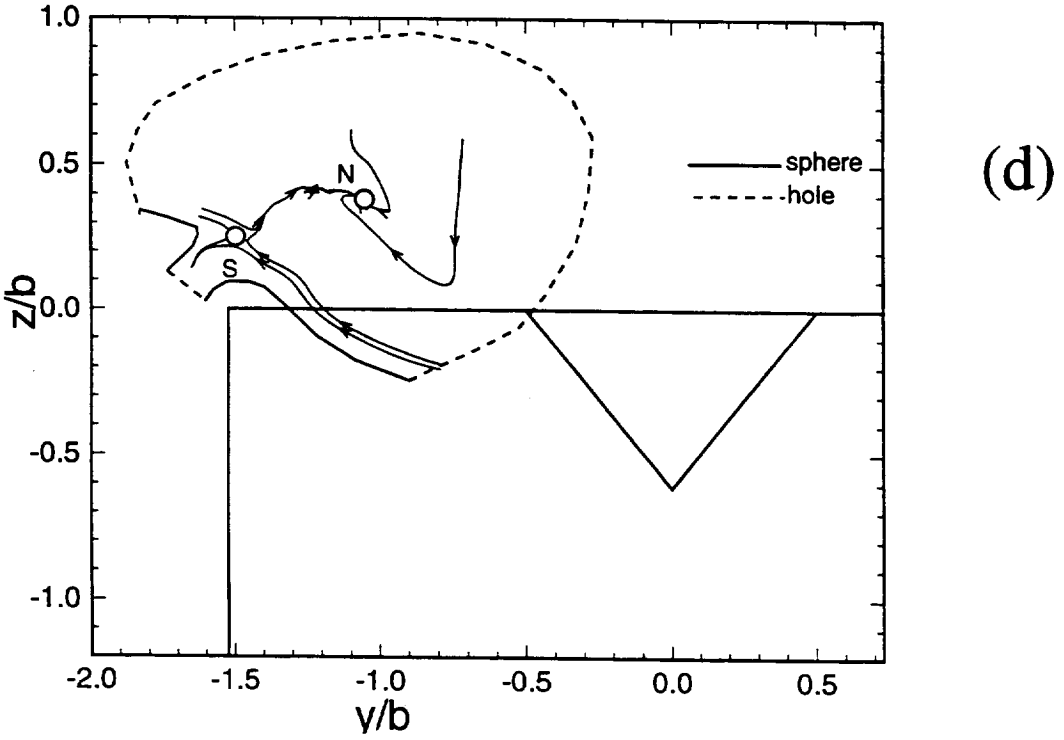

Figure 5.40: (continued)

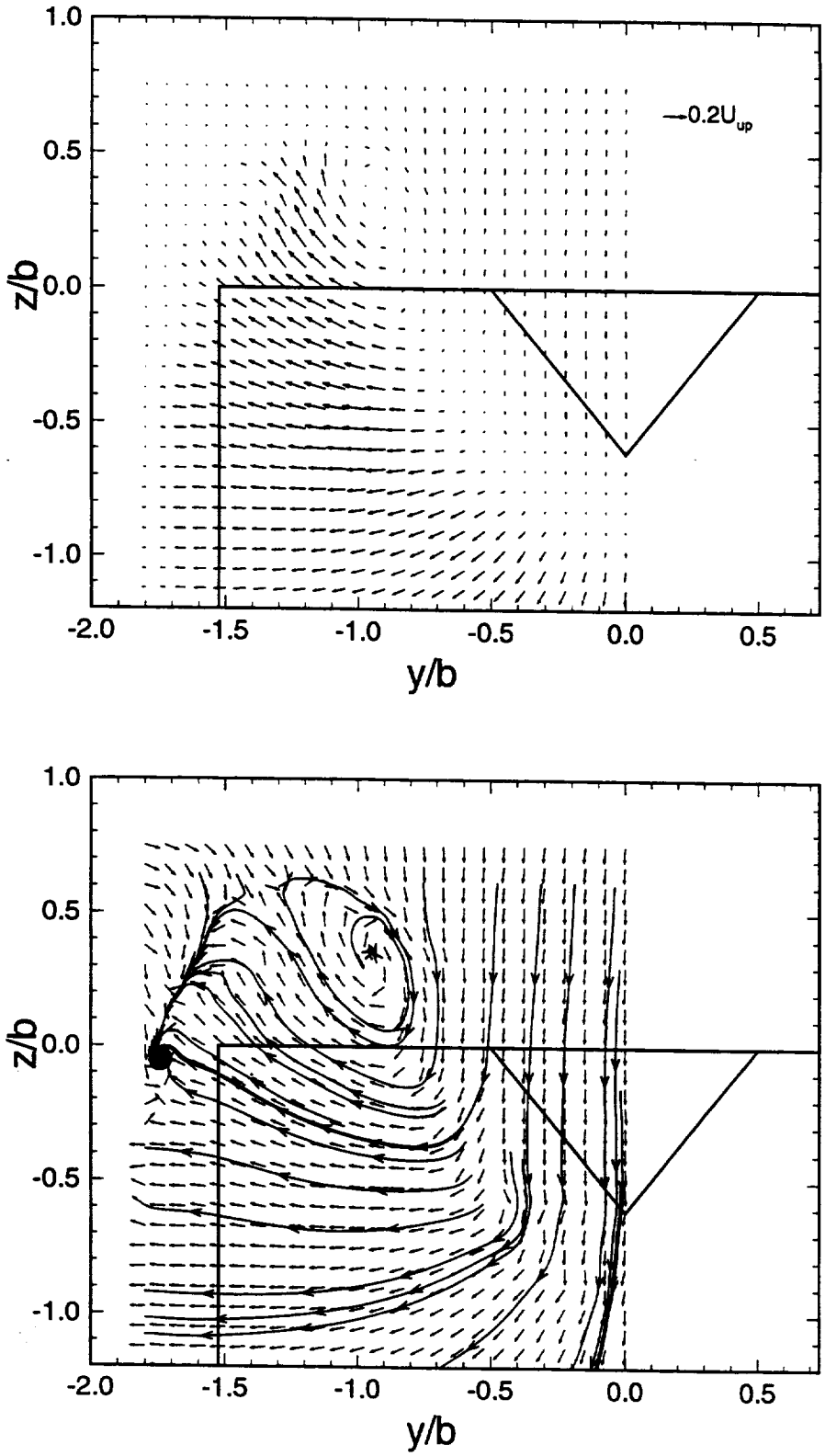

Figure 5.41: vw vector plot for the primary tab geometry at x/b=2.0: a) scaled, b) unscaled, c) $\overline{v} = 0$, $\overline{w} = 0$ intercepts d) singular points.

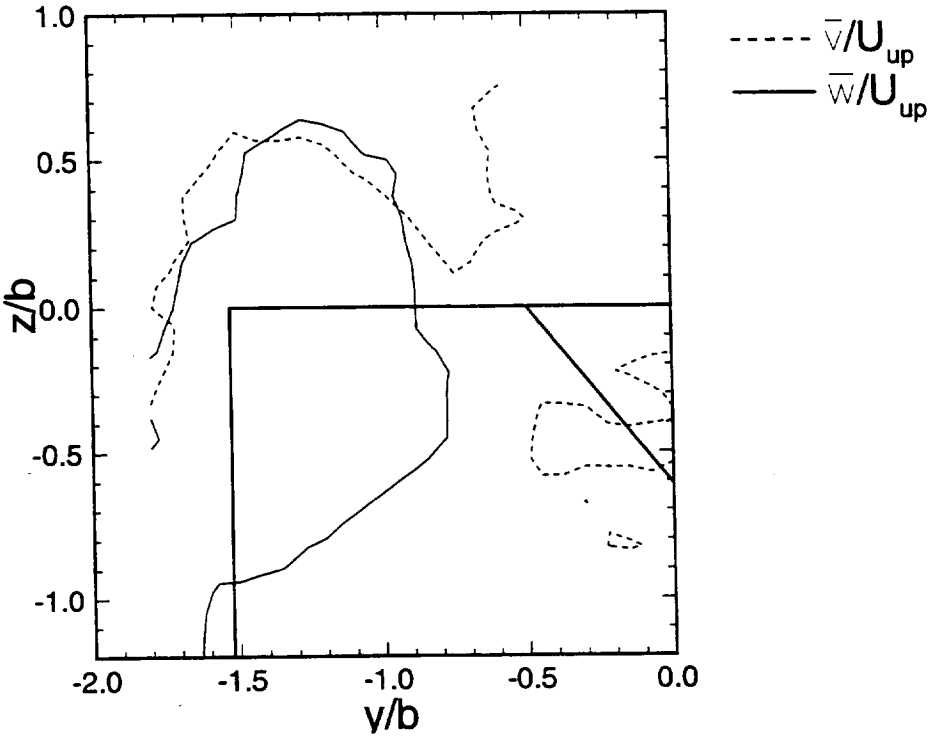

(c)

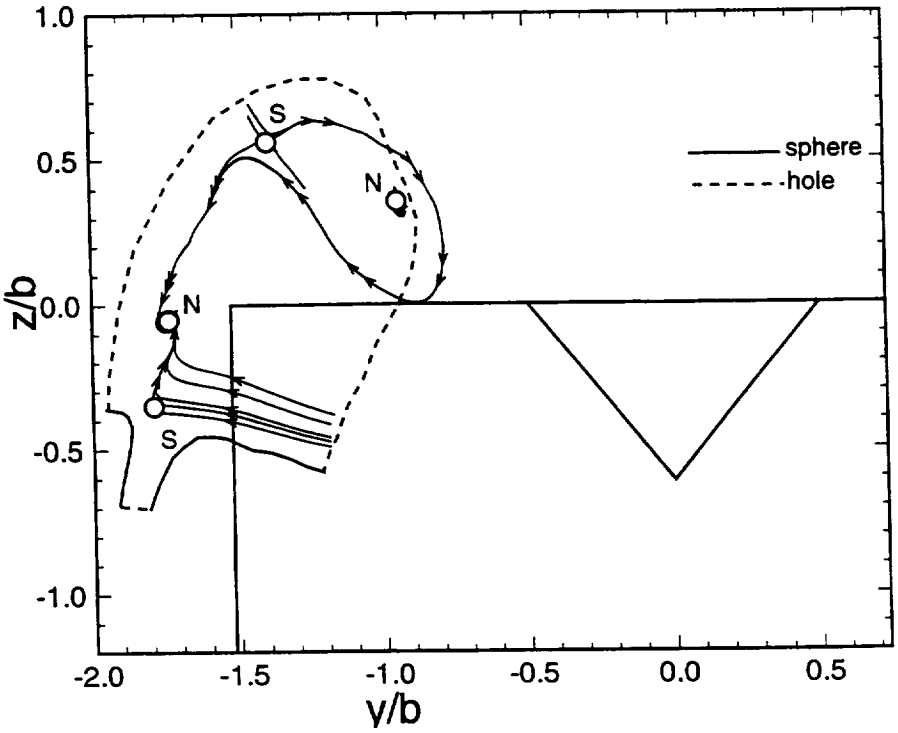

(d)

Figure 5.41: (continued)

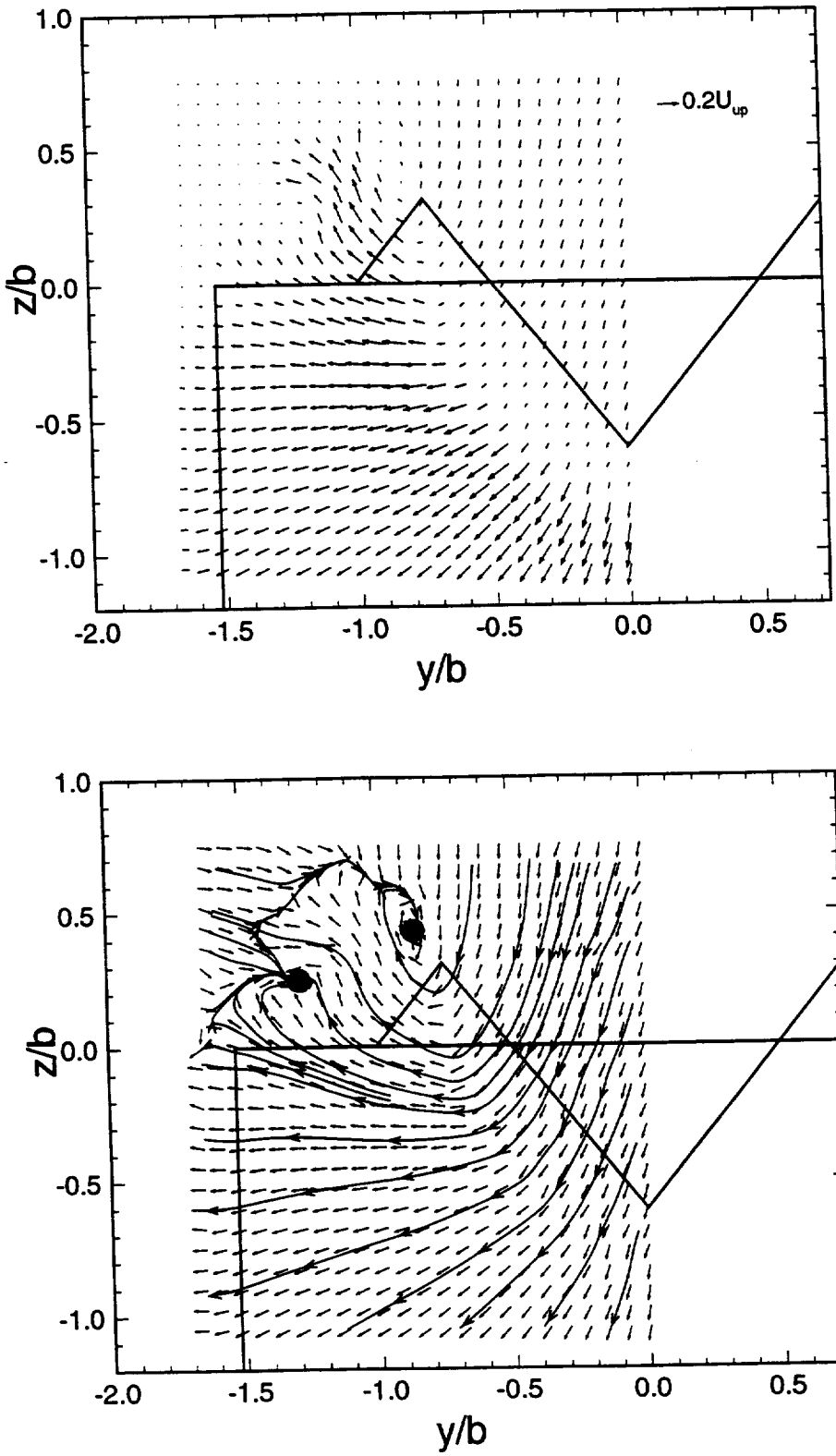

Figure 5.42: vw vector plot for the modified tab geometry at x/b=1.2: a) scaled, b) unscaled, c) $\overline{v} = 0$, $\overline{w} = 0$ intercepts d) singular points.

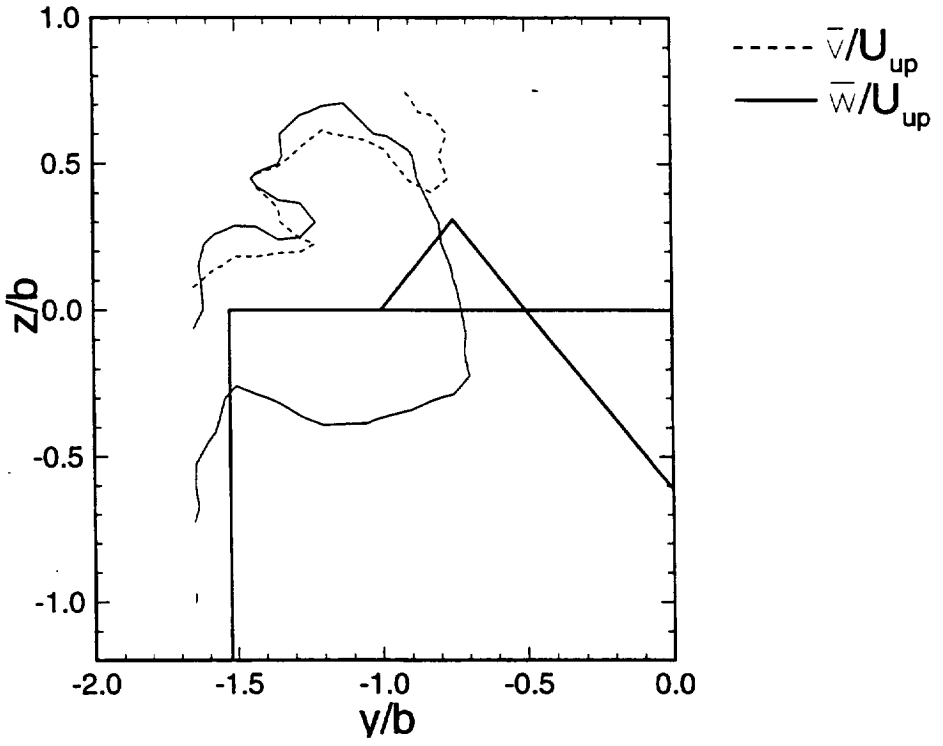

(c)

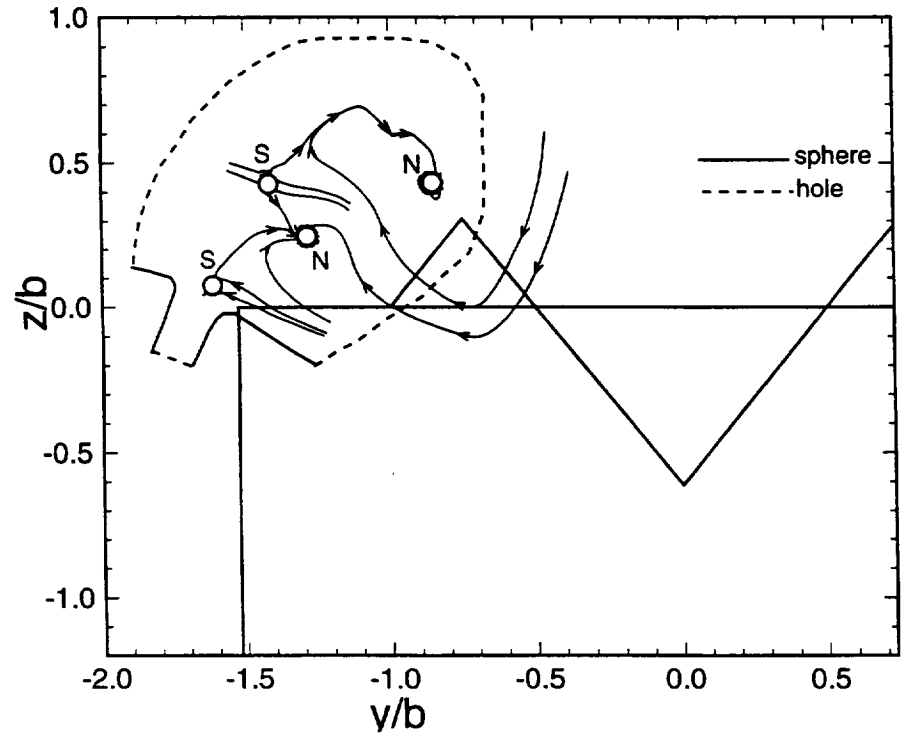

(d)

Figure 5.42: (continued)

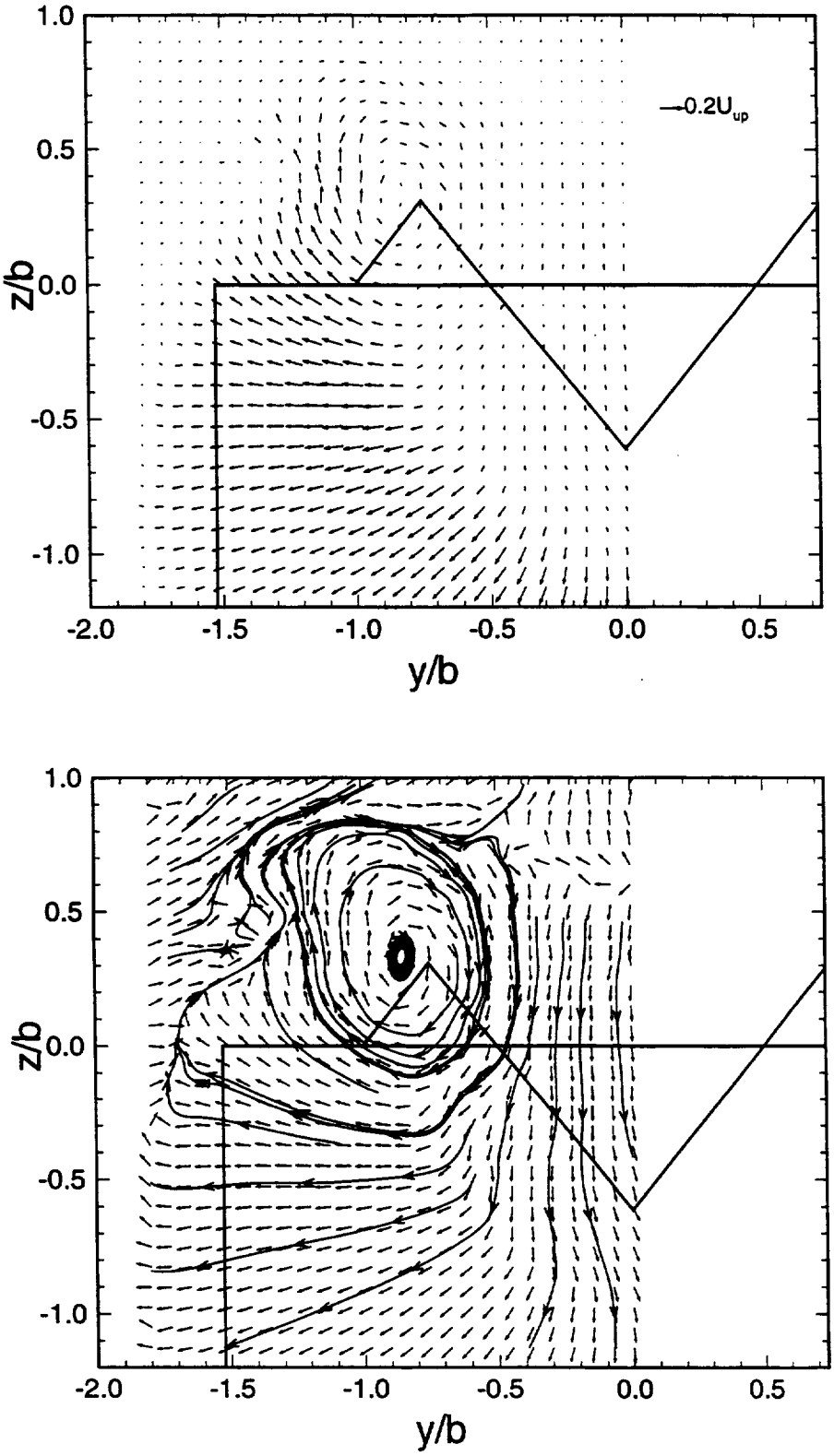

Figure 5.43: vw vector plot for the modified tab geometry at x/b=2.0: a) scaled, b) unscaled, c) $\overline{v} = 0$, $\overline{w} = 0$ intercepts d) singular points.

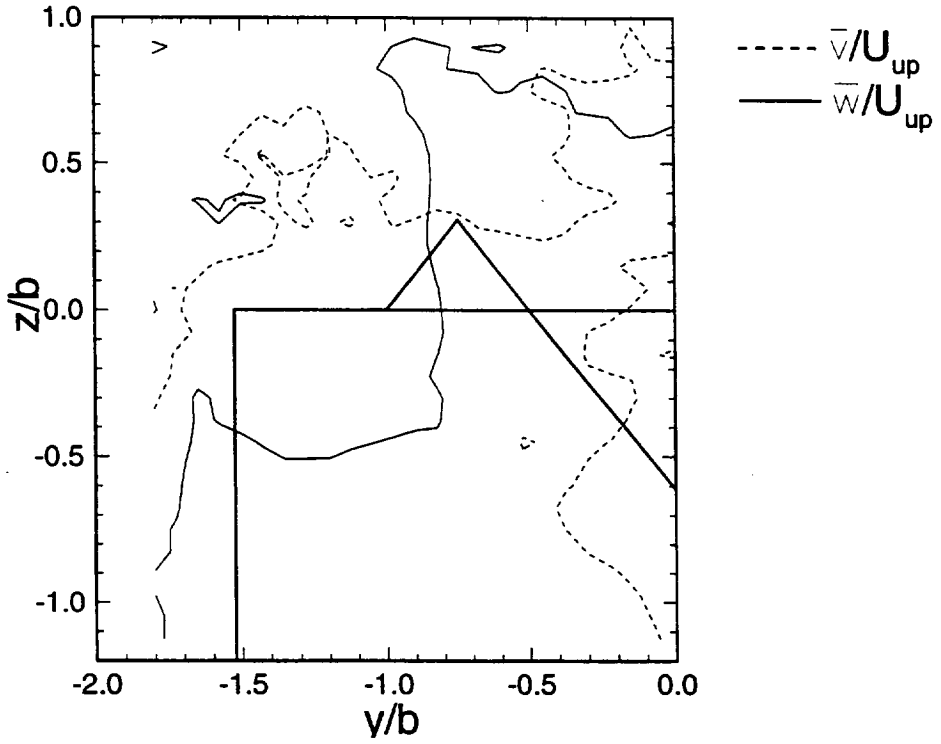

(c)

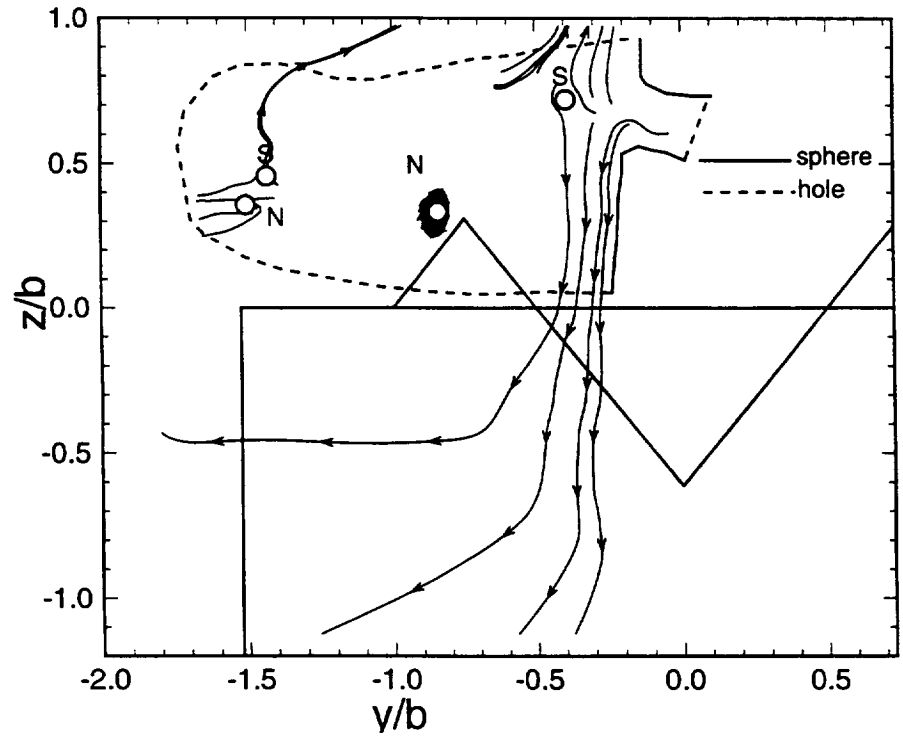

(d)

Figure 5.43: (continued)

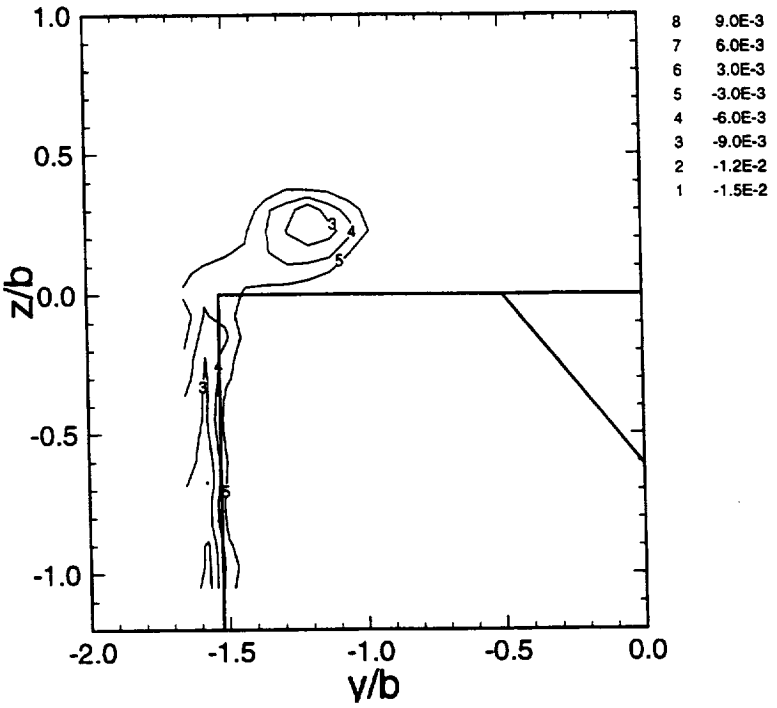

Figure 5.44: $\overline{u'v'}/\ U_{up}{}^2$ for the primary tab geometry at x/b=1.2.

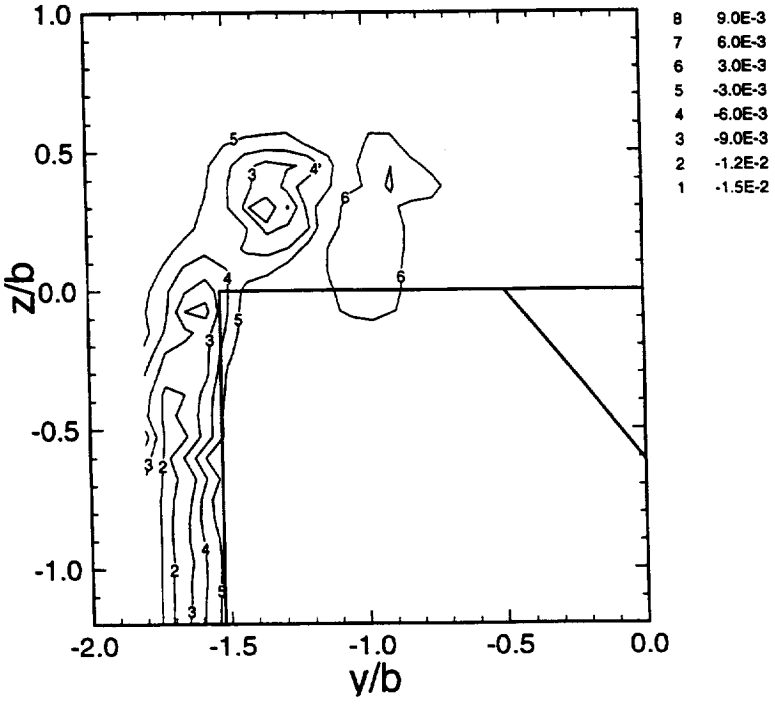

Figure 5.45: $\overline{u'v'}/\ U_{up}{}^2$ for the primary tab geometry at x/b=2.0.

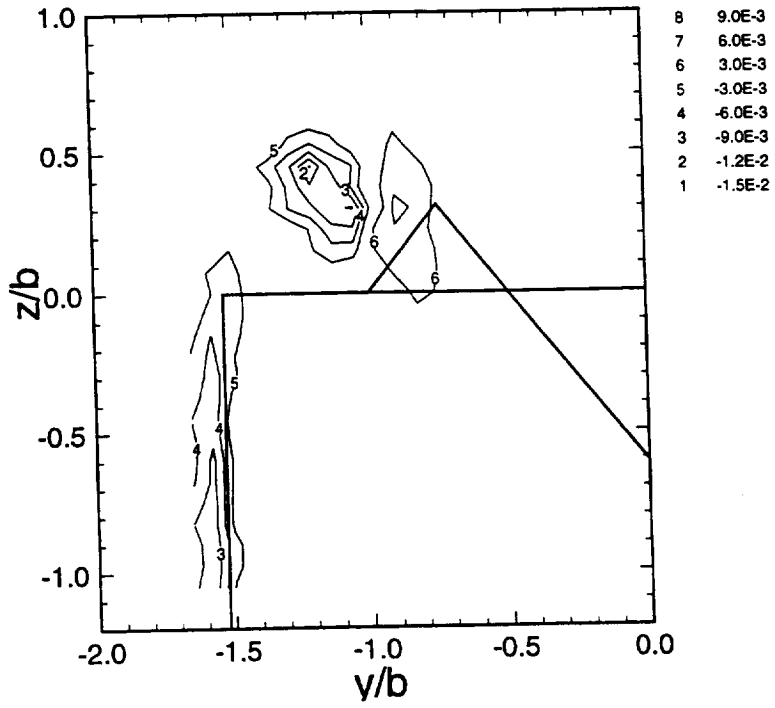

Figure 5.46: $\overline{u'v'}/U_{up}^2$ for the modified tab geometry at x/b=1.2.

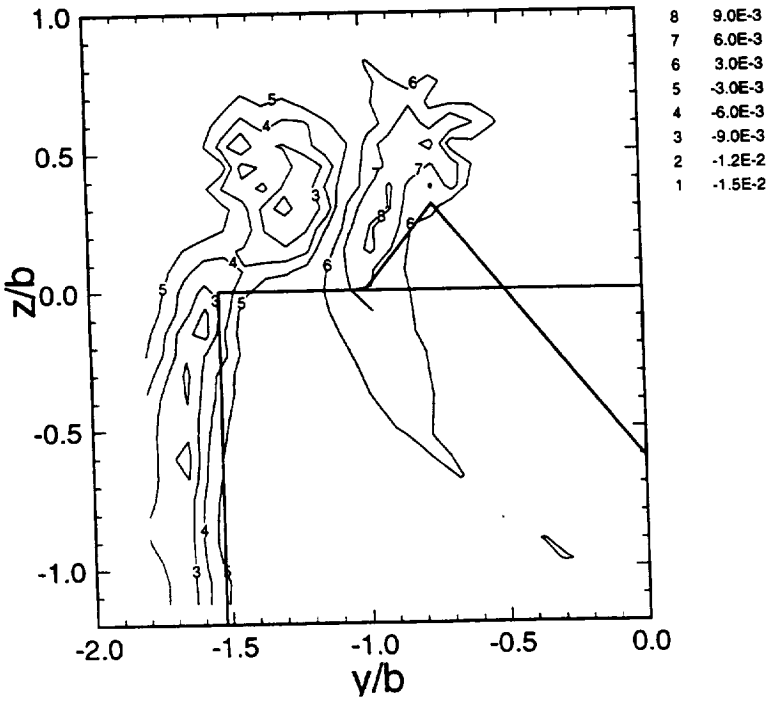

Figure 5.47: $\overline{u'v'}/U_{up}^2$ for the modified tab geometry at x/b=2.0.

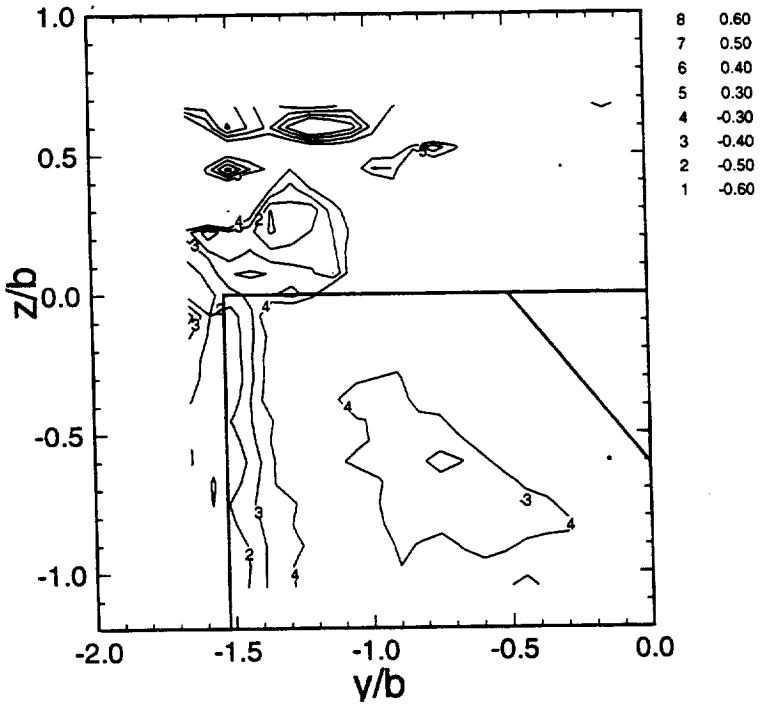

Figure 5.48: $\overline{u'v'}/\tilde{u}\tilde{v}$ for the primary tab geometry at x/b=1.2.

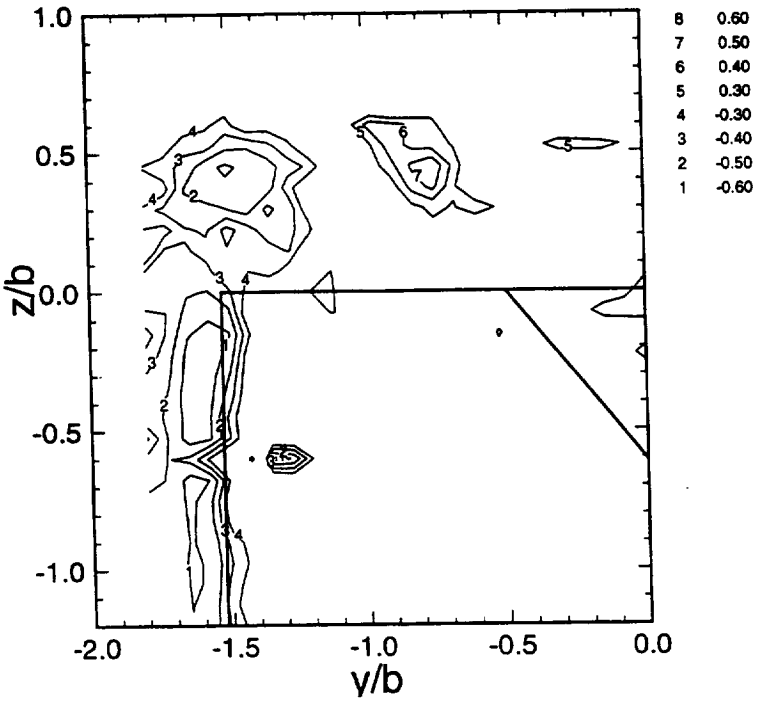

Figure 5.49: $\overline{u'v'}/\tilde{u}\tilde{v}$ for the primary tab geometry at x/b=2.0.

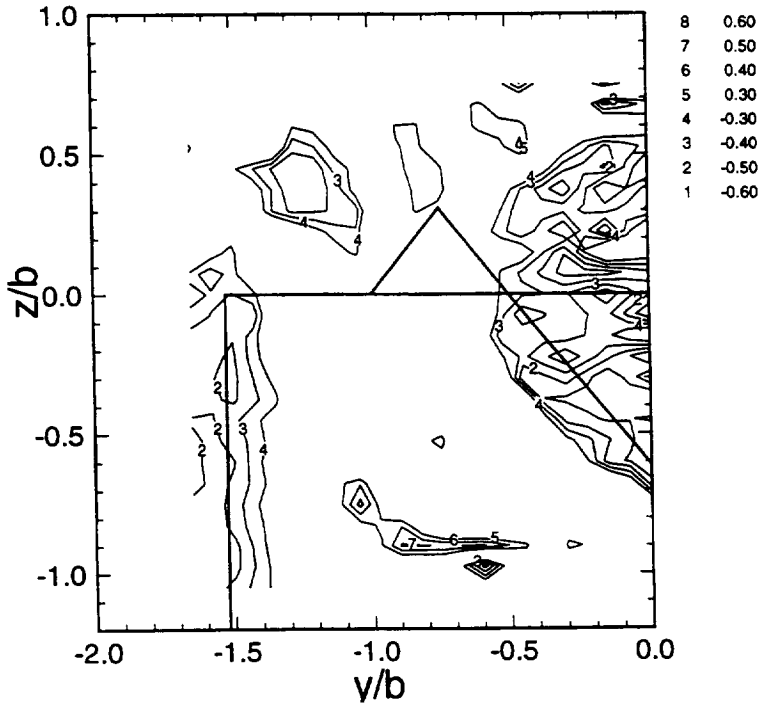

Figure 5.50: $\overline{u'v'}/\tilde{u}\tilde{v}$ for the modified tab geometry at x/b=1.2.

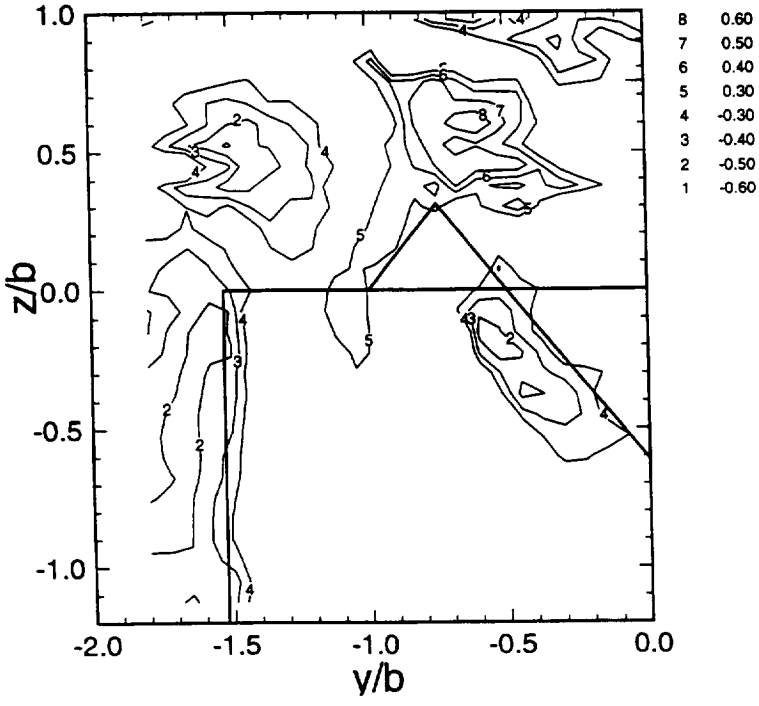

Figure 5.51: $\overline{u'v'}/\tilde{u}\tilde{v}$ for the modified tab geometry at x/b=2.0.

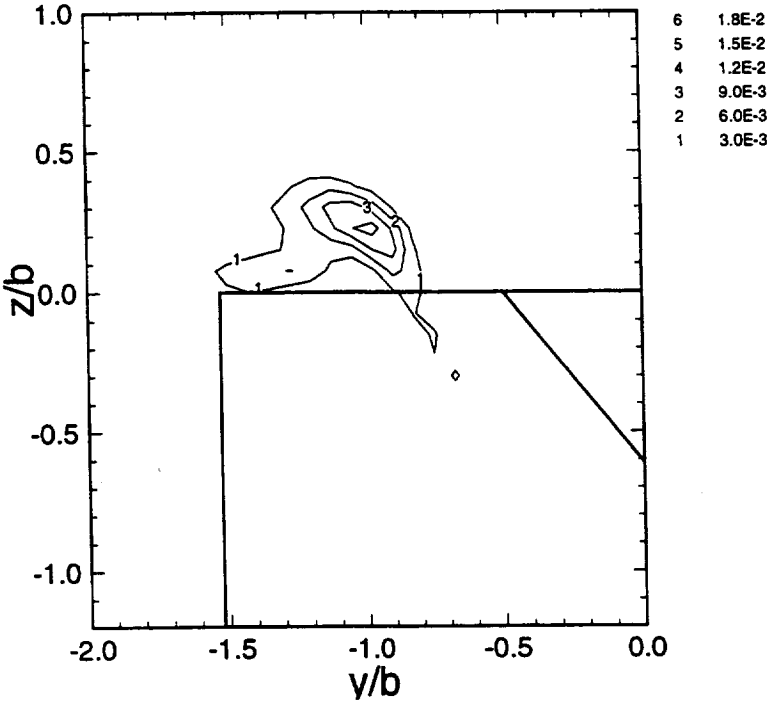

Figure 5.52: $\overline{u'w'}/\ U_{up}{}^2$ for the primary tab geometry at x/b=1.2.

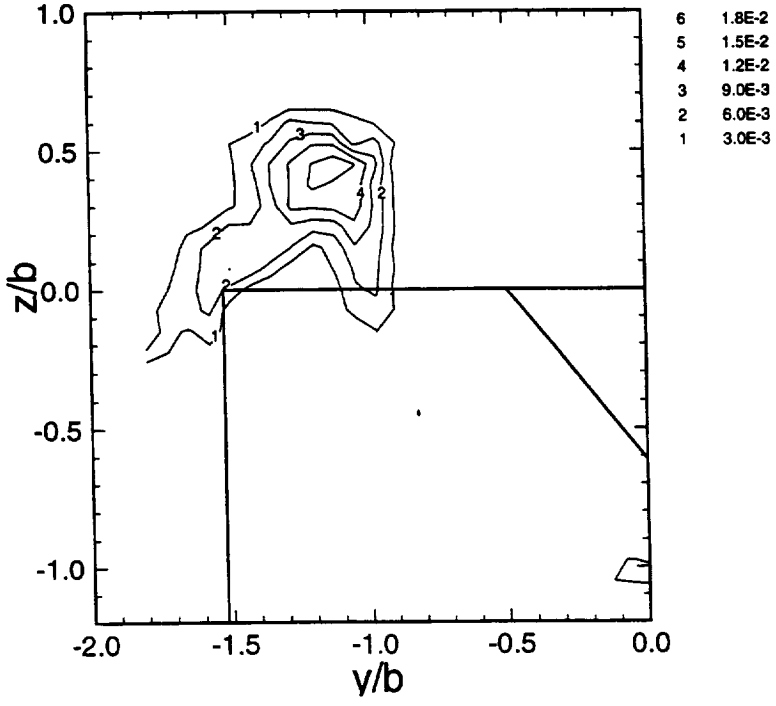

Figure 5.53: $\overline{u'w'}/\ u_{up}{}^2$ for the primary tab geometry at x/b=2.0.

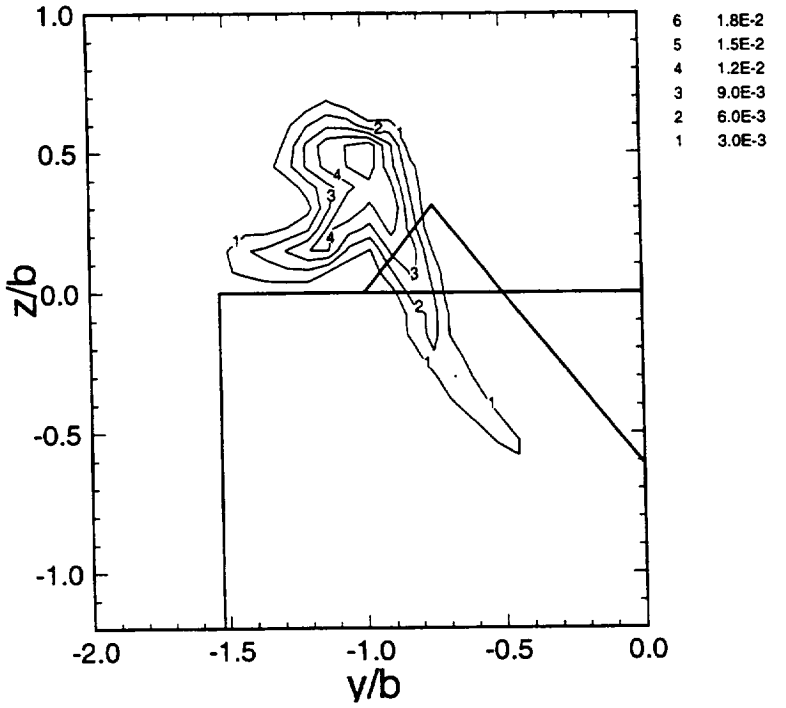

Figure 5.54: $\overline{u'w'}/U_{up}^2$ for the modified tab geometry at x/b=1.2.

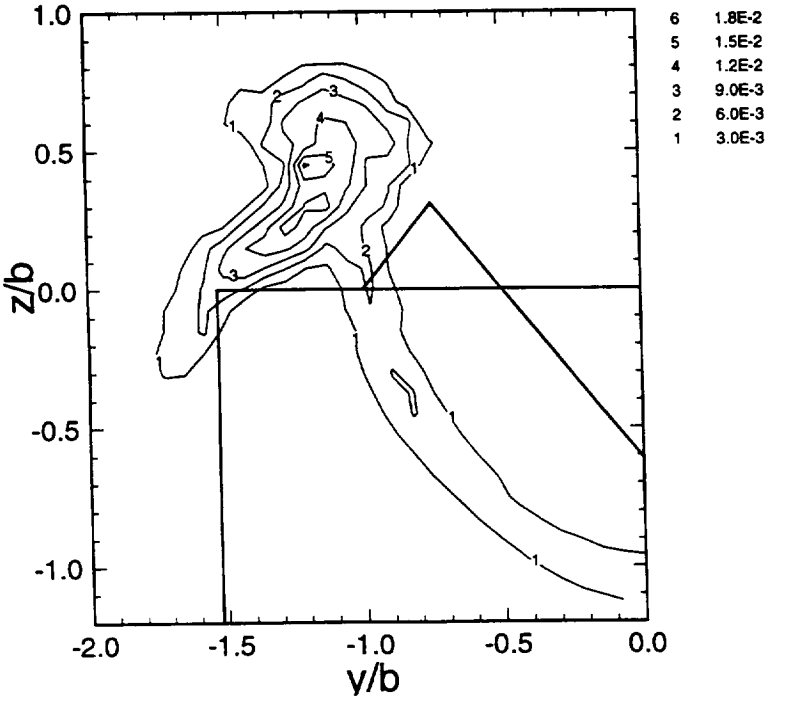

Figure 5.55: $\overline{u'w'}/u_{up}^2$ for the modified tab geometry at x/b=2.0.

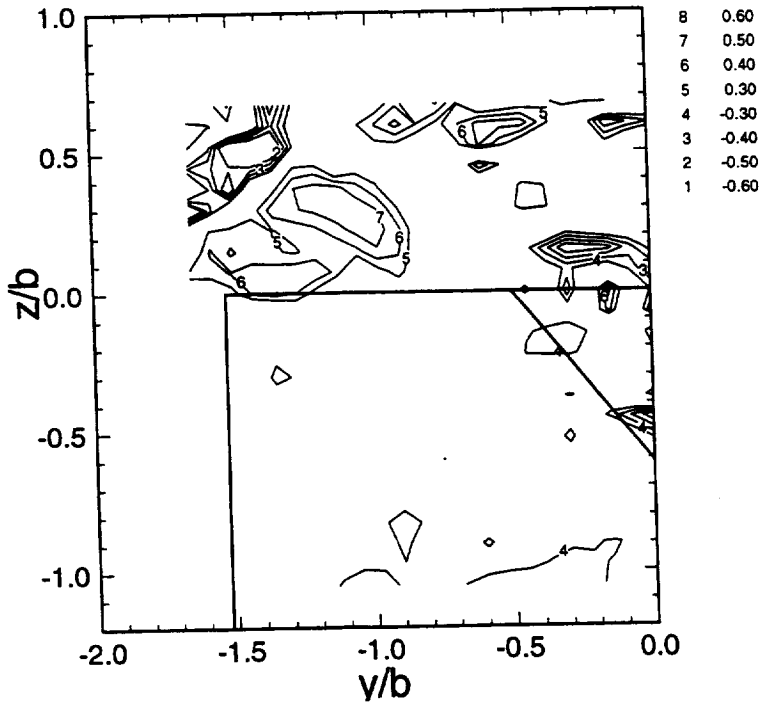

Figure 5.56: $\overline{u'w'}/\tilde{u}\tilde{w}$ for the primary tab geometry at x/b=1.2.

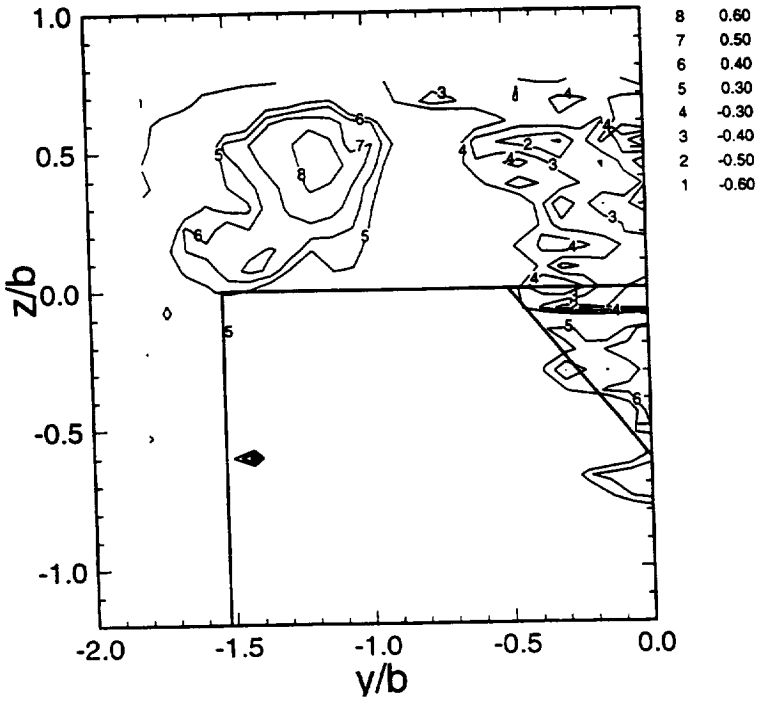

Figure 5.57: $\overline{u'w'}/\tilde{u}\tilde{w}$ for the primary tab geometry at x/b=2.0.

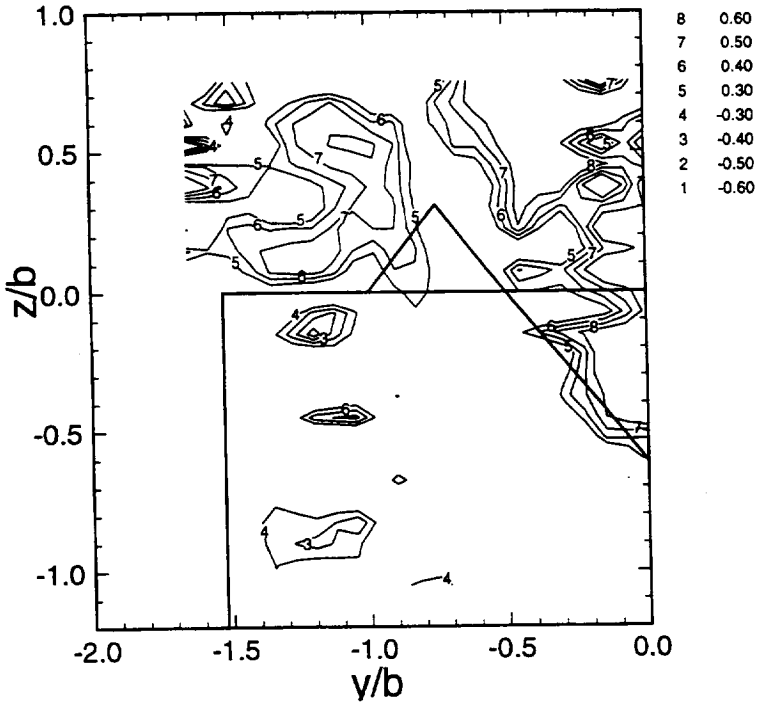

Figure 5.58: $\overline{u'w'}/\tilde{u}\tilde{w}$ for the modified tab geometry at x/b=1.2.

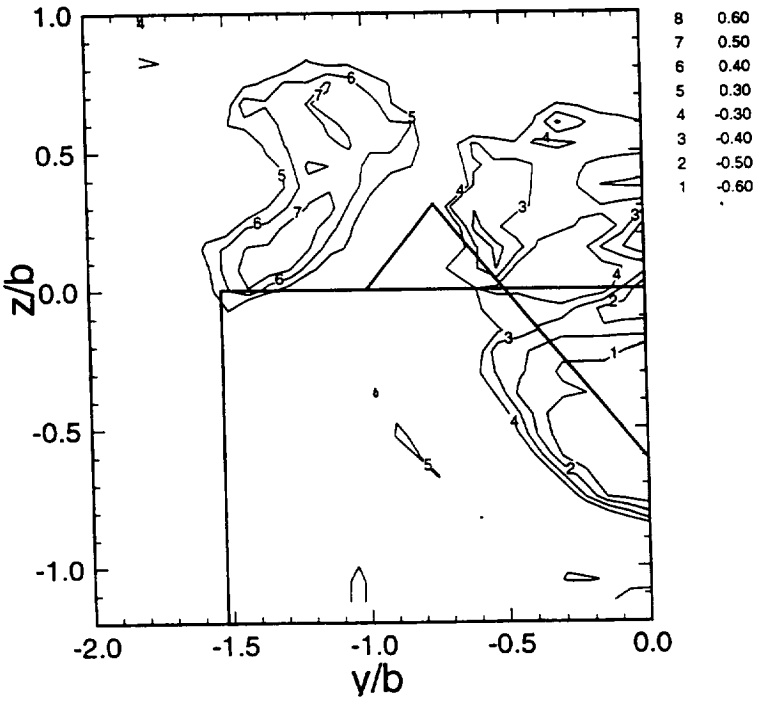

Figure 5.59: $\overline{u'w'}/\tilde{u}\tilde{w}$ for the modified tab geometry at x/b=2.0.

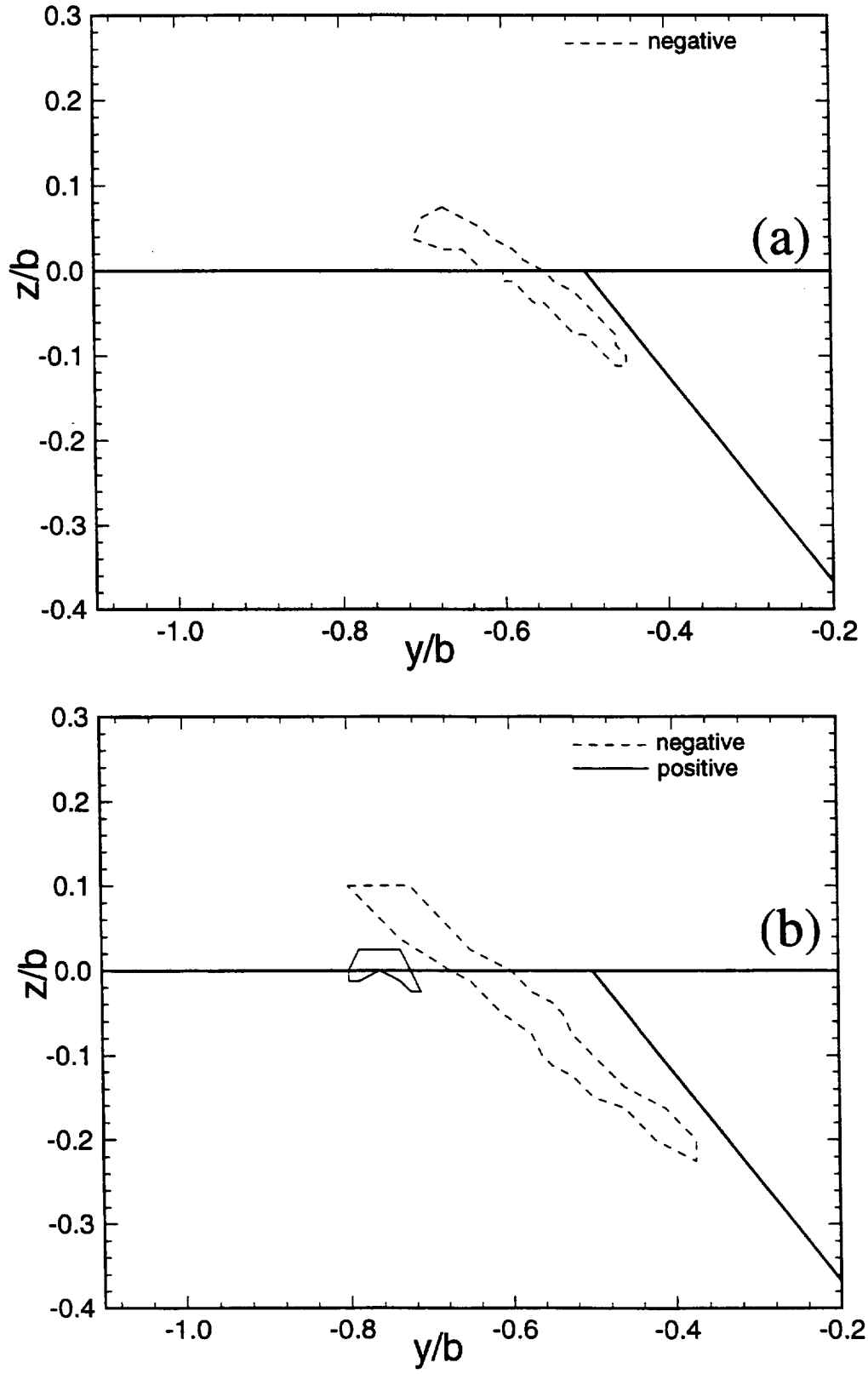

Figure 5.60: Cross-vane results for the primary tab geometry at x/b=: a)0.1, b)0.2, c)0.3, d)0.4.

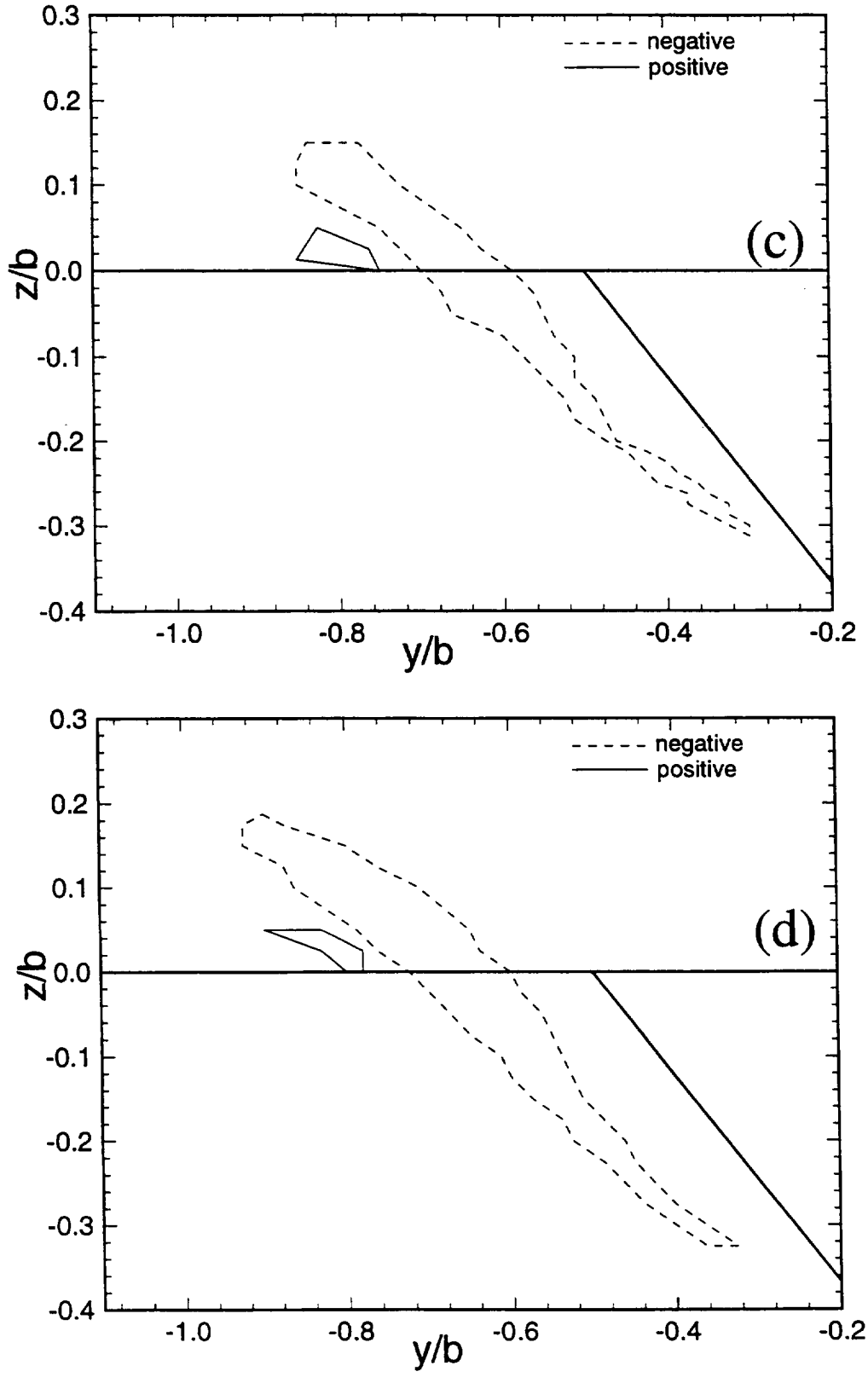

Figure 5.60: (continued)

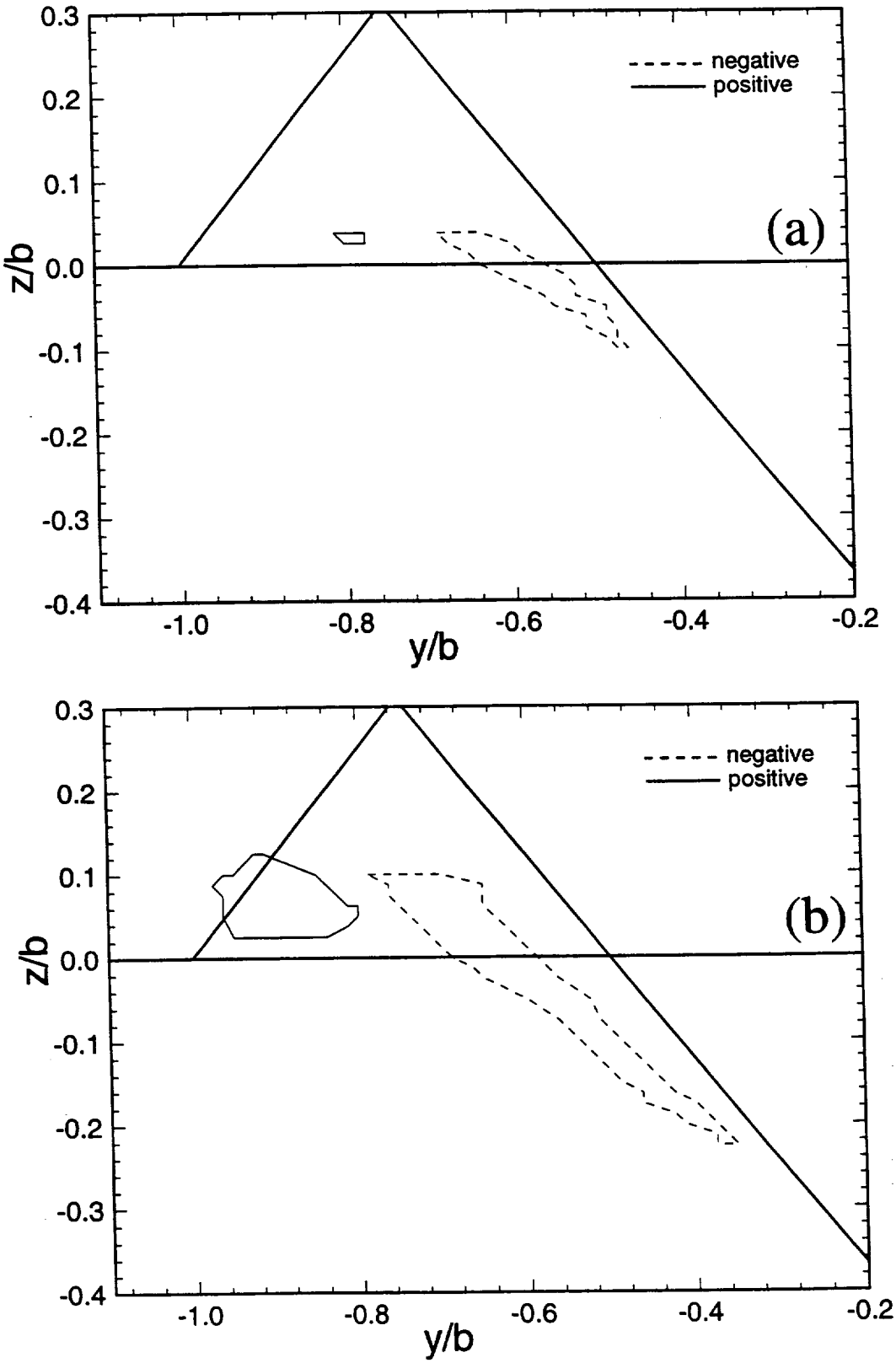

Figure 5.61: Cross-vane results for the modified tab geometry at x/b= a)0.1, b)0.2, c)0.3, d)0.4.

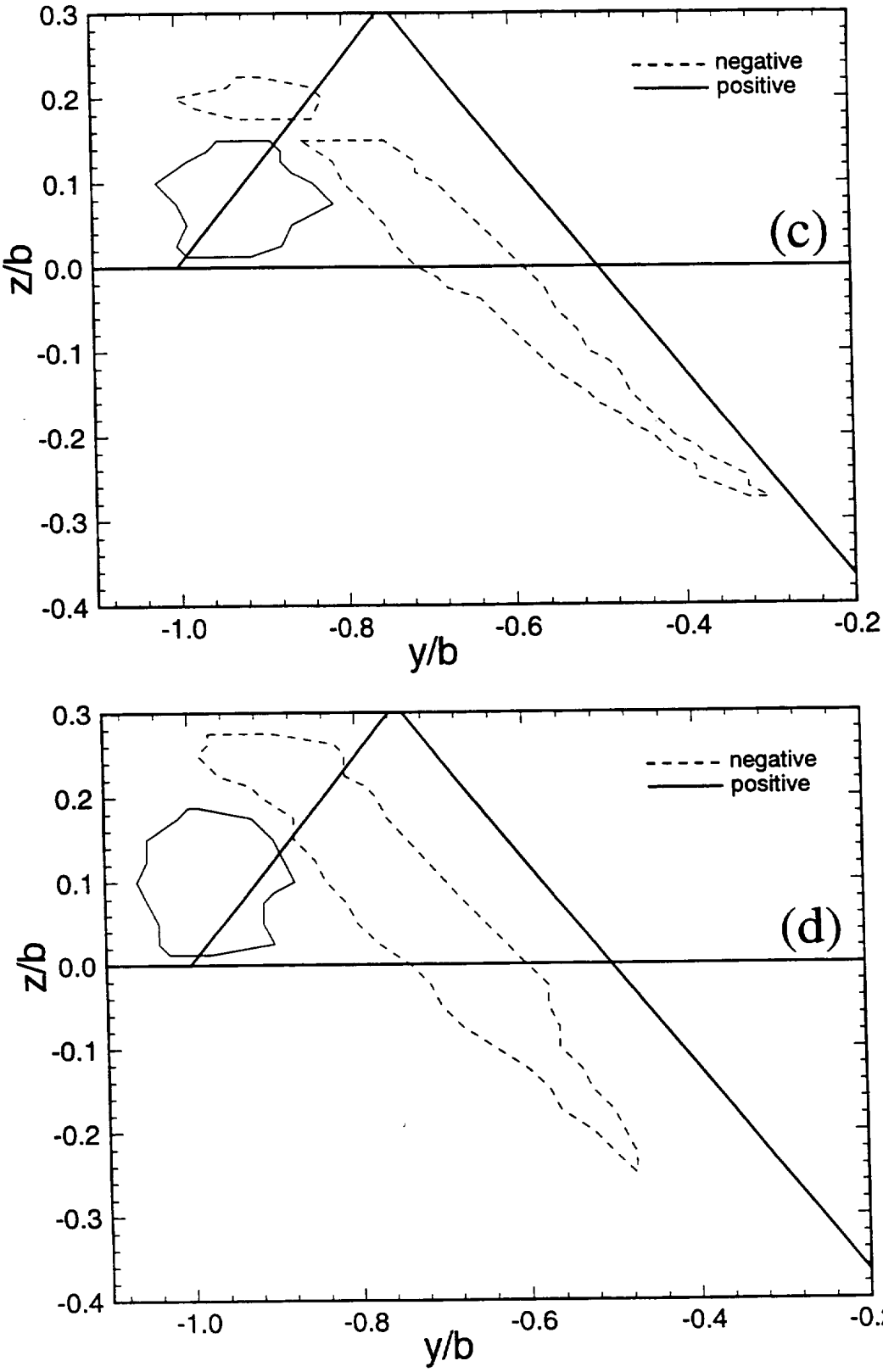

Figure 5.61: (continued)

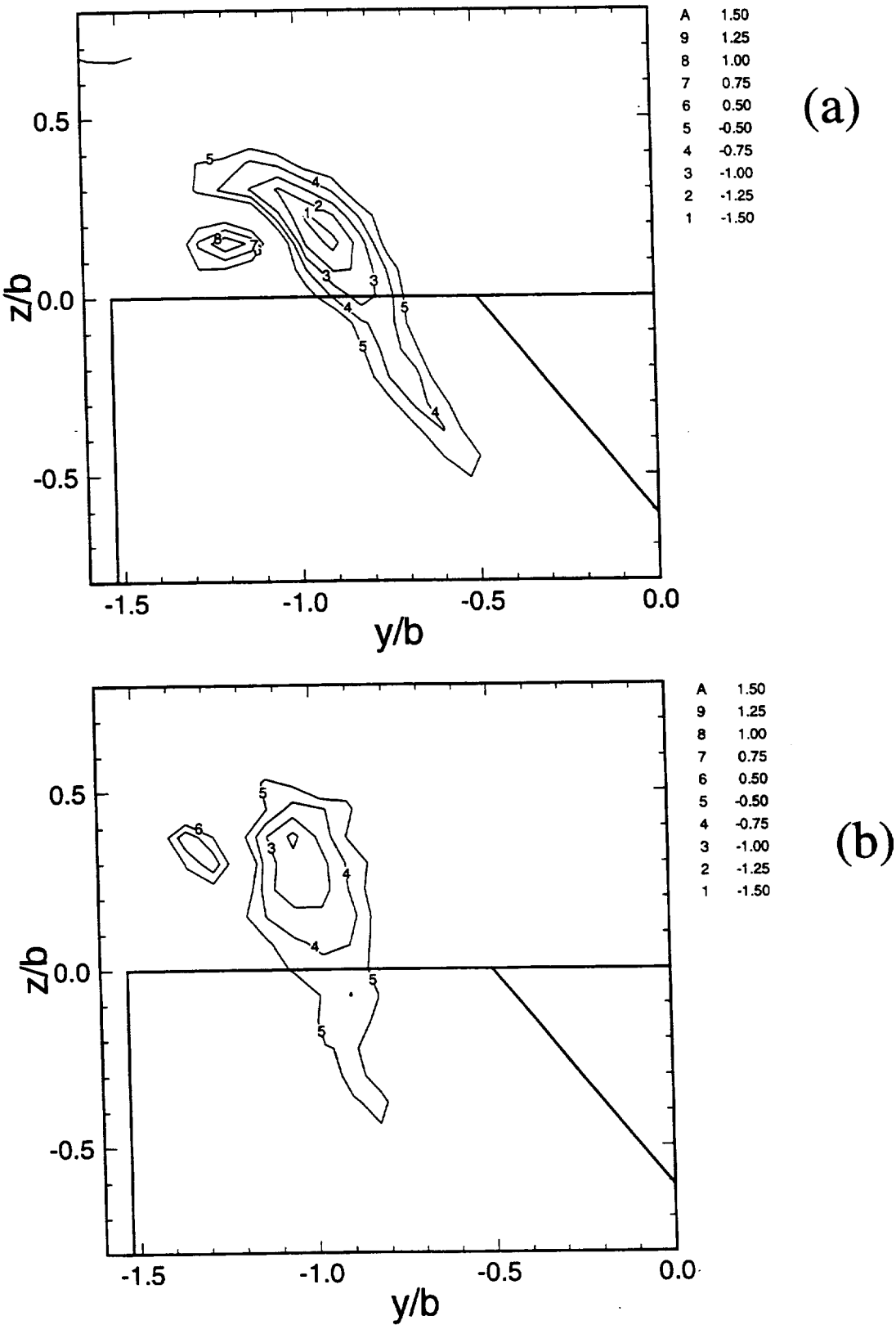

Figure 5.62: ω^*_x for the primary tab geometry: a) x/b=1.2, b) x/b=2.0.

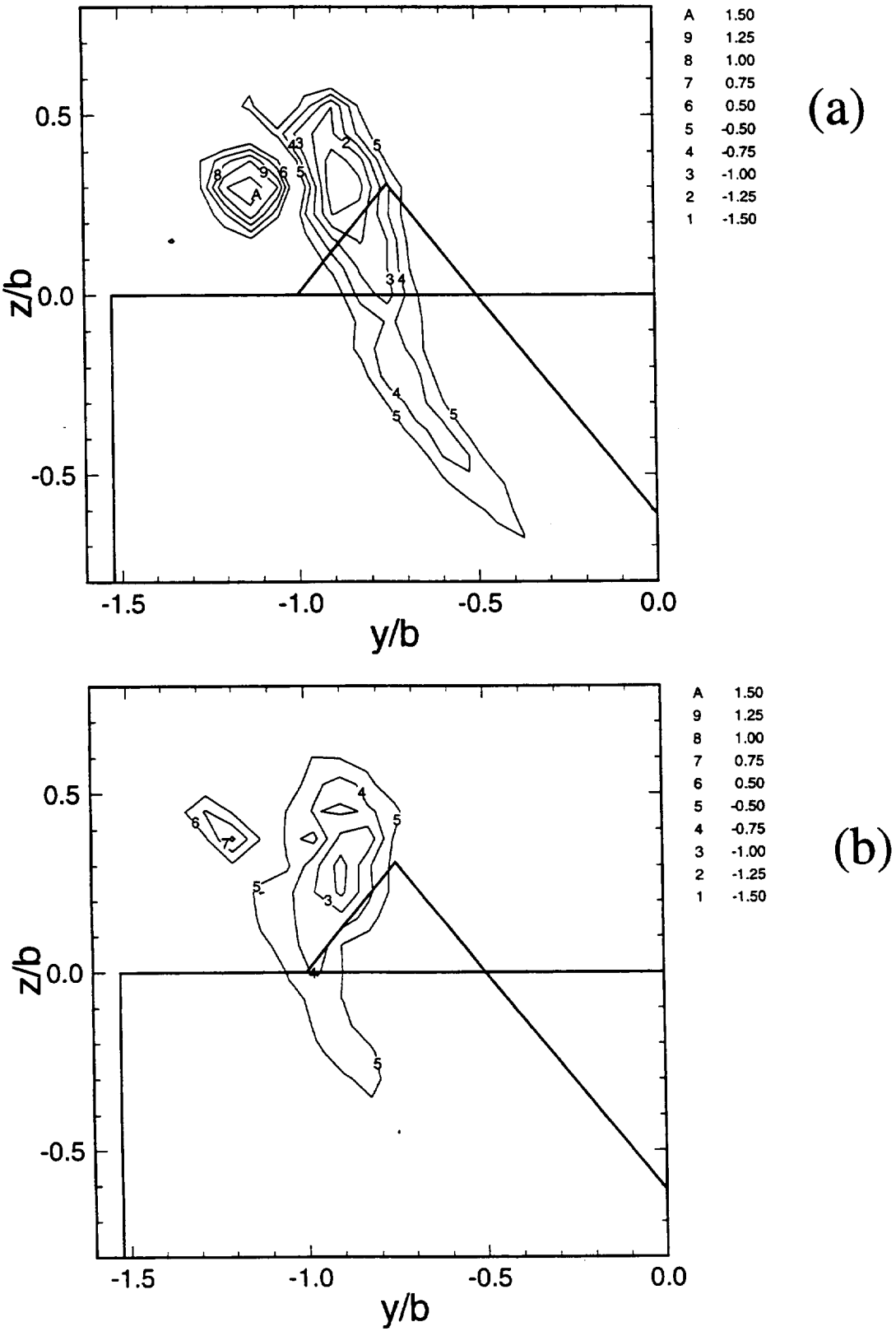

Figure 5.63: ω^*_x for the modified tab geometry: a) x/b=1.2, b) x/b=2.0.

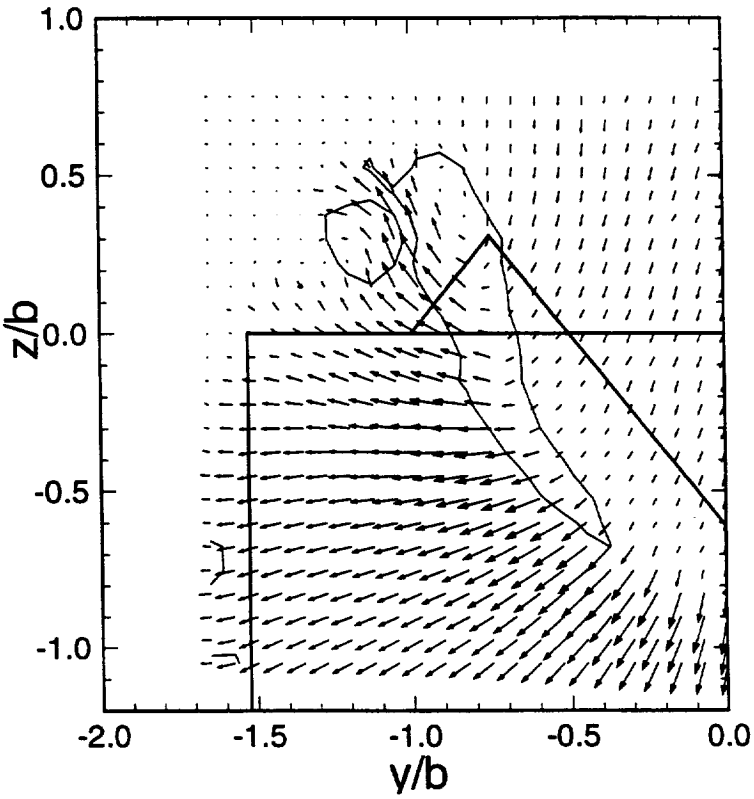

Figure 5.64: Overlay of vw vectors and $\overline{\omega_x}^*$ contours for the modified tab geometry at x/b=1.2.

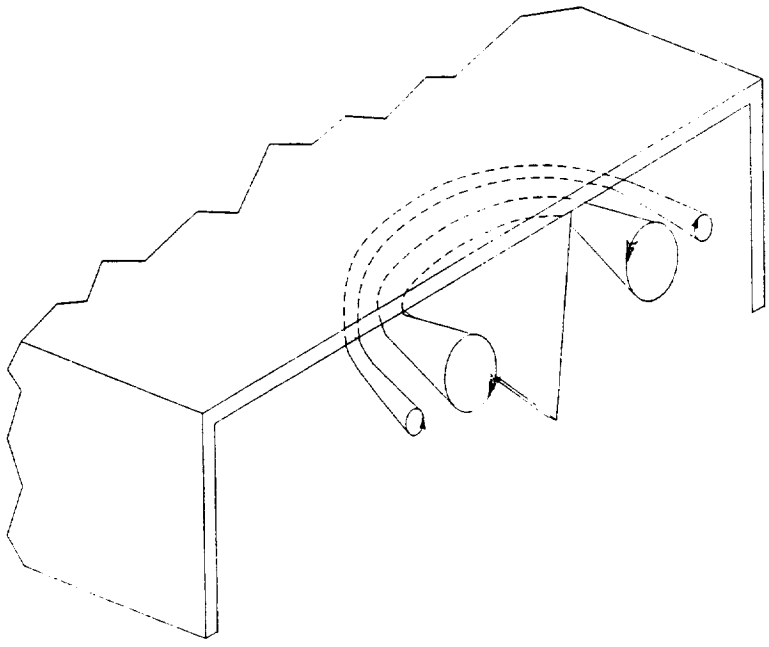

Figure 5.65: Inferred upstream vorticity connections.

6. SUMMARY AND CONCLUSIONS

6.1 Analysis of the Changes for the Flow Field of the Modified Tab Geometry

The expansion of a jet into the surrounding or ambient region can be greatly increased by using secondary tabs in addition to primary tabs which have previously been investigated. The addition of secondary tabs is herein designated as the modified tab geometry. The secondary tabs provide attachment surfaces for the naturally occurring expansion of the core flow into the ambient region. The resulting change in the trajectory of the jet flow causes a tighter curvature in the streamlines at the exit which changes the static pressure field near the exit.

The resulting changes in the static pressure field serves two purposes. First, the flux of ω_x into the flow upstream of the tab increases which enhanced the negative sense streamwise vorticity downstream of the exit. Second, the changes in the pressure field results in a favorable pressure gradient in some regions near the exit of the jet which significantly increases the positive ω_x downstream of the exit. The large scale distortion in the flow field is increased through the combined "pumping action" of the two regions of streamwise vorticity for the modified tab geometry.

In the case of the primary tab geometry the region of negative sense streamwise vorticity dominates the flow and creates the distortion demonstrated in the present study as well as in the past studies (Bradbury and Kahdeme (1975), Ahuja and Brown (1989), and Zaman et. al. (1994)) .

6.2 Conclusions

The following conclusions were supported through the use of several experimental techniques:

- Although the shear layer in the plume region of the primary tab geometry was severely distorted in shape compared to the untabbed geometry, it had similar characteristics. Specifically, the growth rate of the momentum thickness, $d\theta/dx$, was the same and the Reynolds shear stresses were similar for both geometries.
- The shear layer in the plume region for the modified tab geometry showed increased distortion in shape as well as a significant increase in both the growth rate of the momentum thickness and the Reynolds shear stresses compared to the primary tab geometry and the untabbed geometry.
- The flow field of the primary tab geometry and the modified tab geometry were nominally the same below the projected top wall of the tunnel. This indicated that the effect of the secondary tabs was primarily felt in the upper portion of the flow field.
- A favorable pressure gradient was created along side the primary tab and near the jet exit by the addition of the secondary tabs. This change in the pressure field increased the magnitude of the streamwise vorticity associated with the re-orientation of the boundary layer vorticity downstream of the exit for the modified tab geometry when compared to the primary tab geometry.
- The magnitude of the streamwise vorticity due to the upstream pressure hill was slightly increased downstream of the exit plane for the modified tab geometry when compared to the primary tab geometry for $y<0$.
- The two counter rotating regions of streamwise vorticity acted like a "pump" to eject fluid from the core region in the near field. The modified tab geometry showed a greater expansion of the core flow into the ambient region due to the increase in both regions of streamwise vorticity.

7. REFERENCES

Ahuja, K.K, and Brown, W.H., "Shear Flow Control by Mechanical Tabs", AIAA Paper 89-0994, 1989.

Anderson, Dale, Tannehill, John, and Pletcher, Richanrd, Computational Fluid Mechanics and Heat Transfer, Hemisphere Publishing Corp., New York, 1984.

Bradbury, L.J.S, and Khadem, A.H., "The Distortion of a Jet By Tabs", Journal of Fluid Mechanics, vol. 70, 1975.

Bradshaw, P., An Introduction to Turbulence and its Measurements, Pergamon, New York, 1975.

Bruns, J.M., Haw, R.C., Foss, J.F., "The Velocity and Transverse Vorticity Field in a Single Stream Shear Layer", Eight Symposium on Turbulent Shear Flows, Paper 3-1, 1991.

Collis, D.C., and Williams, M.J., "Two-Dimensional Convection from Heated Wires at Low Reynolds Number", Journal of Fluid Mechanics, 6:357-84, 1959.

Champagne

Foss, J.F., "The Effects of the Laminar/Turbulent Boundary Layer States on the Development of a Plane Mixing Layer", Symposium on Turbulent Shear Flows, Paper 11-D, 1977.

Foss, J.F., Wallace, J., Wark, C., "Vorticity Measurements", Instrumentation for Fluid Dynamics, Joseph Schetz and Allen Fuhs ed., Wiley and Sons, Inc., pp.1066-1067, 1995.

Foss, J.F., Klewicki, C.L., and Disimile, P.J., "Transverse Vorticity Measurements Using an Array of Four Hot-Wire Probes", NASA Contractor Report 178098, Appendix A, 1986.

Foss, J.K., and Zaman, K.B.M.Q., "Effect of a Delta Tab on Fine Scale Mixing in a Turbulent Two-Stream Shear Layer", AIAA Paper 96-0546, 1996.

Kock am Brink, B., and Foss, J.F., "Enhanced Mixing via Geometric Manipulation of a Splitter Plate", AIAA Paper 93-3244, 1993.

Kock am Brink, B., Streamwise Vorticity Measurements in the Wake of a Rippled and Planar Trailing Edge, MSU-ENG-91-009, 1991.

Liepmann, H., and Laufer, J., "Investigation of Free Turbulent Mixing", NACA Report No. 1257, 1947.

MKS Instruments, Inc., Bulletin 120/510-2/94, 1994.

Reeder, M. F., An Experimental Study of Mixing enhancement in Jets With Vortex Generating Tabs, PhD. Dissertation, Ohio State University, 1994.

Steffen, C.J., and Zaman, K.B.M.Q., "Analysis of Flow Field From a Rectangular Nozzle With Delta Tabs", AIAA Paper 95-2146, 1995.

Validyne Engineering Corporation, Bulletin DP15TL-2/78F, 1978.

Whitham, G.B., Laminar Boundary Layers, L. Rosehead ed., Clarendon Press, Oxford, pp. 114-133, 1963.

Wygnanski, I., and Fiedler, H.E., "The Two-Dimensional Mixing Region", Journal of Fluid Mechanics, Vol. 41, Part 2, pp.327-361, 1970.

Zaman, K.B.M.Q, Samimy, M., Reeder, M.F., "Control of an Axisymetric Jet Using Vortex Generators", Physics of Fluids A 6(2), pp.778-793, 1994.

Zaman, K.B.M.Q, Samimy, M., Reeder, M.F., "Effect of Tabs on the Evolution of an Axisymetric Jet", Eight Symposium on Turbulent Shear Flows, Paper 25-5, 1991.

Zaman, K.B.M.Q, Samimy, M., Reeder, M.F., "Streamwise Vorticity Generation and Mixing Enhancement in Free Jets by 'Delta-Tabs'", AIAA Paper 93-3253, 1993.

Zaman, K.B.M.Q, Samimy, M., Reeder, M.F., "Supersonic Jet Mixing Enhancement by 'Delta-Tabs'", AIAA Paper 92-3548.

APPENDIX A: Determination of β

The angle β was defined by a line drawn perpendicular to the sensor and the probe axis. This angle was nominally ±45 degrees for the sensors of as x-array, and zero for a single sensor probe. Note that while the angle β, was a physical property of the probe defined by the assembly of the sensors it was determined by the calibration data. The following analysis therefore determined the effective β, not the physical β for use in the processing algorithm. Equation (3.3) was rewritten with the dependence on γ removed from the A,B and n values by

$$E^2(Q,\gamma)=A+BQ^n\cos(\beta-\gamma)^n. \tag{A1}$$

Equation (A1) was then differentiated with respect to γ to produce

$$\frac{dE^2}{d\gamma} = 0+BQ^n\, n\cos(\beta-\gamma)^{n-1}\sin(\beta-\gamma). \tag{A2}$$

Solving equation (A2) for the quantity BQ^n yielded

$$BQ^n=(E^2-A)/\cos(\beta-\gamma)^n. \tag{A3}$$

Equation (A3) was substituted into equation (A2) and solved to give

$$\frac{dE^2}{d\gamma} = \frac{(E^2-A)\,n}{\cos(\beta-\gamma)^n}\cos(\beta-\gamma)^{n-1}\sin(\beta-\gamma) \tag{A4}$$

which simplified to

$$\tan(\beta) = \frac{dE^2}{d\gamma}(\gamma=0)/(E^2(\gamma=0)-A(\gamma=0))n. \tag{A5}$$

The calibration data were used to form a second order fit of E^2 versus γ, see Figure A.1.

The curve was differentiated once and evaluated at $\gamma=0$. The angle β was then determined using equation (A4).

REPORT DOCUMENTATION PAGE

Form Approved
OMB No. 0704-0188

1. AGENCY USE ONLY (*Leave blank*)	2. REPORT DATE	3. REPORT TYPE AND DATES COVERED
	November 1997	Final Contractor Report

4. TITLE AND SUBTITLE

An Experimental Study of the Near Field Region of a Free Jet With Passive Mixing Tabs

5. FUNDING NUMBERS

WU–537–05–21–00
NAG3–1459

6. AUTHOR(S)

D.G. Bohl and J.F. Foss

7. PERFORMING ORGANIZATION NAME(S) AND ADDRESS(ES)

Michigan State University
College of Engineering
East Lansing, Michigan 48824

8. PERFORMING ORGANIZATION REPORT NUMBER

E–10993

9. SPONSORING/MONITORING AGENCY NAME(S) AND ADDRESS(ES)

National Aeronautics and Space Administration
Lewis Research Center
Cleveland, Ohio 44135–3191

10. SPONSORING/MONITORING AGENCY REPORT NUMBER

NASA CR—97-206296
MSU-ENGR-04-96
TSFL-R-044

11. SUPPLEMENTARY NOTES

Project Manager, Khairul Q. Zaman, Turbomachinery and Propulsion Systems Division, NASA Lewis Research Center, organization code 5860, (216) 433–5888.

12a. DISTRIBUTION/AVAILABILITY STATEMENT

Unclassified - Unlimited
Subject Category: 37 Distribution: Nonstandard

This publication is available from the NASA Center for AeroSpace Information, (301) 621–0390.

12b. DISTRIBUTION CODE

13. ABSTRACT ***(Maximum 200 words)***

An experimental study was performed to determine the flow characteristics of a tabbed free jet. Results were acquired in the near field (nominally 2 tab widths upstream to 2 tab widths downstream of the exit plane) of a tabbed jet. Upstream pressure results showed static pressure distributions in both the x- and y-directions along the top surface of the tunnel. Hot-wire measurements showed rapid expansion of the core fluid into the ambient region. Two counter rotating regions of streamwise vorticity were shown on each side of the primary tab. An enhancement of the tabbed jet concept was proposed and tested. Specifically, two tabs, half the scale of the primary tab, were added to the primary tab to provide attachment surfaces for the normally occurring ejection of fluid. The secondary tabs caused a slight increase in the streamwise vorticity created from the upstream static pressure gradient while significantly increasing the re-oriented boundary layer vorticity. The combined pumping effect of the two counter rotating regions of vorticity caused a significant increase in the transport of the jet core fluid into the surrounding region.

14. SUBJECT TERMS

Vorticity; Mixing layers; Jets; Tabs

15. NUMBER OF PAGES

165

16. PRICE CODE

A08

17. SECURITY CLASSIFICATION OF REPORT	18. SECURITY CLASSIFICATION OF THIS PAGE	19. SECURITY CLASSIFICATION OF ABSTRACT	20. LIMITATION OF ABSTRACT
Unclassified	Unclassified	Unclassified	